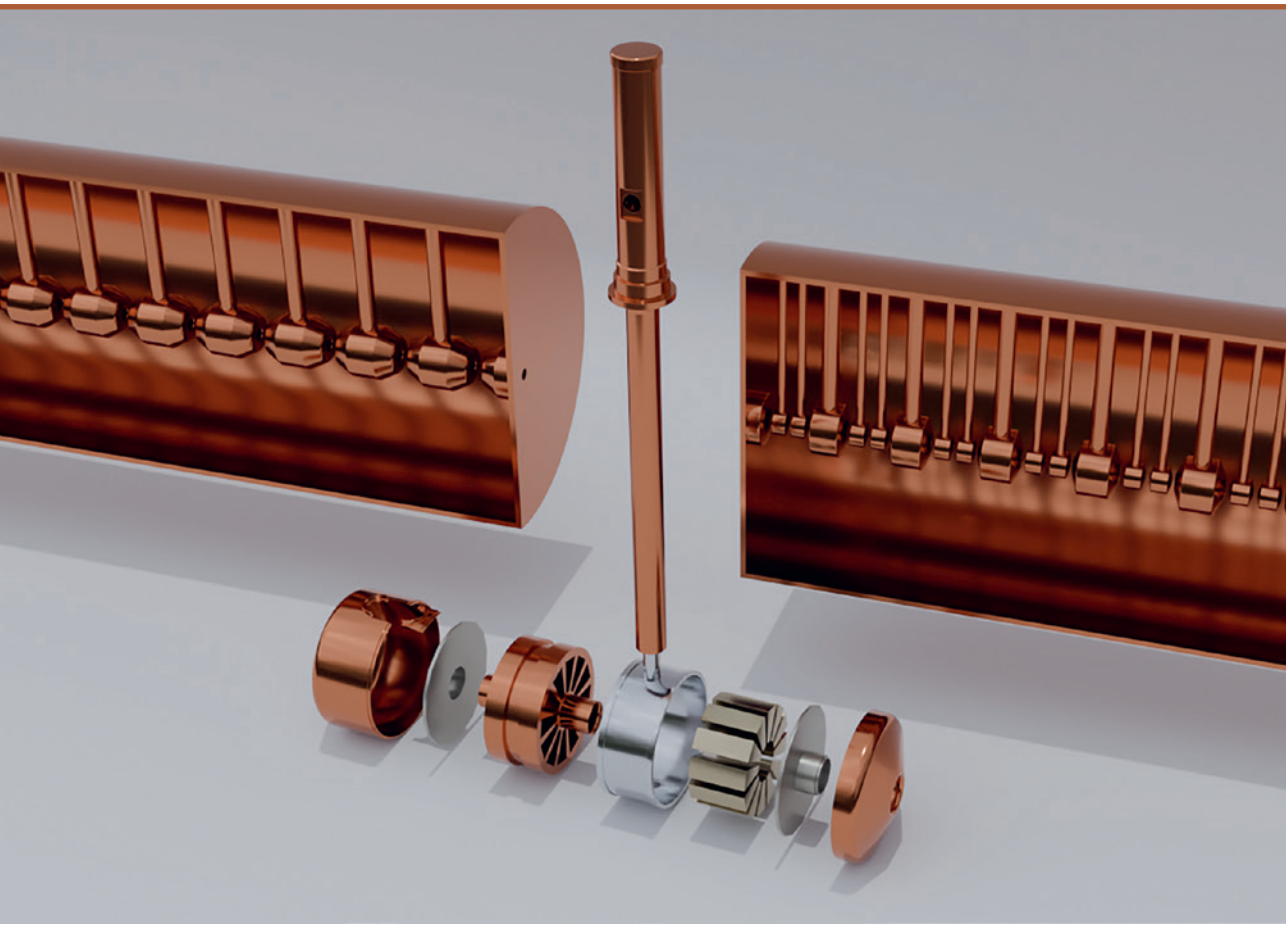
RIGA TECHNICAL UNIVERSITY

Lazar Nikitović

DEVELOPMENT OF LINEAR ACCELERATING STRUCTURES FOR ION INJECTION INTO A CANCER THERAPY SYNCHROTRON AND PARALLEL PRODUCTION OF RADIOISOTOPES

Doctoral Thesis



RTU Press
Riga 2026

RIGA TECHNICAL UNIVERSITY
Faculty of Natural Sciences and Technology
Institute of Particle Physics and Accelerator Technologies

Lazar Nikitović
Doctoral Student of the Study Programme
"Particle Physics and Accelerator Technologies"

DEVELOPMENT OF LINEAR ACCELERATING STRUCTURES FOR ION INJECTION INTO A CANCER THERAPY SYNCHROTRON AND PARALLEL PRODUCTION OF RADIOISOTOPES

Doctoral Thesis

Scientific supervisors

Dr. sc. ing.
TOMS TORIMS

Dr. phys.

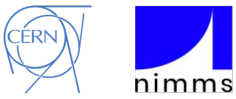
MAURIZIO VRETENAR

Riga 2026

Nikitović, L. Development of Linear Accelerating Structures for Ion Injection into a Cancer Therapy Synchrotron and Parallel Production of Radioisotopes. Summary of the Doctoral Thesis. Riga: RTU Press, 2026, 175 p.

Published in accordance with the decision of the Promotion Council "RTU P-03" of 26 August 2026, Minutes No. 04030-9.3.2/5.

Research has been performed in collaboration with the European Organisation for Nuclear Research (CERN) *Next Ion Medical Machine Study* (NIMMS) group.



The research was carried out within the framework and with financial support of the following projects:

- State Research Programme (SRP) "High-energy physics and accelerator technologies" VPP-IZM-CERN-2020/1-0002; VPP-IZM-CERN-2022/1-0001;



- Horizon 2020 project "Heavy Ion Therapy Research Integration *plus*" (HITRI*plus*) WP7.4. This project has received funding from the European Union's Horizon 2020 Research and Innovation programme under grant agreement No. 101008548.



Cover photo was created by Lazar Nikitović

DOCTORAL THESIS PROPOSED TO RIGA TECHNICAL UNIVERSITY FOR PROMOTION TO THE SCIENTIFIC DEGREE OF DOCTOR OF SCIENCE

To be granted the scientific degree of Doctor of Science (PhD) in Physics and Astronomy, the present Doctoral Thesis has been submitted for defence at the open meeting of the RTU Promotion Council on 30 November 2026 at 15:00, Zoom online: https://rtucloud1.zoom.us/j/918551261387.

OFFICIAL REVIEWERS

Dr. **Giovanni Bisoffi**
National Institute for Nuclear Physics (INFN), Italy

Dr. **Jean-Baptiste Lallement**
European Organization for Nuclear Research (CERN), Switzerland

Prof. Dr. **Hendrik Hähnel**
Goethe University Frankfurt (GU), Germany

DECLARATION OF ACADEMIC INTEGRITY

I hereby declare that the Doctoral Thesis submitted for review to Riga Technical University for promotion to the scientific degree of Doctor of Science (PhD) is my own. I confirm that this Doctoral Thesis has not been submitted to any other university for promotion to a scientific degree.

Lazar Nikitović _____

Date: _____

The Doctoral Thesis has been written in English. It consists of 6 chapters, including Introduction and Conclusions, 88 figures, 36 tables, and 2 appendices; the total number of pages is 165, without appendices. The Bibliography contains 118 references.

ACKNOWLEDGMENTS

I would like to express my appreciation to my academic supervisor, Dr. Toms Torims, for giving me the opportunity to pursue my PhD at Riga Technical University, marking the first milestone in this journey.

I must extend my deepest thanks to my CERN supervisor, Dr. Maurizio Vretenar, who accepted me as his student and selflessly shared his invaluable knowledge with me. Without your continuous support, guidance, motivation, and advice, none of this would have been possible. I am deeply grateful for the opportunity to learn from you and for everything you have taught me - from introducing me to the fascinating world of particle accelerators and guiding me through my research, to helping me grow not only as a researcher, but also as a person. Thank you!

I would also like to thank the director of my institute, Dr. Kārlis Dreimanis, and his deputy, Dr. Andris Ratkus, for warmly welcoming me to the institute and for their continued support throughout the final stages of my PhD journey, particularly during the thesis submission process.

I cannot finish this page without mentioning my dear colleagues from the NIMMS group. I am grateful for all the discussions we have shared, which have contributed to my professional development. A special thanks goes to Ms. Alessandra Lombardi, the current leader of the NIMMS group, and her team for introducing me to beam dynamics at the beginning of this journey.

Throughout this long journey, my biggest support has been my family: my brother Luka, my mother Dušanka, and my father Mirko, who have always believed in me more than I have believed in myself. *Hvala vam na svemu!*

I would also like to thank all my fellow colleagues from the Institute of Particle Physics and Accelerator Technologies who shared room 419 with me while I was struggling to finish this thesis. Among them, I would like to give a special mention to (now Dr.) Kristaps Paļskis - *Paldies par visu, mans draugs! Tev ir draugs uz mūžu, uz kuru vienmēr vari paļauties.*

Last but definitely not least, I would like to thank my dear Dragon Boat club, Divonne-les-Bains, with whom I shared many memorable moments during my stay at SGP. All of you helped me keep my head cool while writing this thesis. *Un merci tout particulier à ma « patronne », Christelle : merci infiniment pour tout !*

ABSTRACT

The demand for ion beams heavier than protons for cancer therapy, particularly carbon and helium ions, has been steadily increasing in recent years. While proton therapy has long been established as a powerful tool for cancer treatment, its physical limitations constrain its application for treating certain types of cancer and have led to growing interest in studying the different particles. Carbon ions, due to their higher linear energy transfer (LET) and superior biological effectiveness, have demonstrated significant advantages in treating radio-resistant tumors, delivering precise and localized damage to cancerous cells while minimizing harm to surrounding healthy tissues. Similarly, helium ions have gained attention as they offer an intermediate solution between protons and carbon ions, with improved dose distribution, making them a promising choice for next-generation particle therapy. As the need for these ions continues to rise, so does the requirement for advanced acceleration technologies capable of delivering high-quality ion beams efficiently and reliably at an affordable cost.

Helium and carbon ions are initially accelerated with a linac, ensuring beam quality before being injected into the therapy synchrotron. To achieve the required beam quality and power efficiency for medical applications, not only improvements in existing technologies but also the development of novel accelerator structures are necessary for modern particle therapy centers. This thesis presents a comprehensive study focused on the design and optimization of a promising linac structure, the Quasi-Alvarez Drift Tube Linac (QA-DTL), capable of accelerating both carbon and helium ions while ensuring high efficiency, and improved beam dynamics.

In addition to operating as a synchrotron injector, such a linac can also be utilized for the production of radioisotopes, which are used for medical diagnostics and therapeutic applications. By achieving both functionalities in parallel, this linac structure maximizes its utility and cost-effectiveness, making it an attractive solution for emerging medical facilities.

Alongside the structural advancements, this research introduces a set of algorithms specifically developed to optimize linac structures using well-established software for the design of linear accelerators. A key focus is placed on maximizing the effective shunt impedance per unit length, a crucial parameter in achieving greater acceleration efficiency while minimizing power consumption. These algorithms refine linac parameters to ensure optimal energy transfer and beam stability. Furthermore, to facilitate the implementation of these algorithms and streamline the design process, two graphical user interfaces (GUIs) have been developed, ensuring highly efficient linac structure designs.

By addressing the need for more efficient and versatile linac structures, the proposed solutions pave the way for future advancements in both particle therapy and radioisotope production. The findings and methodologies presented herein hold the potential to significantly impact the development of next-generation accelerator systems, ensuring their effectiveness in meeting the growing demands of modern medical and scientific applications.

ANOTĀCIJA

Pēdējos gados ir pastāvīgi audzis pieprasījums pēc joniem, kas smagāki nekā protoni, lai pielietotu tos vēža terapijai - jo īpaši oglekļa un hēlija joniem. Lai gan protonu terapijas pietojums kā vēža ārstēšanas metodei ir ievērojami pieaudzis, protonu fizikālā mijiedarbība ierobežo to terapeitisko pielietojumu atsevišķu vēža veidu ārstēšanā, izraisot pieaugošu interesi par citu jonu izpēti klīniskam pielietojumam. Oglekļa joni, pateicoties to augstākai lineārajai enerģijas pārnesei (LET) un augstākai bioloģiskajai efektivitātei, ir ar pierādītām, būtiskām priekšrocībām radiorezistentu audzēju ārstēšanā, nodrošinot precīzu un lokalizētu vēža šūnu bojājumu, vienlaikus līdz minimumam samazinot kaitējumu apkārtējiem veselajiem audiem. Tāpat arī hēlija joni ir guvuši ievērību, jo tie ir kā kompromiss starp protoniem un oglekļa joniem ar uzlabotu dozas sadalījumu, padarot tos par daudzsološu izvēli nākamās paaudzes daļiņu terapijai. Tā kā vajadzība pēc šiem joniem turpina pieaugt, pieaug arī prasība pēc progresīvām daļiņu paātrinātāju tehnoloģijām, kas spēj efektīvi un uzticami nodrošināt augstas kvalitātes jonu kūļus par pieņemamu cenu.

Hēlija un oglekļa jonus sākotnēji paātrina ar lineāro paātrinātāju, nodrošinot staru kūļa kvalitāti, pirms tie tiek ievadīti terapijas sinhrotronā. Lai sasniegtu medicīnā izmantojamiem lietojumiem nepieciešamo staru kūļa kvalitāti un energoefektivitāti, mūsdienu daļiņu terapijas centros ir nepieciešami ne tikai esošo tehnoloģiju uzlabojumi, bet arī jaunu paātrinātāju struktūru izstrāde. Šajā promocijas darbā ir sniegts visaptverošs pētījums par potenciālām lineārā paātrinātāja struktūrām, kurā galvenā uzmanība pievērsta daudzsološas struktūras - kvazi-Alvaresa dreifējošo cauruļu lineārā paaātrinātāja (QA-DTL) - projektēšanai un optimizācijai, kas spēj paātrināt gan oglekļa, gan hēlija jonus, vienlaikus nodrošinot augstu efektivitāti un uzlabotus staru kūļa dinamikas raksturlielumus.

Šādu lineāro paātrinātāju var izmantot ne tikai kā daļiņu injektoru sinhrotronā, bet arī radioizotopu ražošanai, kurus izmanto medicīniskajā diagnostikā un terapijā. Vienlaikus īstenojot abas funkcijas, šī lineārā paātrinātāja struktūra palielina tās lietderību un rentabilitāti, padarot to par pievilcīgu risinājumu jaunām medicīnas iekārtām.

Papildus konstrukcijas uzlabojumiem, šajā pētījumā ir arī izstrādāts algoritmu kopums, kas īpaši pielāgots lineāro paātrinātāju konstrukciju optimizācijai, izmantojot labi zināmu programmatūru lineāro paātrinātāju projektēšanai. Galvenā uzmanība tiek pievērsta efektīvās šunta pretestības maksimizēšanai uz garuma vienību, kas ir būtisks parametrs, lai sasniegtu lielāku paātrināšanas efektivitāti, vienlaikus samazinot enerģijas patēriņu. Šie algoritmi sniedz lineāro paātrinātāju dizaina parametrus, lai nodrošinātu optimālu enerģijas pārnesi un staru kūļa stabilitāti. Turklāt, lai atvieglotu šo algoritmu ieviešanu un racionalizētu projektēšanas procesu, ir izstrādātas divas grafiskās lietotāja saskarnes (GUI), kas nodrošina ļoti efektīvu lineāro paātrinātāju projektēšanas procesu.

Atsaucoties uz vajadzību pēc efektīvākām un daudzpusīgākām lineārā paātrinātāja struktūrām, sniegtie risinājumi bruģē ceļu turpmākai attīstībai gan daļiņu terapijā, gan radioizotopu ražošanā. Promocijas darbā izklāstītie rezultāti un metodoloģija ir ar potenciālu ietekmēt nākamās

paaudzes paātrinātāju sistēmu izstrādi, nodrošinot to efektivitāti, lai apmierinātu pieaugošās prasības mūsdienu pielietojumiem medicīnā un zinātnē.

LIST OF ABBREVIATIONS

Abbreviation	Meaning
ACS	Annular-ring Coupled Structure
AERT	Auger Electron-based Radioisotope Therapy
APF-DTL	Alternating Phase Focusing Drift Tube Linac
ATS	Accelerator and Technology Sector
BEVA	Bevatech GmbH
BTL	Beam Transport Line
CCDTL	Cell-Coupled Drift Tube Linac
CCTWT	Coupled-Cavity Traveling Wave Tube
CERN	Conseil Européen pour la Recherche Nucléaire
CH-DTL	Cross-bar H-mode Drift Tube Linac
CNAO	Centro Nazionale di Adroterapia Oncologica
DC	Direct Current
DEB	Debunching cavity
DLTWS	Disk-Loaded Traveling Wave Structure
DT	Drift Tube
DTL	Alvarez Drift Tube Linac
EM	Electromagnetic
ERC	Energy Ramping Cavity
ESS	European Spallation Source
GUI	Graphical User Interface
HIT	Heidelberg Ion-beam Therapy center
HITRI*plus*	Heavy Ion Therapy Research Integration *plus*
IAEA	International Atomic Energy Agency
IH-DTL	Interdigital H-mode Drift Tube Linac
KONUS	Combined zero degree structure
LANL	Los Alamos National Lab
LEBT	Low Energy Beam Transport
LET	Linear Energy Transfer
MIT	Marburg Ion-beam Therapy center
NIMMS	Next Ion Medical Machine Study
ORNL	Oak Ridge National Laboratory
PET	Positron Emission Tomography
PIMS	PI-Mode Structure
PMQ	Permanent Magnet Quadrupole
QA-DTL	Quasi-Alvarez Drift Tube Linac
RAL	Rutherford Appleton Laboratory
RF	Radio Frequency

RFQ	Radio Frequency Quadrupole
RHIC	Relativistic Heavy Ion Collider
RMS	Root Mean Square
S-IH-DTL	Separated function (tanks) Interdigital H-mode Drift Tube Linac
SCDTL	Side-Coupled Drift Tube Linac
SDTL	Separated-type Drift Tube Linac
SEEIIST	South East European International Institute for Sustainable Technologies
SPECT	Single Photon Emission Computed Tomography
SRR	Split-Ring Resonator
SSA	Solid State Amplifier
SW	Standing Wave
TAT	Targeted Alpha Therapy
TE	Transverse Electric
TM	Transverse Magnetic
WP	Work Package

LIST OF SYMBOLS

Symbol	Meaning
$A_{xx'}$	– Area of the Twiss ellipse in horizontal phase space, mm.mrad
$\vec{B}$	– Magnetic induction vector, T
B_x	– Horizontal magnetic induction component, T
B_y	– Vertical magnetic induction component, T
B_z	– Axial magnetic induction component, T
C_{dt}	– Production cost of all drift tubes, €
C'_{dt}	– Production cost of one drift tubes, €
C_l	– Capital cost of accelerating structure, €/m
C_l^{DTL}	– Capital cost of DTL, €/m
C_l^{QA}	– Capital cost of QA-DTL, €/m
C_p	– Capital cost of radio-frequency system, €/W
C_{pmq}	– Production cost of all permanent magnet quadrupoles, €
C'_{pmq}	– Production cost of one permanent magnet quadrupoles, €
C_{tank}	– Production cost of cavity, €
C'_{tank}	– Production cost per meter of cavity, €/m
C_{tot}	– Total cost of linac structure, €
C_{tot}^{DTL}	– Total cost of DTL, €
C_{tot}^{QA}	– Total cost of QA-DTL, €
E_0	– Average axial electric field amplitude, V/m
E_1	– Amplitude of the electric field, V/m
E_θ	– Azimuthal electric field component, V/m
E_{cx}	– Horizontal component of electric field generated by the particle, V/m
E_{kp}	– Kilpatrick field, kp
E_r	– Radial electric field component, V/m
E_z	– Axial electric field component, V/m
F_{cx}	– Horizontal component of Coulomb's repulsive electric force, N
G	– Quadrupole gradient, T/m
H_1	– Amplitude of the magnetic field, A/m
H_θ	– Azimuthal magnetic field component, A/m
H_{en}	– Hamiltonian, the total energy of the particle's oscillations, J
H_r	– Radial magnetic field component, A/m
H_z	– Axial magnetic field component, A/m
I_b	– Beam current, A
J'_m	– Derivative of the Bessel function of the first kind
J_m	– Bessel function of the first kind
L_{PMQ}	– Available space for the PMQ within the designed drift tube, m
L_c	– Length of the cell, m

L_f – Flat edge length, m

L_g – Gap length, m

L_s – Stem diameter, m

$L_{ucut}^{(1)}$ – Length of shorter undercut in H-mode type linac structures, m

$L_{ucut}^{(2)}$ – Length of longer undercut in H-mode type linac structures, m

$\mathbf{M}$ – Transfer matrix

N or N_{cell} – Number of consecutive coupled cells within the linac structure

N_p – Number of particles inside the beam

P_b – Beam power, W

P_d – Power dissipation of a resonator, W

P_{ext} – External power losses which arise due to external connections to the resonator, or when beam loading is non-negligible

Q_l – Loaded quality factor of a resonator

Q_u – Unloaded quality factor of a resonator

R – Shunt impedance, Ω

$\mathbf{R}$ – Twiss matrix

R' – Shunt impedance per unit length, Ω/m

R_b – Bore radius, m

R_{cav} – Cavity radius, m

R_c – Corner radius, m

R_{dt} – Drift tube radius, m

R_i – Inner nose radius, m

R_o – Outer nose radius, m

T – Transit-time factor

U – Energy stored within a resonator, J

V_0 – Axial RF voltage, V

W_{IN} – Input energy of linac structure, MeV

$W_{IN}^{(i)}$ – Input energy of i-th cell within the linac structure, MeV

W_{OUT} – Output energy of linac structure, MeV

W_{cur} – Input energy of the designed cell, MeV

$\mathbf{X}$ – State vector

Z – Effective shunt impedance, Ω

$ZT2_{best}$ – Maximum effective shunt impedance per unit length for the cell currently being designed, Ω/m

$ZT2_{cal}$ – Calculated effective shunt impedance per unit length within the designed cells, Ω/m

Z' or ZT^2 – Effective shunt impedance per unit length, Ω/m

ΔW – Energy the particle gains within a cell, MeV

$\Delta W^{(i)}$ – Energy gain in i-th cell within the linac structure, MeV

ΔW_d – Energy the particle gains within a cell relative to the synchronous

particle, MeV

ΔW_s – Energy the synchronous particle gains within a cell, MeV

$\Delta\beta$ – Velocity difference between the oscillating and synchronous particles relative to the speed of light in free space

$\Delta\phi$ – Phase shift of the oscillating particle relative to the phase of the synchronous particle, °

$\Delta\phi_c$ – Phase shift between two neighboring cells, °

$\alpha(s)$ – Alpha function, one of the three Twiss parameters

β – Velocity of the particle relative to the speed of light in free space

$\beta(W_{cur})$ – Particle velocity corresponding to the W_{cur} energy

$\beta(s)$ – Beta function, one of the three Twiss parameters, mm/π.mrad

β_s – Velocity of the synchronous particle relative to the speed of light in free space

γ – Face angle, °

$\gamma(s)$ – Gamma function, one of the three Twiss parameters, π.mrad/mm

γ_p – Lorentz factor of particle

γ_s – Lorentz factor of synchronous particle

λ – Radio frequency wavelength, m

μ – Permeability of a medium, H/m

ω – Mode angular frequency, rad/s

ω_0 – Resonant angular frequency, rad/s

ϕ – Phase of the field relative to its crest, °

$\phi(s)$ – Phase advance

ϕ_s – Phase of the synchronous particle, °

θ – Azimuthal coordinate, °

θ_e – Angle of rotation of the Twiss ellipse, °

ε – Permittivity of a medium, F/m

ε_{rms} – Unnormalized root mean square emittance, π.mm.mrad

$\varepsilon_{\phi w}$ – Beam emittance in longitudinal phase space, π.deg.MeV

ε_{err} – Maximal accepted difference between the calculated and desired resonant frequency, Hz

$\varepsilon_{n,rms}$ – Normalized root mean square emittance, π.mm.mrad

$\varepsilon_{xx'}$ – Beam emittance in horizontal phase space, π.mm.mrad

$\varepsilon_{yy'}$ – Beam emittance in vertical phase space, π.mm.mrad

a – Radius of the cylindrical resonator, m

c – Speed of light in free space, m/s

f_c^{TE} – Cutoff frequency of TE mode, Hz

f_c^{TM} – Cutoff frequency of TM mode, Hz

f_{res} – Resonant frequency, Hz

k_{ch} – Auxiliary variable

k_c	– Coupling coefficient
k_n	– Mode number
l	– Length of the cylindrical resonator, m
l_d	– Space between two consecutive quadrupoles within linac structure, m
l_q	– Quadrupole length, m
m	– Number of full-period variations of the field components in the azimuthal direction
m_0	– Rest mass of the accelerated particle, kg
n	– Number of zero-crossings of the axial field components
n_p	– Periodicity factor within QA-DTL
p	– Number of half-period variations of the field components in the longitudinal direction
p'_{mn}	– Root of the derivative of the Bessel function of the first kind
p_{mn}	– Root of the Bessel function of the first kind
$\vec{p_r}$	– Relativistic momentum vector of a particle in motion, kg·m/s
q	– Electric charge of the particle, C
r	– Radial coordinate, m
s	– Beam abscissa within the linac structure, m
v	– Particle velocity, m/s
v_z	– Particle velocity in longitudinal direction, m/s
x	– Position of the particle in the horizontal plane, mm
x'	– Angular deviation of the particle in the horizontal plane, mrad
x'_{mn}	– Zeros of the derivative of the Bessel function of the first kind
x_{mn}	– Zeros of the Bessel function of the first kind
y	– Position of the particle in the vertical plane, mm
y'	– Angular deviation of the particle in the vertical plane, mrad
z	– Axial coordinate which indicates the direction of the wave propagation, m

Table of Contents

LIST OF TABLES **17**

LIST OF FIGURES **19**

1 Introduction **25**
- 1.1 Aim of the doctoral thesis . . . 26
- 1.2 Hypothesis of the research . . . 27
- 1.3 Scope of the doctoral thesis . . . 27
- 1.4 Tasks of the doctoral thesis . . . 27
- 1.5 Scientific novelty . . . 27
- 1.6 Practical significance and applications . . . 28
- 1.7 Research Methodology . . . 28

2 Linear Accelerating Structures for Medical Applications **31**
- 2.1 State-of-the-art . . . 31
- 2.2 Linac structures used in particle therapy nowadays . . . 33
- 2.3 HITRI*plus* project . . . 35
- 2.4 NIMMS collaboration . . . 36
- 2.5 Radioisotope production with linac . . . 37
- 2.6 Conclusions . . . 39

3 RF and Beam Dynamics Theory of Linac Structures **40**
- 3.1 Electromagnetic field theory for linac structures . . . 40
  - 3.1.1 Modes inside linac structures . . . 40
  - 3.1.2 Energy gain in linac structure . . . 43
  - 3.1.3 Linac structure's figures of merit . . . 45
  - 3.1.4 Acceleration inside standing wave multi-cell structures . . . 47
- 3.2 Beam dynamics for linac structures . . . 49
  - 3.2.1 Longitudinal beam dynamics within linac structures . . . 50
  - 3.2.2 Transverse beam dynamics within linac structures . . . 53
  - 3.2.3 Beam distributions . . . 58
- 3.3 Analyzed structures for acceleration and beam manipulation . . . 61

3.3.1 Alvarez drift tube linac . . . 61
3.3.2 Quasi-Alvarez drift tube linac . . . 63
3.3.3 H-mode linac structures . . . 65
3.3.4 Other RF structures for beam manipulation within linacs . . . 66
3.4 Cost efficiency of Alvarez-type linac structures . . . 69
3.5 Conclusions . . . 74

4 Mathematical Model for Optimizing Geometry Parameters of Linac Structures 75
4.1 Simulation software . . . 75
4.2 Graphical User Interface for optimization of Alvarez and Quasi-Alvarez DTL cells 78
4.3 RF design and beam dynamics procedures . . . 81
4.3.1 Optimization algorithms used in RF design of Alvarez-type structures . 82
4.3.2 Optimization algorithms used in RF design of H-mode type structures . 90
4.3.3 Beam dynamics analysis . . . 94
4.4 Conclusions . . . 95

5 Research Results 96
5.1 HITRI*plus* carbon linac designs . . . 96
5.1.1 Quasi-Alvarez Drift Tube Linac for carbon injection into synchrotron . 97
5.1.2 H-mode Drift Tube Linac for carbon injection into synchrotron . . . 103
5.1.3 Alvarez Drift Tube Linac for radioisotope production . . . 113
5.1.4 Debunching cavity before injection into carbon synchrotron . . . 119
5.1.5 Comparison and choice of the ideal linac configuration . . . 121
5.2 NIMMS helium linac designs . . . 124
5.2.1 Quasi-Alvarez Drift Tube Linac for helium injection into synchrotron and radioisotope production . . . 125
5.2.2 H-mode Drift Tube Linac for helium injection into synchrotron . . . 130
5.2.3 Alvarez Drift Tube Linac for radioisotope production . . . 135
5.2.4 Debunching cavity and energy ramping cavity before injection into helium synchrotron . . . 141
5.2.5 Comparison and choice of the ideal linac configuration . . . 143
5.3 Isotope production helium linac design . . . 145
5.4 Conclusions . . . 149

6 Conclusions 151
6.1 Thesis statements to be defended . . . 152
6.2 Future research challenges . . . 153

BIBLIOGRAPHY 154

LIST OF PUBLICATIONS 164

APPENDICES **166**

LIST OF TABLES

1.1 Performance comparison of different linac structures for acceleration of low-velocity particles 29

2.1 List of prospective radioisotopes for use in diagnostics and therapeutics, producible using a linac that accelerates helium ions and/or deuterons 38

3.1 List of data regarding conventional DTL and QA-DTL 73

5.1 RF and geometry parameters of the QA-DTL for carbon ion acceleration from 0.7 MeV/u to 5 MeV/u 98
5.2 PMQ parameters of the QA-DTL for carbon ion acceleration from 0.7 MeV/u to 5 MeV/u 99
5.3 Beam parameters of the QA-DTL for carbon ion acceleration from 0.7 MeV/u to 5 MeV/u 100
5.4 RF and geometry parameters of the S-IH-DTL for carbon ion acceleration from 0.7 MeV/u to 5 MeV/u 104
5.5 PMQ parameters of the S-IH-DTL with quadrupole doublets for carbon ion acceleration from 0.7 MeV/u to 5 MeV/u 106
5.6 PMQ parameters of the S-IH-DTL with quadrupole triplets for carbon ion acceleration from 0.7 MeV/u to 5 MeV/u 107
5.7 Beam parameters of the S-IH-DTL for carbon ion acceleration from 0.7 MeV/u to 5 MeV/u 108
5.8 RF and geometry parameters of the DTL1 and DTL2 for acceleration of 5 mA helium ions from 5 MeV/u to 10 MeV/u 114
5.9 PMQ parameters of the DTL1 for acceleration of 5 mA helium ions from 5 MeV/u to 7.1 MeV/u 115
5.10 PMQ parameters of the DTL2 for acceleration of 5 mA helium ions from 7.1 MeV/u to 10 MeV/u 115
5.11 Beam parameters of the DTL1 and DTL2 for acceleration of 5 mA helium ions from 5 MeV/u to 10 MeV/u 116
5.12 RF and geometry parameters of DEB used for reducing energy spread of carbon ions before injection into therapy synchrotron 120

5.13 Beam parameters of DEB used for reducing energy spread of carbon ions before injection into therapy synchrotron 120
5.14 Comparison between QA-DTL and S-IH-DTL for carbon ion acceleration . . . 121
5.15 Comparison between QA-DTL and IH-DTL for carbon ion acceleration 122
5.16 Comparison between Alvarez-type and H-mode type linac configurations for carbon ion acceleration 123
5.17 RF and geometry parameters of the QA-DTL for acceleration of 5mA and 30mA helium ions from 1 MeV/u to 5 MeV/u 126
5.18 PMQ parameters of the QA-DTL for helium ion acceleration from 1 MeV/u to 5 MeV/u 126
5.19 Beam parameters of the QA-DTL for helium ion acceleration from 1 MeV/u to 5 MeV/u 127
5.20 RF and geometry parameters of the IH-DTL for helium ion acceleration from 1 MeV/u to 5 MeV/u 131
5.21 PMQ parameters of the IH-DTL for helium ion acceleration from 1 MeV/u to 5 MeV/u 132
5.22 Beam parameters of the IH-DTL for helium ion acceleration from 1 MeV/u to 5 MeV/u 133
5.23 RF and geometry parameters of the DTL1 and DTL2 for acceleration of 30 mA helium ions from 5 MeV/u to 10 MeV/u 136
5.24 PMQ parameters of the DTL1 for acceleration of 30 mA helium ions from 5 MeV/u to 7.1 MeV/u 136
5.25 PMQ parameters of the DTL2 for acceleration of 30 mA helium ions from 7.1 MeV/u to 10 MeV/u 137
5.26 Beam parameters of the DTL1 and DTL2 for acceleration of 30 mA helium ions from 5 MeV/u to 10 MeV/u 138
5.27 RF and geometry parameters of ERC used for ramping the energy and DEB used for reducing energy spread of helium ions before injection into therapy synchrotron 142
5.28 Beam parameters of ERC used for ramping the energy and DEB used for reducing the energy spread of helium ions before injection into the therapy synchrotron . 143
5.29 Comparison between QA-DTL and IH-DTL for helium ion acceleration 144
5.30 Overview of Alvarez-type linac configuration for helium ion acceleration . . . 145
5.31 RF and geometry parameters of the QA-DTL for helium ion acceleration from 1 MeV/u to 7.1 MeV/u 146
5.32 PMQ parameters of the QA-DTL for helium ion acceleration from 1 MeV/u to 7.1 MeV/u 147
5.33 Beam parameters of the QA-DTL for helium ion acceleration from 1 MeV/u to 7.1 MeV/u 148

LIST OF FIGURES

2.1 Schematic representation of a typical ion source and linac. 31
2.2 Layout of the particle therapy facility in Heidelberg (Source: [41]). 33
2.3 Sections of the (a) IH-DTL and (b) S-IH-DTL linac structures. 34
2.4 Sections of the (a) DTL and (b) QA-DTL linac structures. 35
2.5 Layout of the HITRI*plus* linac. 36
2.6 Layout of the NIMMS linac. 37
2.7 Schematic representation of the linac configuration for radioisotope production. 37

3.1 Field configuration of (left) TE_{11}, (middle) TM_{01}, and (right) TE_{21} modes within a cylindrical waveguide (adapted from [71]). 41
3.2 Cutoff frequencies of the first 14 TE and TM modes of a cylindrical resonator relative to the cutoff frequency of the dominant TE_{11} mode (adapted from [70]). 43
3.3 (a) Magnetic field distribution of TM_{01p} family modes; (b) Electric field distribution of TE_{11p} family modes; (c) Electric field distribution of TE_{21p} family modes; Simulations were performed on a cylindrical resonator using CST Studio Suite. 43
3.4 Electric field with a crest in the middle of the gap (adapted from [45]). 44
3.5 Dispersion curve of a linac structure containing eleven coupled cells. 48
3.6 Standing wave modes suitable for particle acceleration in multi-cell coupled cavities (adapted from [77]). 49
3.7 Accelerating field with illustrated stable and unstable regions. The synchronous phase has a negative value ($\phi_s < 0$). 51
3.8 Longitudinal phase space with stable trajectory (green line) and unstable trajectory (red line) separated by the separatrix (blue line). 53
3.9 Twiss ellipse in horizontal phase space with characteristic points. 56
3.10 Beam envelope in the horizontal plane (teal) and vertical plane (orange), along with Twiss ellipses plotted at the center of each element in the $FODO$ lattice. The phase advance per cell is 90 degrees. 57
3.11 Beam distribution in horizontal phase space with: (a) 4D-KV distribution; (b) 6D-Uniform distribution; (c) 6D-Parabolic distribution; (d) 6D-Gaussian distribution. All of the beam distributions have the same rms emittances. 61
3.12 (a) The section of one cell of DTL; (b) A drift tube with PMQ within DTL. . . 62
3.13 The 3D model of DTL. 62

3.14 Comparison between different QA-DTL configurations and DTL (adapted from [15]). 64
3.15 One super-period of QA-DTL with periodicity factor of two. 64
3.16 The 3D model of QA-DTL featuring super-periods with the periodicity factor of two. 64
3.17 (a) The section of one cell of H-mode cavity; (b) A drift tube within H-mode drift tube linac. 65
3.18 The 3D model of IH-DTL. 66
3.19 The 3D model of S-IH-DTL. 66
3.20 (Left) Twiss ellipses within the DEB in the presence of voltage with different amplitudes; (Right) the voltage with different amplitudes corresponding to the ellipses on the left. The green Twiss ellipse occurs when the DEB is not in operation. 67
3.21 Phase oscillation within the ERC; φ_0 corresponds to the zero-crossing phase. The blue points represent the phase of each beam bunch at the center of the gap. 68
3.22 (Left) Twiss ellipse within the ERC in the presence of an external EM field with different phases in the middle of the gap; (Right) the external EM field corresponding to the ellipses on the left. 68
3.23 (a) π-mode structure (Source: [2]) and (b) 0-mode structure used as DEB or ERC units. 69
3.24 Total cost of the structure as a function of the accelerating field, with the emphasis on the minimal cost. 71

4.1 (a) Triangular mesh of a two-cell structure generated with Automesh; (b) EM field distribution obtained after applying the Fish solver to the output data provided by Automesh. 76
4.2 (a) The 3D model, (b) the electric field distribution, and (c) the magnetic field distribution, created in CST Studio Suite. 77
4.3 Interface of A-GUI used for optimization of DTL cells. 79
4.4 Interface of QA-GUI used for the optimization of QA-DTL super-periods. . . . 80
4.5 (Top) First or last sub-cell of QA-DTL super-period; (bottom) middle sub-cell of QA-DTL super-period or cell of DTL; with geometry parameters: L_s - Stem diameter, L_g - Gap length, L_c - Cell length, R_{cav} - Cavity radius, R_{dt} - Drift tube radius, R_c - Corner radius, γ - Face angle, R_o - Outer nose radius, L_f - Flat edge length, R_i - Inner nose radius, R_b - Bore radius (adapted from [98]). Index s exists only in QA-DTL and denotes the shorter DT, while the index l exists in both QA-DTL (for the longer DT) and DTL (for every DT). 83
4.6 The impact of different gap lengths on the effective shunt impedance per unit length, maximum electric field in the cell, and resonant frequency of the cell. The rest of the parameters are fixed: R_{cav} = 25 cm, γ = 10 $^\circ$ and L_c = 10 cm. . . 84

4.7 The impact of different cavity radii on the effective shunt impedance per unit length, maximum electric field in the cell, and resonant frequency of the cell. The rest of the parameters are fixed: L_g = 2 cm, γ = 10 ° and L_c = 10 cm. . . . 84
4.8 The impact of different face angles on the effective shunt impedance per unit length, the maximum electric field in the cell, the resonant frequency of the cell, and space for the PMQ within the DT. The rest of the parameters are fixed: L_g = 2 cm, R_{cav} = 25 cm and L_c = 10 cm. 85
4.9 Algorithm for designing the most optimal DTL and QA-DTL for the highest effective shunt impedance per unit length. 86
4.10 Algorithm for optimizing gap length to achieve the highest effective shunt impedance per unit length. 87
4.11 Algorithm for the optimization of the face angle to achieve the highest effective shunt impedance per unit length. 88
4.12 Algorithm for adjusting the cavity radius to achieve the resonant frequency. . . 89
4.13 Algorithm for adjusting the gap length to achieve the resonant frequency. 89
4.14 Algorithm for designing the IH-DTL for the highest effective shunt impedance per unit length. 91
4.15 Algorithm for designing undercut of H-mode type structures. 92
4.16 The section of the H-mode type cell with highlighted undercuts. 92
4.17 Algorithm for designing the S-IH-DTL for the highest shunt impedance per unit length. 93

5.1 Electric field distribution in QA-DTL for carbon ion acceleration from 0.7 MeV/u to 5 MeV/u, simulated with Poisson/SUPERFISH codes. 97
5.2 Beam envelopes along the QA-DTL from 0.7 MeV/u to 5 MeV/u for (a) carbon ions and (b) helium ions. For each accelerated ion, the top plot represents transverse beam envelopes in the xz and yz planes, while the bottom plot shows the phase envelope. 101
5.3 Carbon ion phase space (left column) at 0.7 MeV/u and (right column) at 5 MeV/u with the nominal beam current of 0.6 mA within QA-DTL. 102
5.4 Helium ion phase space (left column) at 0.7 MeV/u and (right column) at 5 MeV/u with the nominal beam current of 5 mA within QA-DTL. 102
5.5 (Left and middle)The 3D model of one S-IH-DTL cavity and (right) electric field distribution within S-IH-DTL designed for carbon ion acceleration from 0.7 MeV/u up to 5 MeV/u, simulated with CST Studio Suite. 103
5.6 Axial electric field in (a) first and (b) last S-IH-DTL cavities for carbon ion acceleration from 0.7 MeV/u to 5 MeV/u, simulated with CST Studio Suite. . . 105
5.7 Beam envelopes along the (a) S-IH-DTL with doublets and (b) S-IH-DTL with triplets from 0.7 MeV/u to 5 MeV/u for carbon ions. For each structure, the top plot represents transverse beam envelopes in the xz and yz planes, while the bottom plot shows the phase envelope. 109

5.8 Beam envelopes along the (a) S-IH-DTL with doublets and (b) S-IH-DTL with triplets from 0.7 MeV/u to 5 MeV/u for helium ions. For each structure, the top plot represents transverse beam envelopes in the xz and yz planes, while the bottom plot shows the phase envelope. 110
5.9 Carbon ion phase space (left column) at 0.7 MeV/u and (right column) at 5 MeV/u with the nominal beam current of 0.6 mA within S-IH-DTL with quadrupole doublets. 111
5.10 Carbon ion phase space (left column) at 0.7 MeV/u and (right column) at 5 MeV/u with the nominal beam current of 0.6 mA within S-IH-DTL with quadrupole triplets. 111
5.11 Helium ion phase space (left column) at 0.7 MeV/u and (right column) at 5 MeV/u with the nominal beam current of 5 mA within S-IH-DTL with quadrupole doublets. 112
5.12 Helium ion phase space (left column) at 0.7 MeV/u and (right column) at 5 MeV/u with the nominal beam current of 5 mA within S-IH-DTL with quadrupole triplets. 112
5.13 Electric field distribution in (a) DTL1, and (b) DTL2, for acceleration of 5 mA helium ions from (a) 5 MeV/u to 7.1 MeV/u, and (b) 7.1 MeV/u to 10 MeV/u, respectively, simulated with Poisson/SUPERFISH codes. 113
5.14 Beam envelopes along the (a) DTL1 from 5 MeV/u to 7.1 MeV/u and (b) DTL2 from 7.1 MeV/u to 10 MeV/u for helium ions. For each structure, the top plot represents transverse beam envelopes in the xz and yz planes, while the bottom plot shows the phase envelope. 117
5.15 Helium ion phase space (left column) at 5 MeV/u and (right column) at 7.1 MeV/u with the nominal beam current of 5 mA within DTL1. 118
5.16 Helium ion phase space (left column) at 7.1 MeV/u and (right column) at 10 MeV/u with the nominal beam current of 5 mA within DTL2. 118
5.17 Electric field distribution in DEB used for reducing energy spread of carbon ions before injection into therapy synchrotron, simulated with Poisson/SUPERFISH codes. 119
5.18 Carbon ion phase space (left column) before and (right column) after DEB. . . 121
5.19 Layout of preferred HITRI*plus* linac configuration. Dimensions are given in cm. 124
5.20 Electric field distribution in QA-DTL for helium ion acceleration from 1 MeV/u to 5 MeV/u, simulated with Poisson/SUPERFISH codes. 125
5.21 Beam envelopes along the QA-DTL from 1 MeV/u to 5 MeV/u for helium ions at (a) 5mA (beam for synchrotron) and (b) 30 mA (beam for radioisotope production) of nominal beam current. For each accelerated ion, the top plot represents transverse beam envelopes in the xz and yz planes, while the bottom plot shows the phase envelope. 128

5.22 Helium ion phase space (left column) at 1 MeV/u and (right column) at 5 MeV/u with the nominal beam current of 5 mA within QA-DTL. 129
5.23 Helium ion phase space (left column) at 1 MeV/u and (right column) at 5 MeV/u with the nominal beam current of 30 mA within QA-DTL. 129
5.24 (a) The 3D model of IH-DTL and (b) electric field distribution in IH-DTL for helium ion acceleration from 1 MeV/u to 5 MeV/u, simulated with CST Studio Suite. 130
5.25 Axial electric field in IH-DTL designed for acceleration of helium ions from 1 MeV/u to 5 MeV/u, simulated with CST Studio Suite. 130
5.26 Beam envelopes along the IH-DTL from 1 MeV/u to 5 MeV/u for helium ions with 5 mA of nominal beam current. The top plot represents transverse beam envelopes in the xz and yz planes, while the bottom plot shows the phase envelope. 132
5.27 Helium ion phase space (left column) at 1 MeV/u and (right column) at 5 MeV/u with the nominal beam current of 5 mA within IH-DTL. 134
5.28 Electric field distribution in (a) DTL1, and (b) DTL2, for acceleration of 30 mA helium ions from (a) 5 MeV/u to 7.1 MeV/u, and (b) 7.1 MeV/u to 10 MeV/u, respectively, simulated with Poisson/SUPERFISH codes. 135
5.29 Beam envelopes along the DTL1 from 5 MeV/u to 7.1 MeV/u for helium ions at a beam current of 30 mA. The top plot represents transverse beam envelopes in the xz and yz planes, while the bottom plot shows the phase envelope. 139
5.30 Beam envelopes along the DTL2 from 7.1 MeV/u to 10 MeV/u for helium ions at a beam current of 30 mA. The top plot represents transverse beam envelopes in the xz and yz planes, while the bottom plot shows the phase envelope. 139
5.31 Helium ion phase space (left column) at 5 MeV/u and (right column) at 7.1 MeV/u with the nominal beam current of 30 mA within DTL1. 140
5.32 Helium ion phase space (left column) at 7.1 MeV/u and (right column) at 10 MeV/u with the nominal beam current of 30 mA within DTL2. 140
5.33 Electric field distribution in (a) ERC used for ramping the energy, and (b) DEB used for reducing energy spread of helium ions before injection into therapy synchrotron, simulated with Poisson/SUPERFISH codes. 141
5.34 Helium ion phase space (left column) before and (right column) after ERC. . . 143
5.35 Helium ion phase space (left column) before and (right column) after DEB. . . 143
5.36 Layout of preferred NIMMS linac configuration. Dimensions are given in cm. . 145
5.37 Electric field distribution in QA-DTL for helium ion acceleration from 1 MeV/u to 7.1 MeV/u, simulated with Poisson/SUPERFISH codes. 146
5.38 Beam envelopes along the QA-DTL from 1 MeV/u to 7.1 MeV/u with 30 mA of beam current used for radioisotope production. The top plot represents transverse beam envelopes in the xz and yz planes, while the bottom plot shows the phase envelope. 148

5.39 Helium ion phase space (left column) at 1 MeV/u and (right column) at 7.1 MeV/u with the nominal beam current of 30 mA within QA-DTL. 149
5.40 Layout of preferred (a) HITRI*plus*, (b) NIMMS, and (c) Astatine linac configuration. Dimensions are given in cm. 150

1. Introduction

Particle therapy has emerged as one of the most promising approaches for treating cancer, offering significant advantages over conventional radiotherapy techniques. Unlike X-rays, charged particles such as protons, carbon ions, and helium ions deposit their energy with high precision, minimizing damage to surrounding healthy tissues and maximizing tumor control. Consequently, the global demand for advanced and more accessible particle therapy facilities is steadily increasing. However, the construction and operation of such facilities remain both costly and technologically challenging, necessitating continuous advancements in accelerator technology.

At the heart of a majority of particle therapy centers lies the linear accelerator (linac), a crucial component responsible for accelerating particles before injection into a synchrotron or directly into the treatment beamline. The power efficiency, length, and beam quality of the linac significantly impact the overall performance of the facility. Therefore, optimizing linac structures to achieve higher power efficiency, improved beam dynamics, and reduced structural complexity is essential for the future of particle therapy. This thesis focuses on investigating innovative linac designs that address these challenges, ultimately proposing novel high-frequency linac structure solutions for next-generation accelerator facilities.

Furthermore, the proposed linac structures can be used to produce innovative radioisotopes for imaging and cancer treatment. By optimizing the algorithms and applying them to develop novel linac structures, this thesis contributes to the advancement of linac technology and particle therapy, ensuring its adaptability to future demands.

This thesis is structured to first provide a comprehensive overview of linear accelerating structures and their role in medical applications. It covers the state-of-the-art in linac technology, as well as ongoing international projects and collaborations, such as Heavy Ion Therapy Research Integration *plus* (HITRI*plus*) and Next Ion Medical Machine Study (NIMMS), which aim to improve accelerator-based cancer treatment. Additionally, it discusses the potential of radioisotope production using linacs and the associated technological challenges.

Furthermore, the fundamental theory behind Radio Frequency (RF) acceleration and beam dynamics, with a particular focus on linac structures, is presented. It introduces the electromagnetic field principles governing linac structures, explores key figures of merit, and explains the mechanisms of beam acceleration inside multi-cell standing wave structures. A detailed analysis of beam dynamics within linac structures is also provided, covering longitudinal and transverse beam dynamics, as well as beam distribution considerations.

The simulation software, mathematical models, and optimization algorithms used in this study are introduced. The computational tools employed for RF and beam dynamics simulations are outlined, along with the optimization algorithms developed for designing power-efficient linac structures. Additionally, two Graphical User Interfaces (GUIs) were created to automate the linac design process, enabling more efficient optimization of accelerator parameters.

After introducing the algorithms for designing linac structures, this thesis presents an analysis and comparison of different linac design options. Several structures for carbon ion and/or helium ion acceleration are evaluated, including Alvarez, Quasi-Alvarez, and H-mode linac structures. The feasibility of using linac structures for both synchrotron injection and radioisotope production is investigated, followed by a comparison of the proposed designs and the selection of the most suitable linac configuration for the next-generation linac.

1.1 Aim of the doctoral thesis

This thesis aims to develop highly efficient novel linac structures to serve as injectors for particle therapy synchrotrons and then compare them with existing structures. The developed linac structures are designed to optimize power efficiency and beam quality compared to existing accelerators, ensuring improved performance in clinical settings. The ability to accelerate both carbon and helium ions within a single linac system enhances the flexibility and applicability of the design. The comparison of the developed linac structures with existing accelerators is followed by the selection of the most promising structure for the next-generation linacs.

Beyond its role in cancer treatment, the linac is also envisioned as a versatile system capable of supporting radioisotope production. The demand for medical radioisotopes, particularly for imaging and therapy treatments, continues to rise, necessitating reliable production methods. By enabling high-intensity, precise ion beam acceleration, the proposed linac structure can contribute to the production of radioisotopes commonly used in therapy and diagnostics.

A central objective of this research is to establish a systematic approach for developing an efficient linac structure tailored to the dual-purpose operation of synchrotron injection and radioisotope production. To achieve this, the study introduces a set of algorithms for developing linac structures aimed at maximizing the effective shunt impedance per unit length, an essential parameter influencing energy consumption and acceleration efficiency. These algorithms have been implemented in two graphical user interfaces (GUIs) created by the author, allowing for the automated development of linac structures.

Ultimately, this thesis aims to contribute to the advancement of accelerator technology by providing a linac structure design that meets the evolving needs of modern particle therapy and radioisotope production. This research lays the groundwork for next-generation linacs capable of delivering high-quality ion beams with enhanced efficiency.

1.2 Hypothesis of the research

Building upon the knowledge of recently developed accelerator technologies and modern simulation codes, one can develop less expensive and more flexible linear accelerators than those used so far for ion injection into therapy synchrotrons, which can, at the same time, produce radioisotopes.

1.3 Scope of the doctoral thesis

The scope of the thesis is to develop a novel standing-wave linac structure as an ion injector for cancer therapy synchrotrons that can reduce costs and improve performance with respect to currently used linac structures, and at the same time allow the production of radioisotopes.

1.4 Tasks of the doctoral thesis

In order to achieve the overall goal, the following tasks are established:

1. To investigate existing ion linac structures that could be used as a carbon and helium injector for a cancer therapy synchrotron.
2. To define an optimization methodology for designing linac structures, by maximizing power efficiency and ensuring beam transmission without any loss of particles.
3. To design and optimize different linac structures with the required input and output parameters, to be used as ion injectors for cancer therapy synchrotrons, or for the production of radioisotopes at different energies.
4. To compare the different linac structures designed under task three and select the overall best solution for future carbon and helium cancer therapy facilities.
5. To integrate the designed linac structures into the proposed helium and carbon ion therapy facilities.

1.5 Scientific novelty

This thesis makes a significant contribution to accelerator technologies, with the most impactful achievements as follows:

1. A novel ion linac structure has been developed as an injector for cancer therapy synchrotrons, offering improved output beam parameters compared to currently used Interdigital H-mode Drift Tube Linac (IH-DTL) injectors.

2. The developed optimization tools are not limited to linac structures used as injectors for cancer therapy synchrotrons, but can also be applied to ion linac designs studied in other fields.

1.6 Practical significance and applications

1. The Alvarez-type linac configuration, composed of the developed Quasi-Alvarez Drift Tube Linac (QA-DTL) and two Alvarez Drift Tube Linac (DTL) cavities, offers a shorter, improved linac solution for future particle therapy facilities, providing higher beam quality with comparable power consumption to IH-DTL based solutions.

2. In a stand-alone, the proposed Alvarez-type linac configuration can be utilized for the production of innovative radioisotopes with a high-current beam at a lower cost compared to existing solutions.

3. The developed Alvarez-type linac configuration is part of the general design of the HITRI*plus* carbon linac[1] and the NIMMS helium linac[2]. Due to its performance presented in this thesis, the developed linac configuration was chosen as the injector for the future Advanced Particle Therapy Center for the Baltic States[3].

1.7 Research Methodology

In order to successfully reach the aim of this thesis, a well-organized research methodology was required. The research methodology is structured into five essential steps to develop optimized accelerating structures and integrate them into the linac of future ion therapy facilities.

The first step is primarily focused on a comprehensive literature review, which provides insights into the state-of-the-art and the latest technologies employed in the field of ion linear accelerators. To successfully accomplish this step, a wide range of sources were consulted, including journal papers, conference proceedings, patents, EU-funded projects, and scientific database searches performed on linear accelerator technologies (e.g., Scopus and Web of Science). Additionally, during the three-year-long stay at CERN, continuous access to the world-leading experts in the field of accelerator technologies was essential for gaining an in-depth understanding of linear accelerators and identifying key challenges and opportunities that guided the direction of this research.

The second step explores the limitations and challenges in conventional Alvarez DTL design such as acceleration of low-velocity particles (the current bottom limit of 1 MeV/u was reported in [1], but in practice, they are usually used at energies from 3 MeV/u), the reduction of expensive and difficult-to-produce components (e.g., quadrupole magnets), and the overall cost

[1]Website: https://www.hitriplus.eu
[2]Website: https://nimms.web.cern.ch
[3]Link: https://link.springer.com/article/10.1007/s12553-024-00875-2

of the structures, as well as in IH-DTL design, such as the improvement of beam quality. Based on these findings, an overall performance comparison of different linac structures for acceleration of low-velocity particles is presented in Table 1.1.

Table 1.1: Performance comparison of different linac structures for acceleration of low-velocity particles

	Power efficiency	**Structure cost**	**Beam quality**
DTL	Medium	Bad	Good
IH-DTL	Good	Good	Medium
New design	Medium	Good	Good

The third step involves the development of an optimization methodology for the linac structure in the form of optimization algorithms. The developed algorithms are then validated using the input parameters (i.e., input and output energies, resonant frequency, and accelerating field) used in the design of an existing, well-established linac structure - LINAC4 at CERN. The optimized geometry achieved with the developed algorithms was benchmarked against published LINAC4 geometry [2], demonstrating strong agreement. Furthermore, the developed algorithms are refined to provide all the necessary information for achieving a power-efficient linac structure with exceptional beam performance, building upon the concepts established in the second step.

The fourth step is the design phase of the proposed linac structures, which combines the knowledge gained from the first three steps and results in structures with optimized geometry and improved beam parameters compared to conventional designs. To enhance the efficiency of the design process, several commercial tools were employed:

- Electromagnetic (EM) simulation software that computes and visualizes the electric and magnetic field distributions within the accelerating structure. In the case of Alvarez-type DTL structures, the two-dimensional (2D) software was used (e.g., Poisson/SUPERFISH codes [3]), while for H-mode type DTL structures, the three-dimensional (3D) EM simulation software was utilized (e.g., CST Studio Suite [4]).

- Multi-particle simulation software, TraceWin [5], was used to perform beam dynamics analysis and assess beam quality within the designed structures.

To further increase efficiency during the design process, the author developed additional optimization tools in the C# programming language and integrated them into a graphical user interface (GUI). These tools are based on the geometry optimization algorithms developed in the third step and utilize the aforementioned commercial software to obtain key linac parameters for further analysis and comparison. The developed tool iteratively optimizes the geometric design of the linac structure until the maximum effective shunt impedance per unit length is achieved, corresponding to the structure with the highest power efficiency. A key advantage of the developed tool is its applicability beyond medical purposes and the scope of this thesis,

extending to any field that requires the design of low-energy linac structures for ion acceleration. It is also worth noting that the development of these codes required approximately three months, while the overall time savings during the design process amounted to approximately six months.

The fifth and final step involves a comparison between the linac structure developed in step four and conventional designs currently used in ion therapy facilities. The comparison is based on power efficiency, length, and beam performance. During this step, the developed QA-DTL is integrated with designed DTL structures into a complete linac configuration with low power consumption and high beam quality without any beam loss.

2. Linear Accelerating Structures for Medical Applications

In this chapter, the state-of-the-art linac structures used for ion acceleration are presented. This is followed by an overview of linac structures currently used in particle therapy facilities as synchrotron injectors. Subsequently, the framework for the activities described in this thesis is provided by Heavy Ion Therapy Research Integration *plus* (HITRI*plus*), a European Commission-funded project under Horizon 2020 aimed at developing new technologies for heavy-ion therapy (particularly carbon ions), and Next Ion Medical Machine Study (NIMMS), a CERN initiative for the development of new accelerator technologies for cancer treatment. Additionally, the possibility of producing radioisotopes using only the linac configuration proposed in this thesis is elaborated, along with a list of producible radioisotopes.

2.1 State-of-the-art

Most circular particle accelerators require a linac as an injector, making it a crucial component. Today, there are more than 30,000 particle accelerators worldwide, of which half are radiotherapy electron linacs used in hospitals for the production of X-rays for cancer treatment [6]. Linacs for relativistic particles, like electrons, are usually high-frequency (GHz range) traveling wave structures, such as Disk-Loaded Traveling Wave Structure (DLTWS) [7] or Coupled-Cavity Traveling Wave Tube (CCTWT) [8]. In contrast, linacs used for the acceleration of heavier particles, which become relativistic only at high energy, such as protons and other ions heavier than protons, consist of a pre-accelerating and beam-bunching structure, such as a Radio Frequency Quadrupole (RFQ), and one or more linac structures at lower frequency (MHz range), depending on the application and desired output energy, as shown in Figure 2.1.

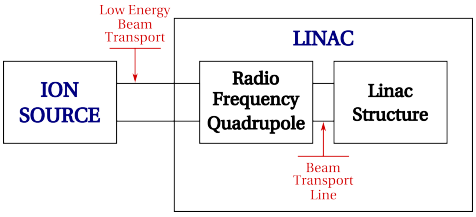


Figure 2.1: Schematic representation of a typical ion source and linac.

Linac structures used for the acceleration of non-relativistic particles are often classified based on their electromagnetic mode of operation. The following is a list of ion linac structures that are either currently in operation or were proposed but never built:

1. Alvarez Drift Tube Linac (DTL), TM mode, protons and heavy ions, 108 - 352 MHz, 1.4 - 50.3 MeV/u [2, 9–11];
2. Quasi-Alvarez Drift Tube Linac (QA-DTL), TM mode, lead ions and carbon ions, 203 - 750 MHz, 0.24 - 7 MeV/u [12–16];
3. Separated-type Drift Tube Linac (SDTL), TM mode, protons, 324 - 432 MHz, 50 - 300 MeV/u [17, 18];
4. Side-Coupled Drift Tube Linac (SCDTL), TM mode, protons, 704 - 3000 MHz, 7 - 160 MeV/u [19–22];
5. Cell-Coupled Drift Tube Linac (CCDTL), TM mode, protons, 352 MHz, 40 - 120 MeV/u [23–26];
6. PI-Mode Structure (PIMS), TM mode, protons, 352 MHz, 102 - 160 MeV/u [27, 28];
7. Split-Ring Resonator (SRR), TM mode, heavy ions, 145 MHz, 4.7 - 30.8 MeV/u [29];
8. Annular-ring Coupled Structure (ACS), TM mode, protons, 972 MHz, 181 - 400 MeV/u [30];
9. Interdigital H-mode Drift Tube Linac (IH-DTL), TE mode, protons and carbon ions 217 - 325 MHz, 0.4 - 7 MeV/u [31–36];
10. Alternating Phase Focusing Drift Tube Linac (APF-DTL), TE mode, heavy ions, 108 MHz, 0.3 - 1.4 MeV/u [37, 38];
11. Separated function (tanks) Interdigital H-mode Drift Tube Linac (S-IH-DTL), TE mode, heavy ions, 105 MHz, 0.15 - 1.5 MeV/u [39];
12. Cross-bar H-mode Drift Tube Linac (CH-DTL), TE mode, protons, 325 MHz, 11.7 - 24.3 MeV/u [40];

Usually, the criterion for choosing the linac structure for a given application is to select the most power efficient option from the provided list, based on the desired particle, energy range, and operational mode. For the medical application discussed in this thesis, the candidates are the DTL and its modification (QA-DTL), followed by the IH-DTL and its modification (S-IH-DTL).

2.2 Linac structures used in particle therapy nowadays

The layout of a typical particle therapy facility, like the one in Heidelberg, is shown in Figure 2.2, highlighting the position of the linac and its size in comparison with the other components of the facility.

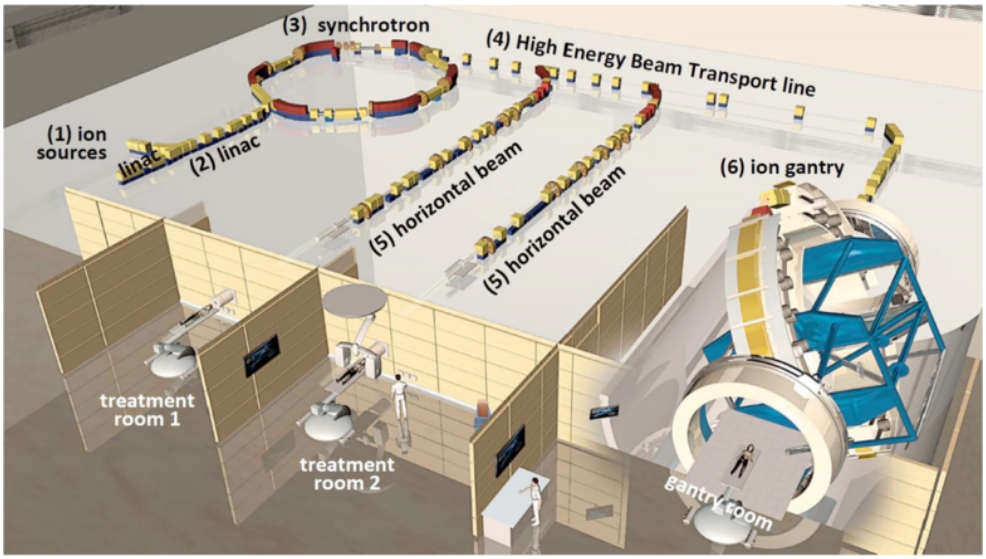


Figure 2.2: Layout of the particle therapy facility in Heidelberg (Source: [41]).

The linac structure within a particle therapy center must be compact, energy-efficient, and have low operational and maintenance costs. As noted in Section 2.1, the most efficient linac structures for the acceleration of low-velocity ions are the DTL, QA-DTL, IH-DTL, and S-IH-DTL. Moreover, the initial acceleration of protons or particles heavier than protons within the particle therapy facilities nowadays is usually done with either the DTL or IH-DTL. Both have proven to be viable acceleration structures over the last few decades, but unfortunately, neither is perfect.

Only four particle therapy centers that use carbon ions for patient cancer treatments currently exist in Europe. All four of them use the IH-DTL structure as a synchrotron injector due to its high power efficiency. The IH-DTL, which was developed as a carbon injector for cancer therapy at GSI from 1993 to 1997 [42], has not undergone significant developments and improvements in the field of medical applications since then. However, it has been used as a synchrotron injector in all carbon ion cancer therapy facilities in Europe: MedAustron in Austria [36], Marburg Ion-beam Therapy Center (MIT) in Germany [43], Heidelberg Ion-beam Therapy Center (HIT) in Germany, and Centro Nazionale di Adroterapia Oncologica (CNAO) in Italy [44]. In all of the mentioned facilities, the injectors operate at 217 MHz. Since the effective shunt impedance per unit length, and hence power efficiency of the normal conducting structures, scales as $ZT^2 \propto \sqrt{f}$ [45], one way of improving the IH-DTL is to increase its frequency. The manufacturing process

of an IH-DTL operating at frequencies higher than 217 MHz becomes complex and, at some point, impossible due to mechanical limitations and tolerances when low-energy particles are accelerated. To overcome this problem, the modification of the IH-DTL is necessary, leading to the introduction of the S-IH-DTL. The sections of the IH-DTL and S-IH-DTL are shown in Figure 2.3.

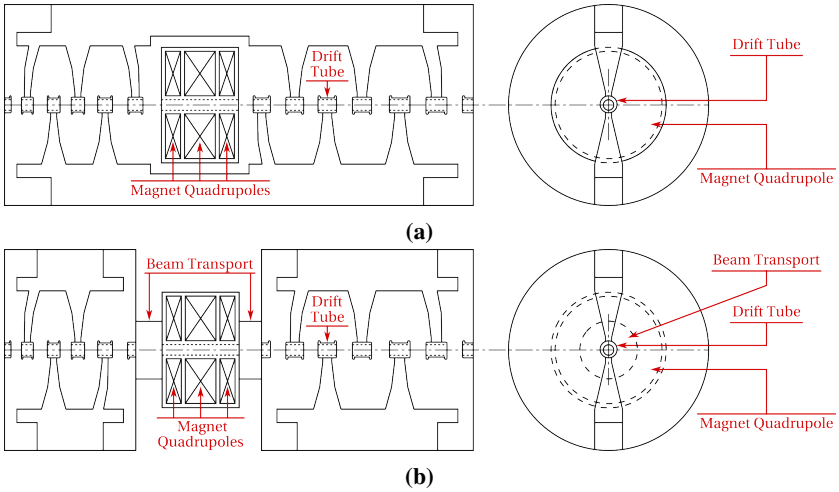


Figure 2.3: Sections of the (a) IH-DTL and (b) S-IH-DTL linac structures.

Detailed analysis and design processes from both radio frequency (RF) and beam dynamics perspectives, regarding the IH-DTL and S-IH-DTL, are presented in Subsection 4.3.2. On the other hand, due to the specific geometry and lack of transverse focusing magnets in each drift tube, there is currently no carbon injector that is comparable with the IH-DTL in terms of power consumption. Also, it is important to mention that both IH-DTL and S-IH-DTL, as will be explained in Subsection 3.3.3, operate in a mode characterized by a longitudinal magnetic field (H-mode, or TE mode).

In contrast, the DTL operating in a mode characterized by a longitudinal electric field (E-mode, or TM mode) has proven to be a reliable linac structure through its implementation as a proton injector for synchrotrons in leading particle accelerator research facilities around the world, such as the *Conseil Européen pour la Recherche Nucléaire* (CERN) [2], the *Relativistic Heavy Ion Collider* (RHIC) [46], the *European Spallation Source* (ESS) [47], and others.

Unfortunately, the DTL has not received much recognition as a carbon injector for synchrotrons due to its low power efficiency for low-velocity particles. To overcome this issue, the DTL has to be modified to become suitable as a carbon injector. This thesis aims to conduct a detailed study of the QA-DTL, an evolution of the DTL for low-velocity particles, and emphasize its potential and the recognition it deserves. The introduction of the QA-DTL will pave the way for the use of Alvarez-type structures as carbon injectors. The sections of the DTL and QA-DTL are shown in Figure 2.4.

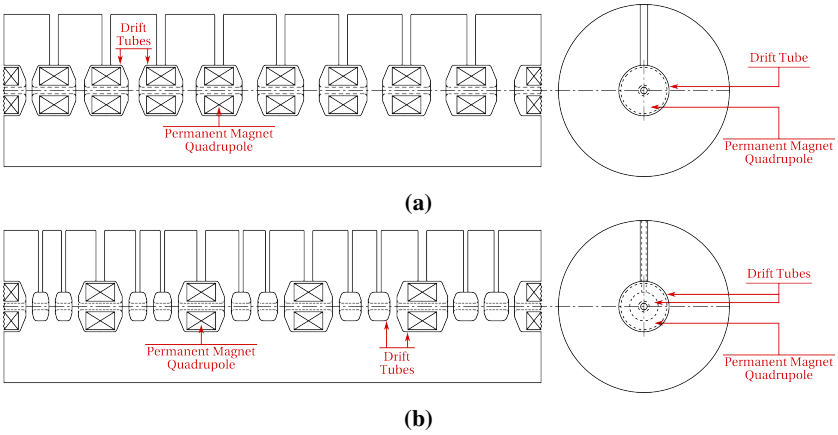


Figure 2.4: Sections of the (a) DTL and (b) QA-DTL linac structures.

The RF design steps and detailed analysis of beam dynamics are presented in Section 4.3.1 for both the DTL and QA-DTL. Another purpose of this thesis is to present the designs of the QA-DTL, which accelerates carbon and helium ions in the same energy range as the IH-DTL while operating at higher frequencies. The benefit of resonating at higher frequencies is the reduction in cavity size, resulting in lower power consumption, and enabling the use of various types of RF source amplifiers. Both DTL and QA-DTL, as will be explained in Subsections 3.3.1 and 3.3.2, operate in a mode characterized by a longitudinal electric field.

2.3 HITRI*plus* project

Heavy Ion Therapy Research Integration *plus* (HITRI*plus*) has the goal to integrate and propel medical and biophysics research on cancer treatment with heavy ion beams and at the same time develop its sophisticated instruments [48].

According to Grant Agreement No. 101008584, the HITRI*plus* project is coordinated by a consortium of 18 leading facilities in the European accelerator community. It consists of 13 Work Packages (WPs), each divided into a specific number of tasks [48]. Specifically for this thesis, the relevant WP is WP7, with a focus on Task 4. Task 7.4 addresses the improvement of injector linac design and is carried out by the Bevatech GmbH (BEVA) - CERN team, with contributions from the South East European International Institute for Sustainable Technologies (SEEIIST). The activities within this task involve developing a conceptual design of a multi-ion injector and obtaining preliminary beam dynamics results, followed by performance comparison with existing injectors. In order to fulfill the requirements of Task 7.4, HITRI*plus* has developed its linac layout, as shown in Figure 2.5.

The beams for the HITRI*plus* linac are provided by two ion sources: a beam of carbon ions and a beam of helium ions. The linac should be composed of three distinct sections. The first section contains an RFQ and a linac structure of any type capable of accelerating both carbon

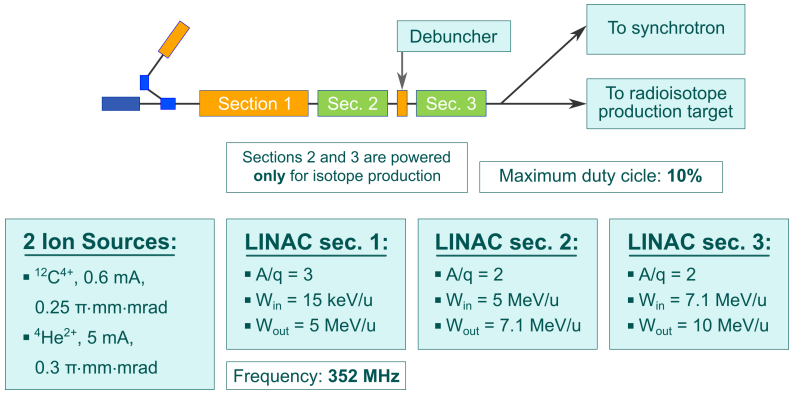


Figure 2.5: Layout of the HITRI*plus* linac.

and helium ions up to 5 MeV/u. The second and third sections contain only linac structures dedicated to the acceleration of helium ions from 5 MeV/u to 7.1 MeV/u and from 7.1 MeV/u to 10 MeV/u, respectively. The transition energy between the second and third sections is set at 7.1 MeV/u, primarily due to the production of 211-Astatine, one of the most promising alpha-emitting radioisotopes for cancer treatment [49]. In other words, the first section serves solely as an injector for the cancer therapy synchrotron, while the second and third sections are dedicated exclusively to radioisotope production. One of the three linac designs presented in this thesis has been developed under the HITRI*plus* project. This particular design is suitable as a carbon injector for the SEEIIST particle therapy center, a research facility dedicated to cancer treatment and biomedical investigations [50].

2.4 NIMMS collaboration

In 2019, CERN launched the Next Ion Medical Machine Study (NIMMS) with the goal of developing cutting-edge accelerator technologies for a new generation of compact and cost-efficient ion therapy facilities [51]. The primary focus of NIMMS is to advance the use of particles heavier than protons, as proton-based installations are already commercially available. In this context, NIMMS has initiated the design of a helium linac to serve as an injector for a therapy synchrotron and, in parallel, for radioisotope production. The layout of the NIMMS linac is shown in Figure 2.6.

The NIMMS linac is powered by one of two available ion sources, providing either helium ions or deuterons. Similar to the HITRI*plus* linac, the ion source is followed by three accelerating sections. All three sections must be capable of accelerating both types of particles provided by the ion sources. The first section accelerates the ions to an energy of 5 MeV/u, which is used either for helium injection into a cancer therapy synchrotron or for radioisotope production with helium ions or deuterons - depending on the demand. The next two sections are also capable of accelerating both helium ions and deuterons but are dedicated solely to radioisotope production.

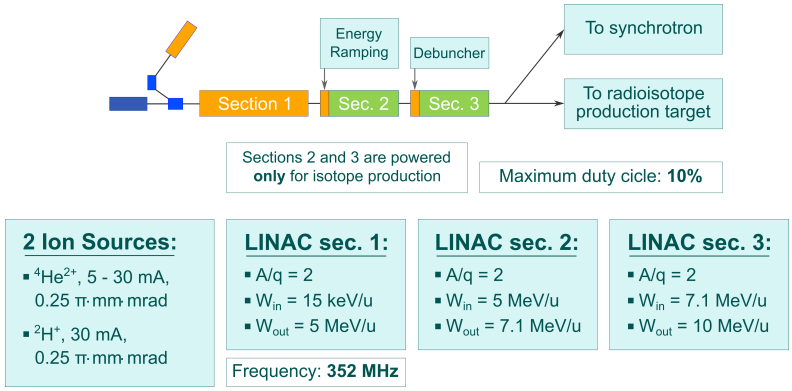


Figure 2.6: Layout of the NIMMS linac.

The second section accelerates both ions up to 7.1 MeV/u, while the final section accelerates them to 10 MeV/u. To maximize radioisotope production, the linac must achieve acceleration of both helium ions and deuterons, each with a nominal beam current of 30 mA with 100% beam transmission. Furthermore, to enable more efficient injection into the therapy synchrotron, a debunching cavity is required. The linac structure designed within NIMMS, and presented in this thesis, is adapted as a helium injector for the future Advanced Particle Therapy Center for the Baltic States [52].

2.5 Radioisotope production with linac

Depending on market demand, the linac structures proposed in this thesis can produce radioisotopes with helium ions or deuterons for diagnostic and therapeutic purposes, by only changing the ion source. The linac configuration for radioisotope production is shown in Figure 2.7.

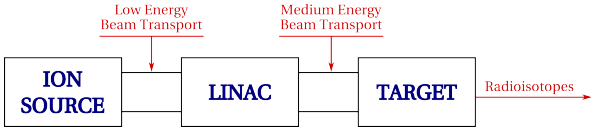


Figure 2.7: Schematic representation of the linac configuration for radioisotope production.

The NIMMS linac, presented in Section 5.2, can provide 30 mA of helium ions and deuterons at energies of 5 MeV/u, 7.1 MeV/u, and 10 MeV/u. The International Atomic Energy Agency (IAEA) has compiled a list of several dozen radioisotopes used as tracers in the physical and biological sciences [53]. A list of promising radioisotopes for use in diagnostics and therapeutics, extracted from [53], that can be produced by the linac structure with helium ions and/or deuterons, is presented in Table 2.1.

Table 2.1: List of prospective radioisotopes for use in diagnostics and therapeutics, producible using a linac that accelerates helium ions and/or deuterons

Radio-isotope	Half-time	Use	Production reaction	Suitable linac energy [MeV/u]	Refer-ences
^{18}F	109.8 min	PET	^{16}O(α, p)^{18}F ^{20}Ne(d, α)^{18}F	10 5	[54] [55]
^{64}Cu	12.7 h	β^- therapy AERT PET	^{64}Ni(d, 2n)^{64}Cu	7.1	[56]
^{67}Cu	61.8 h	$\beta-$ therapy SPET	^{64}Ni(α, p)^{67}Cu	5	[57]
^{68}Ge	270.9 d	*Generator for* ^{68}Ga - PET	^{66}Zn(α, 2n)^{68}Ge	7.1	[58]
^{89}Zr	78.4 h	PET	^{89}Y(d, 2n)^{89}Zr	7.1	[59]
^{103}Pd	17 d	AERT Brachytherapy	^{103}Rh(d, 2n)^{103}Pd	7.1	[60]
^{123}I	13.2 h	SPECT	^{121}Sb(α, 2n)^{123}I ^{122}Te(d, n)^{123}I	7.1 5	[61] [62]
^{177}Lu	6.6 d	β^- therapy	^{176}Yb(d, n)^{177}Lu	5	[63]
^{211}At	7.2 h	TAT SPECT	^{209}Bi(α, 2n)^{211}At	7.1	[64, 65]

Courtesy of K. Paļskis

The reputable U.S.-based company NUSANO has provided a list of radioisotopes currently in high demand, some of which are shown in Table 2.1 [66]. From Table 2.1, PET (Positron Emission Tomography) and SPECT (Single Photon Emission Computed Tomography) are widely used methods for functional patient imaging (diagnostics). PET produces high-quality three-dimensional images, while SPECT generates a series of two-dimensional projections that are used to reconstruct three-dimensional images [67, 68].

On the other hand, radioisotopes that decay by beta-particle emission (used in β^- Therapy), alpha-particle emission (used in Targeted Alpha Therapy - TAT), and electron capture, leading to the emission of Auger electrons (used in Auger Electron-based Radioisotope Therapy - AERT), are suitable for radioisotope therapy (therapeutics) due to their short range in tissue [69]. Additionally, radioisotopes that decay via low-energy gamma photon emission can be employed in brachytherapy, a method involving the physical implantation of isotopes.

2.6 Conclusions

In this chapter, the state-of-the-art has been reviewed, highlighting the various types of linac structures that are currently available and in use. Among them, two commonly employed linac structures in particle therapy facilities (the IH-DTL and DTL) have been discussed, as they form the core of this study. The chapter then elaborated on the HITRI*plus* project and the NIMMS collaboration, emphasizing their overall designs and the thesis's contribution to them. Lastly, an overview of radioisotope production is provided, including a list of promising radioisotopes for diagnostics and therapeutics that can be produced using linac structures with helium ions and deuterons presented in this thesis.

3. RF and Beam Dynamics Theory of Linac Structures

In this chapter, the physics behind electromagnetic waves, the behavior of the beam inside linac structures, the software used for complex simulations, and the linac economics are presented. The chapter consists of four sections, each dedicated to a corresponding topic. The first section explains the fundamental concepts necessary for understanding electromagnetic wave properties within the linac structure, addressing the question: *"How do electromagnetic waves affect the beam during its acceleration within the linac structure?"*. The second section focuses on beam behavior inside linac structures during their acceleration, while the third section describes the developed linac structures presented in this thesis, applying the theoretical framework established in the first two sections of this chapter. Lastly, the fourth section focuses on the linac economics of Alvarez-type linac structures used for the acceleration of low-velocity ions.

3.1 Electromagnetic field theory for linac structures

In the interest of designing any linac structure ready for manufacturing, the physics of electromagnetic (EM) wave propagation and its influence on the beam must first be understood. Therefore, this section aims to provide all the necessary information required for successful beam acceleration from the beginning to the end of the linac structure without losing any particles. The mathematical representation of EM field modes that can exist within a linac structure, the mathematical tools used to explain energy transfer from the external EM field to the beam, the important fundamental properties of linac structures known as *figures of merit*, as well as acceleration and different operational modes inside standing-wave multi-cell structures, are all presented in this section.

3.1.1 Modes inside linac structures

To understand EM modes within a linac structure, we first consider a cylindrical waveguide. When an external EM field is applied to the cylindrical waveguide, the EM waves can have only electric or magnetic components in the direction of wave propagation (longitudinal plane), but not both at the same time. An EM wave in which the electric field is entirely perpendicular to the direction of propagation is known as a Transverse Electric (TE) mode, whereas a wave in which

the magnetic field is entirely perpendicular to the direction of propagation is called a Transverse Magnetic (TM) mode. Both TE and TM modes can exist at certain discrete frequencies, dictated by the geometry of the waveguide. By enclosing both ends of the cylindrical waveguide, it becomes a cylindrical resonator in which standing waves are established at specific resonant frequencies [70].

Both TM and TE modes are labeled with three subscripts (TM_{mnp} and TE_{mnp}), which are used to identify the variation of the electric and magnetic fields across the cavity. The subscript m (m = 0, 1, 2, ...) represents the number of full-period variations of the field components in the azimuthal direction. The subscript n (n = 1, 2, 3, ...) represents the number of zero-crossings of the axial field components (E_z or H_z, depending on the propagating mode) in the radial direction. Finally, the subscript p (p = 0, 1, 2, ...) indicates the number of half-period variations of the field components in the longitudinal direction. The three most commonly used modes in the field of linear accelerators are TM_{010}, TE_{110}, and TE_{210}, with their representations in the cylindrical waveguide shown in Figure 3.1.

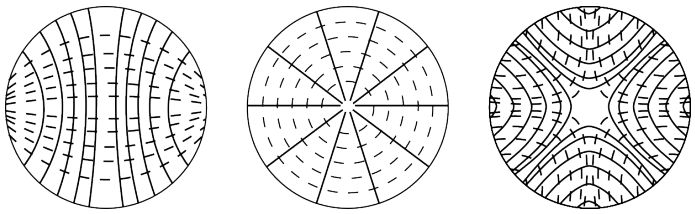


Figure 3.1: Field configuration of (left) TE_{11}, (middle) TM_{01}, and (right) TE_{21} modes within a cylindrical waveguide (adapted from [71]).

The TM mode is a special form of EM wave where the magnetic field has only transverse components, while the electric field, in addition to transverse components, also has a component in the longitudinal direction. The general mathematical expressions for both electric and magnetic field components for TM_{mnp} modes, within a cylindrical resonator, are as follows [70]:

$$H_\theta = -j\omega\varepsilon\frac{a}{x_{mn}}E_1 J'_m\left(\frac{x_{mn}}{a}r\right)\cos(m\theta)\cos\left(\frac{p\pi}{l}z\right), \tag{3.1a}$$

$$H_r = -j\omega\varepsilon\frac{ma^2}{x_{mn}^2 r}E_1 J_m\left(\frac{x_{mn}}{a}r\right)\sin(m\theta)\cos\left(\frac{p\pi}{l}z\right), \tag{3.1b}$$

$$H_z = 0 \tag{3.1c}$$

$$E_\theta = \frac{p\pi}{l}\frac{ma^2}{x_{mn}^2 r}E_1 J_m\left(\frac{x_{mn}}{a}r\right)\sin(m\theta)\sin\left(\frac{p\pi}{l}z\right), \tag{3.1d}$$

$$E_r = -\frac{p\pi}{l}\frac{a}{x_{mn}}E_1 J'_m\left(\frac{x_{mn}}{a}r\right)\cos(m\theta)\sin\left(\frac{p\pi}{l}z\right), \tag{3.1e}$$

$$E_z = E_1 J_m\left(\frac{x_{mn}}{a}r\right)\cos(m\theta)\cos\left(\frac{p\pi}{l}z\right), \tag{3.1f}$$

where ω represents the angular frequency of the wave, a is the radius of the cylindrical resonator, x_{mn} represents the zeros of the Bessel function of the first kind, E_1 is the amplitude of the

electric field, J_m is the Bessel function of the first kind, J'_m represents the derivative of the Bessel function of the first kind, ε is the permittivity of the medium within the resonator, and l is the length of the resonator.

Besides the mathematical representation of TM modes propagation inside linac structures (Equations 3.1a-3.1f), an important parameter is the cutoff frequency. The cutoff frequency is the value above which a certain mode starts to propagate. For the TM mode, the cutoff frequency is defined as [72]:

$$f_c^{TM} = \frac{p_{mn}}{2\pi a\sqrt{\mu\varepsilon}}, \tag{3.2}$$

where p_{mn} represents the root of the Bessel function of the first kind (J_m).

Likewise, the TE mode also represents a special form of EM wave, where the electric field has only transverse components, while the magnetic field, in addition to transverse components, also has a component in the longitudinal direction. The general mathematical expressions for both electric and magnetic field components for TE_{mnp} modes, within a cylindrical resonator, are as follows [70]:

$$H_\theta = -\frac{p\pi}{l}\frac{ma^2}{x'^2_{mn}r}H_1 J_m\left(\frac{x'_{mn}}{a}r\right)\sin(m\theta)\cos\left(\frac{p\pi}{l}z\right), \tag{3.3a}$$

$$H_r = \frac{p\pi}{l}\frac{a}{x'_{mn}}H_1 J'_m\left(\frac{x'_{mn}}{a}r\right)\cos(m\theta)\cos\left(\frac{p\pi}{l}z\right), \tag{3.3b}$$

$$H_z = H_1 J_m\left(\frac{x'_{mn}}{a}r\right)\cos(m\theta)\sin\left(\frac{p\pi}{l}z\right), \tag{3.3c}$$

$$E_\theta = j\omega\mu\frac{a}{x_{mn}}H_1 J'_m\left(\frac{x'_{mn}}{a}r\right)\cos(m\theta)\sin\left(\frac{p\pi}{l}z\right), \tag{3.3d}$$

$$E_r = j\omega\mu\frac{ma^2}{x'^2_{mn}r}H_1 J_m\left(\frac{x'_{mn}}{a}r\right)\sin(m\theta)\sin\left(\frac{p\pi}{l}z\right), \tag{3.3e}$$

$$E_z = 0, \tag{3.3f}$$

where H_1 is the amplitude of the magnetic field, x'_{mn} represents the zeros of the derivative of the Bessel function of the first kind, and μ is the permeability of the medium within the resonator.

Similarly to the TM modes, TE modes also have an expression providing the minimal frequency value above which the modes start to propagate, known as the cutoff frequency. In the case of the TE mode, the cutoff frequency is defined as [72]:

$$f_c^{TE} = \frac{p'_{mn}}{2\pi a\sqrt{\mu\varepsilon}}, \tag{3.4}$$

where p'_{mn} represents the root of the derivative of the Bessel function of the first kind with respect to its argument (J'_m).

The dominant mode for a certain resonator is the mode that has the lowest cutoff frequency. Inside a cylindrical resonator, the dominant mode is TE_{11}. By raising the excitation frequency

after the appearance of the dominant mode, other TE and TM modes appear at certain orders and frequencies. The graphical representation of the cutoff frequencies of the first fourteen TE and TM modes of the cylindrical resonator, relative to the cutoff frequency of the dominant TE_{11} mode, is shown in Figure 3.2.

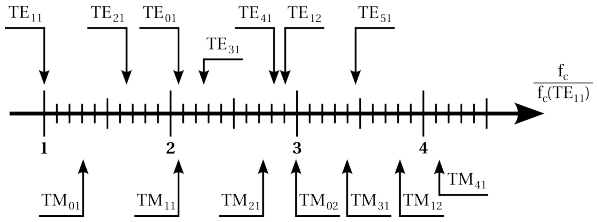


Figure 3.2: Cutoff frequencies of the first 14 TE and TM modes of a cylindrical resonator relative to the cutoff frequency of the dominant TE_{11} mode (adapted from [70]).

Furthermore, in addition to Figure 3.1, the cross-section of the cylindrical resonator showing the magnetic field distribution of TM_{01p} and the electric field distribution of the TE_{11p} and TE_{21p} family modes is shown in Figure 3.3.

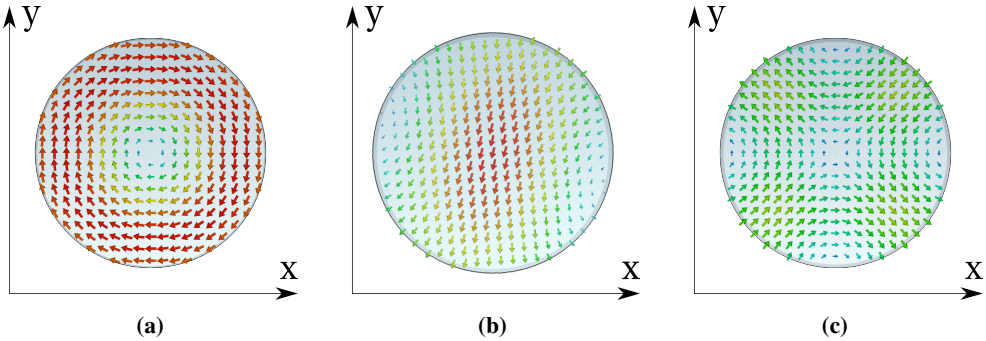


Figure 3.3: (a) Magnetic field distribution of TM_{01p} family modes; (b) Electric field distribution of TE_{11p} family modes; (c) Electric field distribution of TE_{21p} family modes; Simulations were performed on a cylindrical resonator using CST Studio Suite.

3.1.2 Energy gain in linac structure

To achieve a more efficient energy transfer from the external EM field to the beam, drift tubes are introduced within cylindrical resonators (consult Figures 2.3 and 2.4). The neighboring drift tubes concentrate the electric field along the trajectory of the particles in the space between them, making acceleration more efficient. At the same time, drift tubes act as *Faraday cages*, preventing the deceleration of particles when the established field changes polarity. The electric field along the z-axis is as follows [45]:

$$E_z(z,t) = E(z)cos(\omega t + \phi), \tag{3.5}$$

where ω represents the angular frequency of the RF pulse, and ϕ is the phase of the field relative to its crest when $t = 0$. Now, a particle traveling through the gap, as shown in Figure 3.4, will experience an electric field given by Equation 3.5, in a manner described by the following expression:

$$E_z(r = 0, z) = E(0, z)cos\left[\omega \int_0^z v(z)dz + \phi\right], \tag{3.6}$$

where $v(z)$ is the velocity of the particle at position z. The expression $\int_0^z v(z)dz$ can be substituted with $t(z)$, which represents the time when the particle is at position z. At the moment when $t = 0$, the particle is at the origin.

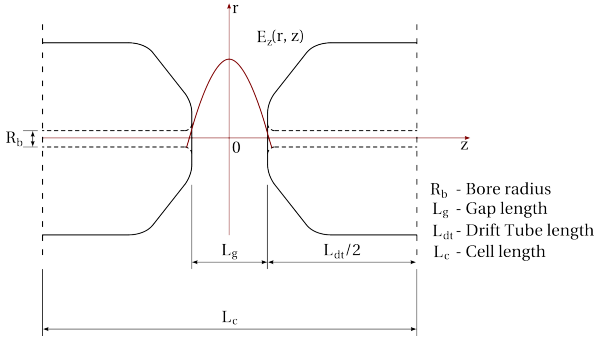


Figure 3.4: Electric field with a crest in the middle of the gap (adapted from [45]).

A cell of a linac structure usually consists of halves of neighboring drift tubes and the space between them, known as the *gap*. Now, consider the case of a cell shown in Figure 3.4, with the field confined within its length. An arbitrary particle with an electric charge q traveling through the gap will experience an energy gain given by [73]:

$$\Delta W = q \int_{-L_c/2}^{L_c/2} E(0, z)cos\left[\omega t(z) + \phi\right]. \tag{3.7}$$

The equation 3.7 can be further simplified, leading to its most compact form, known as the *Panofsky equation*:

$$\Delta W = qE_0L_cTcos(\phi), \tag{3.8}$$

where E_0 represents the average axial electric field amplitude, which can be expressed in terms of the axial RF voltage (V_0) as:

$$E_0 = \frac{V_0}{L_c} = \frac{\int_{-L_c/2}^{L_c/2} E(0, z)dz}{L_c}. \tag{3.9}$$

In Equation 3.8, T is known as the *transit-time factor*, and it is defined as [45]:

$$T = \frac{\int_{-L_c/2}^{L_c/2} E(0,z) cos\left[\omega t(z)\right] dz}{\int_{-L_c/2}^{L_c/2} E(0,z) dz} - tan\phi \frac{\int_{-L_c/2}^{L_c/2} E(0,z) sin\left[\omega t(z)\right] dz}{\int_{-L_c/2}^{L_c/2} E(0,z) dz}. \tag{3.10}$$

The transit-time factor is an important and complex parameter, encapsulating a significant amount of physics. Since the electric field on the axis is time-varying, a particle cannot experience the same energy gain as it would under a constant Direct Current (DC) electric field. The ratio of energy gain in a time-varying RF field to that in a constant DC electric field is known as the transit-time factor.

3.1.3 Linac structure's figures of merit

The fundamental properties used to characterize any linac structure by providing information about its performance are known as *figures of merit*, which are listed below [45].

1. *Impedance of a resonator* - There are four accepted definitions of impedance that are often used interchangeably.

   (a) *Shunt impedance* - (R) provides information about the power dissipation of the resonator (P_d) according to the provided axial voltage (V_0). A particularly important property of shunt impedance is its independence from the excitation level of the resonator. The shunt impedance is defined as:

   $$R = \frac{V_0^2}{P_d}. \tag{3.11}$$

   (b) *Shunt impedance per unit length* (R') is a convenient figure of merit when the resonator is long. It is defined as the ratio of the shunt impedance to the length of the resonator (l):

   $$R' = \frac{R}{l} = \frac{V_0^2}{P_d \cdot l} = \frac{E_0^2}{P_d/l}. \tag{3.12}$$

   (c) *Effective shunt impedance* (Z) is one of the most important figures of merit when accelerating structures are concerned, as it contains information about peak energy gain ($\Delta W_{peak} = qV_0T$). It is defined as the ratio of the square of the peak energy gain to the power dissipation:

   $$Z = RT^2 = \frac{\left(V_0 T\right)^2}{P_d} = \left(\frac{\Delta W_{peak}}{q}\right)^2 \frac{1}{P_d}. \tag{3.13}$$

   (d) *Effective shunt impedance per unit length* (Z' or often ZT^2) – similarly to shunt impedance per unit length, the effective shunt impedance per unit length becomes more important when the resonator is long. This figure of merit is of great importance during the design of linac structures, since in most cases the goal is to maximize the effective shunt impedance per unit length to achieve the highest power efficiency of

the structure. The effective shunt impedance per unit length is defined as the ratio between the effective shunt impedance and the length of the resonator:

$$Z' \equiv ZT^2 = \frac{Z}{l} = \frac{(V_0 T)^2}{P_d \cdot l} = \frac{(E_0 T)^2}{P_d / l}. \tag{3.14}$$

2. *Quality factor* - There are two types of quality factors:

   (a) *Unloaded quality factor* (Q_u) is a dimensionless figure of merit that specifies how underdamped the resonator is. It is proportional to the ratio of stored energy inside the resonator (U) to the dissipated power inside the walls of the resonator per RF cycle, at RF frequency ($\omega = 2\pi f$):

   $$Q_u = \omega \frac{U}{P_d}. \tag{3.15}$$

   (b) *Loaded quality factor* (Q_l) is less useful than the unloaded quality factor. In addition to the power dissipated into the resonator walls, the loaded quality factor also includes external power losses, which arise due to external connections to the resonator or when beam loading is non-negligible - collectively noted as P_{ext}. It is defined as:

   $$Q_l = \omega \frac{U}{P_d + P_{ext}}. \tag{3.16}$$

3. *r over Q* $\left(\frac{r}{Q}\right)$ is an important figure of merit since it does not depend on the surface properties that determine power dissipation, but rather on the resonator geometry. The expression defining *r over Q* is as follows:

   $$\frac{r}{Q} \equiv \frac{Z}{Q_u} = \frac{(V_0 T)^2 / P_d}{\omega U / P_d} = \frac{(V_0 T)^2}{\omega U}. \tag{3.17}$$

4. *Beam power* (P_b) is the fraction of the RF power transferred to the beam due to the beam's interaction with the external field within the resonator. It is proportional to the product of beam current (I_b) and energy gain (ΔW), but inversely proportional to the electric charge of the accelerated particle (q):

   $$P_b = \frac{I_b \Delta W}{q}. \tag{3.18}$$

5. *Kilpatrick field* (E_{kp}) defines the limit of the maximum electric field achievable before the occurrence of RF breakdown [74]. It depends on the resonant frequency of the resonator and is described by the empirical expression (frequency is given in MHz, while the Kilpatrick field is given in MV/m) [75]:

   $$f_{res} = 1.64 \cdot E_{kp}^2 \cdot e^{\frac{-8.5}{E_{kp}}}. \tag{3.19}$$

3.1.4 Acceleration inside standing wave multi-cell structures

The standing wave pattern can be achieved by closing the walls on both sides of the waveguide, creating a resonator, as explained in Subsection 3.1.1. By closing both sides of the resonator, the wave can only be reflected from the conducting walls and cannot propagate outside the resonator. That is, by exciting the EM field inside the resonator, a traveling wave is initially created, which hits the wall when it reaches the end of the resonator and reflects backward with the same frequency and amplitude as the incident wave. Upon meeting, the reflected and incident waves combine, creating a wave with an amplitude twice that of the incident wave. The superposed wave is known as a *standing wave*. Every standing wave is characterized by points where the amplitude of the oscillating field is always zero, known as *nodes*, and points where the field amplitude constantly changes between the minimum and maximum, known as *antinodes*.

Due to the power inefficiency of single-cell resonators when used as linear particle accelerators, coupled multi-cell structures are more widely used, forming chains of cells. In the ideal case, the particles would receive maximal energy if they arrive at each gap at the crest of the RF wave, as shown in Figure 3.4. Unfortunately, due to beam stability reasons (explained in detail in Subsection 3.2.1), the crest of the EM wave is slightly displaced from the middle of the gap, resulting in a slight reduction in the efficiency of the linac structure. Since the particles gain energy in each gap, they become faster while passing through them. To ensure that the crest of the RF wave aligns with each gap when the particles arrive, there are two possible approaches to consider, both of which significantly influence the design process.

The first approach involves designing a linac structure with multiple identical cells separated by conducting walls, each using an individual power supply that allows for the adjustment of the accelerating field phase. While this approach offers flexibility, it is often impractical due to the high operational costs associated with using multiple power sources. However, in cases where multiple ions with different charge-to-mass ratios are accelerated within a single linac structure, the ability to adjust the field inside each cell becomes an important aspect. In such cases, the first approach may be considered.

The second approach involves increasing the length of each cell, which allows the use of a single power source. While this approach is more power-efficient than the first, the length of the cells increases rapidly, making the overall linac structure significantly longer than in the first approach. To implement the second approach, the so-called synchronicity condition must be respected, which simultaneously defines the length of each cell. The synchronicity condition is as follows [76]:

$$L_c = \frac{\beta\lambda}{2\pi}\Delta\phi_c, \tag{3.20}$$

where β is the particle's velocity relative to the speed of light in free space, λ is the RF wavelength, and $\Delta\phi_c$ is the phase shift between two neighboring cells.

Depending on the number of consecutive coupled cells within the linac structure (N), different Standing Wave (SW) modes arise, describing the relative phase difference of field oscillations

in each neighboring cell. The SW modes are constrained by the number of coupled cells, and for visualization purposes, they are typically represented on a dispersion curve ranging from the lowest-frequency mode, known as the *0-mode*, to the highest-frequency mode, known as the π*-mode*. The dispersion curve for eleven coupled cells is shown in Figure 3.5.

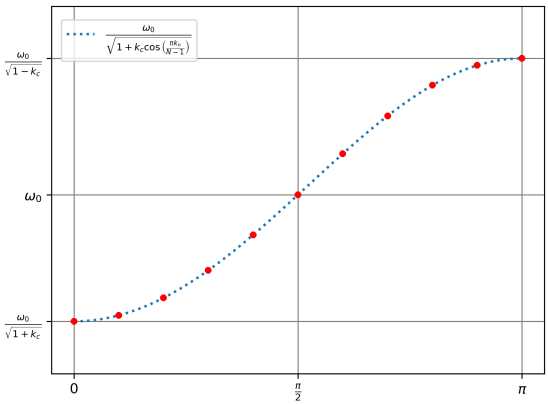


Figure 3.5: Dispersion curve of a linac structure containing eleven coupled cells.

The dispersion curve, as shown in Figure 3.5, is a periodic function described by Equation 3.21 [76].

$$\omega = \frac{\omega_0}{\sqrt{1 + k_c \cos \frac{\pi k_n}{N-1}}}, \tag{3.21}$$

where ω represents the mode angular frequency, ω_0 is the resonant angular frequency of a single cell if it were isolated from the other cells, k_n is an integer known as the mode number, defined within the range $[0, N-1]$, and k_c represents the coupling coefficient. The lowest frequency mode (*0-mode*) and the highest frequency mode (π*-mode*) from the dispersion curve shown in Figure 3.5 are defined as:

$$\omega = \frac{\omega_0}{\sqrt{1 + k_c}} \left(0 - mode\right), \tag{3.22a}$$

$$\omega = \frac{\omega_0}{\sqrt{1 - k_c}} \left(\pi - mode\right). \tag{3.22b}$$

For the acceleration of particles, the three most useful (and practical) SW modes are the 0-mode, $\frac{\pi}{2}$-mode, and π-mode due to their accelerating field distribution. The electric field patterns of these three SW modes are shown in Figure 3.6.

To maintain synchronicity along the cavity during the acceleration process, the length of each cell must satisfy Equation 3.20, depending on the chosen SW mode. Consequently, the

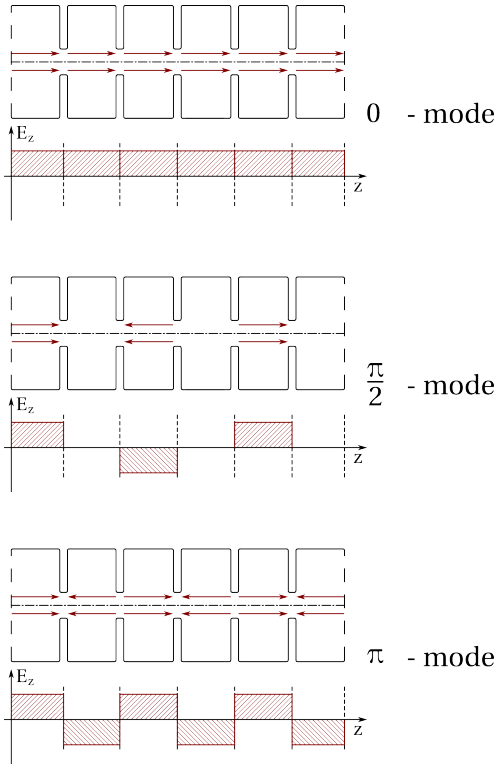


Figure 3.6: Standing wave modes suitable for particle acceleration in multi-cell coupled cavities (adapted from [77]).

length of each cell for the three most practical SW modes present in linac structures is given by:

$$L_c = \beta\lambda\,(0 - mode)\,, \tag{3.23a}$$

$$L_c = \frac{\beta\lambda}{4}\left(\frac{\pi}{2} - mode\right), \tag{3.23b}$$

$$L_c = \frac{\beta\lambda}{2}\,(\pi - mode)\,. \tag{3.23c}$$

3.2 Beam dynamics for linac structures

The following section focuses on several concepts of beam dynamics that will be useful throughout the thesis. A detailed overview of beam dynamics and accelerator physics, in general, can be found in the extensive literature, such as [78–81], to name a few.

Inside the linac structure, the movement of a particle with charge q and velocity $\vec{v} = (v_x, v_y, v_z)$, after experiencing an external electric field $\vec{E} = (E_x, E_y, E_z)$ and magnetic field $\vec{B} = (B_x, B_y, B_z)$, is described by the Lorentz force (Equation 3.24):

$$\frac{d\vec{p_r}}{dt} = q\left(\vec{E} + \vec{v} \times \vec{B}\right), \tag{3.24}$$

where $\vec{p_r} = \gamma_p m_0 \vec{v}$ represents the relativistic momentum of a particle in motion, $\gamma_p = 1/\sqrt{1-\beta^2}$ is the Lorentz factor, and m_0 represents the rest mass of the accelerated particle.

In order to prevent confusion between the variable describing the particle's position in the longitudinal plane (denoted by z) and the beam abscissa within the linac structure, the s notation has to be introduced. By defining the beam abscissa as s, and the particle's velocity in the longitudinal direction as v_z, the Lorentz force from Equation 3.24 can be rewritten as:

$$\frac{d\vec{p_r}}{ds} = \frac{q\left(\vec{E} + \vec{v} \times \vec{B}\right)}{v_z}. \tag{3.25}$$

In the field of linear accelerators, the x and y notations are typically used to indicate the horizontal and vertical directions (transverse planes), respectively, while the z notation is commonly used to indicate the axial direction (longitudinal plane). Considering the aforementioned notations for the transverse and longitudinal planes, the general equations of motion in Cartesian coordinates take the form [82]:

$$\begin{aligned}
\frac{d(\gamma_p\beta_x)}{ds} &= \frac{q}{m_0 c}\left(\frac{dy}{ds}B_z - B_y + \frac{E_x}{v_z}\right), \\
\frac{d(\gamma_p\beta_y)}{ds} &= \frac{q}{m_0 c}\left(B_x - \frac{dx}{ds}B_z + \frac{E_y}{v_z}\right), \\
\frac{d(\gamma_p\beta_z)}{ds} &= \frac{q}{m_0 c}\left(\frac{dx}{ds}B_y - \frac{dy}{ds}B_x + \frac{E_z}{v_z}\right).
\end{aligned} \tag{3.26}$$

3.2.1 Longitudinal beam dynamics within linac structures

Once designed, linac structures will optimally accelerate a single particle within a beam of N_p particles. The particle for which the linac structure is designed is called the *synchronous particle*, and it is always in synchronicity with the accelerating field. The phase of the synchronous particle is defined as the synchronous phase (ϕ_s).

Within the linac community, by convention, the accelerating field varies over time as a cosine function, with the crest at the origin ($\phi = 0$). To prevent the loss of particles during the acceleration of the beam, the important concept of *phase stability* must be defined. There are two possible regions, relative to the crest of the accelerating field, in which the beam can oscillate around the synchronous particle based on its position:

- rising (negative) side near the crest at the origin (region from $-\pi/2$ to 0) and
- falling (positive) side near the crest at the origin (region from 0 to $\pi/2$)

The region between $\pi/2$ and $3\pi/2$ is not considered since the accelerating field in that range is negative, which would decelerate the particles. For better clarification, the field-phase plot is shown in Figure 3.7.

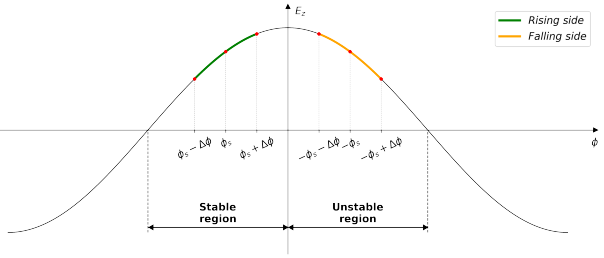


Figure 3.7: Accelerating field with illustrated stable and unstable regions. The synchronous phase has a negative value ($\phi_s < 0$).

In the case where the synchronous particle is positioned on the rising side of the accelerating field near the crest (at ϕ_s), the particles arriving earlier (at $\phi_s - \Delta\phi$) will experience a smaller field amplitude and thus will gain less energy compared to the synchronous particle. On the other hand, the particles arriving later than the synchronous particle (at $\phi_s + \Delta\phi$) will experience a higher field amplitude and therefore will gain more energy than the synchronous particle. Hence, this region is known as the *stable region* - the beam in this region will cluster around the synchronous particle. In the second case, when the synchronous particle is positioned on the falling side of the accelerating field near the crest (at $-\phi_s$), the situation is the opposite of the previous case - particles arriving earlier (at $-\phi_s - \Delta\phi$) will receive stronger acceleration, while the particles arriving later (at $\phi_s + \Delta\phi$) will receive weaker acceleration, which will eventually lead to beam loss, and hence this region is known as the *unstable region*. Therefore, in order to keep the beam stable, the principle of phase stability must be respected, which has as a consequence the positioning of the synchronous particle on the rising side of the accelerating field (Figure 3.7).

Inside linac structures, the motion of a beam consisting of N_p particles is usually represented in six-dimensional (6D) canonical phase space [78, 79]. In 6D phase space, each particle of the observed beam is described by two sets of coordinates - position (x) and momentum (p_r) - which satisfy Hamilton's equations of motion:

$$\frac{\partial x}{\partial t} = \frac{\partial H_{en}(x, p_r, t)}{\partial p_r}, \tag{3.27a}$$

$$\frac{\partial p_r}{\partial t} = -\frac{\partial H_{en}(x, p_r, t)}{\partial x}, \tag{3.27b}$$

where H_{en} is known as the *Hamiltonian*, and it represents the total energy of the particle's oscillations. As mentioned earlier, each particle oscillates around the synchronous particle, so the energy gain slightly differs. Starting from the Panofsky equation (Equation 3.8), which describes

the energy gain of a single particle in each cell within the linac structure, the difference in energy gain relative to the synchronous particle is described as:

$$\Delta W_d = \Delta W - \Delta W_s = qE_0TL_c\left[\cos(\phi) - \cos(\phi_s)\right], \tag{3.28}$$

where ϕ represents the phase of the oscillating particle. Along the path *s*, the variation of Equation 3.28 is calculated as its derivative with respect to *s*:

$$\frac{d}{ds}\Delta W_d = qE_0T\left[\cos(\phi) - \cos(\phi_s)\right]. \tag{3.29}$$

Besides the difference in energy gain of each particle oscillating around the synchronous particle, there is also a difference in their phases, which is defined as:

$$\Delta\phi = \phi - \phi_s. \tag{3.30}$$

Similarly to Equation 3.29, the phase difference between the oscillating particle and the synchronous particle along path *s* is as follows:

$$\frac{d}{ds}\Delta\phi = \frac{\omega}{c}\left[\frac{1}{\beta} - \frac{1}{\beta_s}\right] = -\frac{\omega\Delta\beta}{\beta\beta_s c} \approx -\frac{\omega\Delta\beta}{\beta_s^2 c} = -\frac{\omega\Delta W_d}{2c\beta_s\gamma_s^2\Delta W_s}. \tag{3.31}$$

The final result from Equation 3.31 is obtained under the assumption that the oscillating particle velocity ratio ($\Delta\beta/\beta_s$) is expressed via the energy gain ratio ($\Delta W_d/W_s$) [83]. Equations 3.29 and 3.31 are important in the field of longitudinal beam dynamics, as they fully describe the oscillatory motion of each particle. By combining the previously mentioned equations, the second-order differential equation is obtained:

$$\frac{d^2}{ds^2}\Delta\phi + \frac{\omega qE_0T}{2c\beta_s\gamma_s^2\Delta W_s}\left[\cos(\phi_s + \Delta\phi) - \cos(\phi_s)\right] = 0. \tag{3.32}$$

The solution of Equation 3.32 represents an important result, as it provides the necessary information for describing the motion of a particle in longitudinal phase space, and it has the following form [83]:

$$\frac{\omega}{2c\beta_s\gamma_s^2\Delta W_s}\left\{\frac{\omega\Delta W_d^2}{4c\beta_s\gamma_s^2\Delta W_s} + qE_0T\left[\sin(\phi_s + \Delta\phi) - \Delta\phi\cos(\phi_s) - \sin(\phi_s)\right]\right\} = H_{en}. \tag{3.33}$$

Calculating ΔW_d further with respect to $\Delta\phi$ using numerical methods, the different trajectories are obtained in longitudinal phase space, as shown in Figure 3.8.

Figure 3.8 has been obtained by assuming the constant velocity of the synchronous particle. By observing the longitudinal phase space in Figure 3.8, the reader can notice the stable trajectory, known as a *bucket*, marked by the green line, the unstable trajectory highlighted by the red line, and the trajectory that separates the stable and unstable ones, known as the *separatrix*, denoted by the blue line.

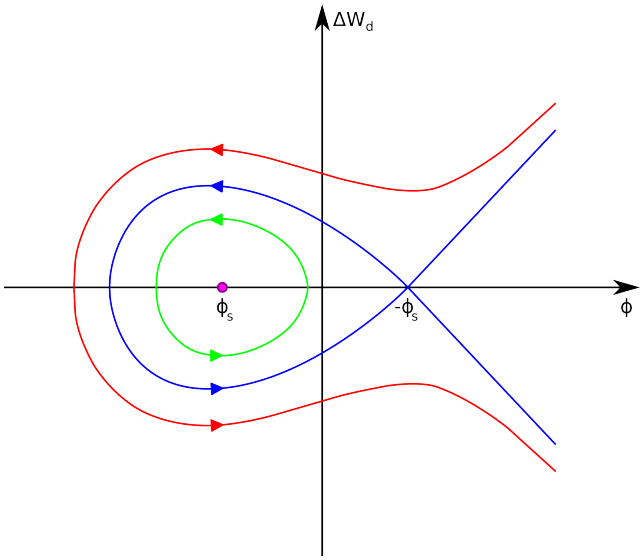


Figure 3.8: Longitudinal phase space with stable trajectory (green line) and unstable trajectory (red line) separated by the separatrix (blue line).

3.2.2 Transverse beam dynamics within linac structures

Inside the linac structure, not all particles are always located directly on the beam axis. Most of them are positioned slightly off-axis, which is not an issue until they reach a gap. All off-axis particles inside each gap, in addition to experiencing the longitudinal electric field (as explained in the previous subsection), also experience the radial components of both magnetic and electric fields. Since the crest of the accelerating field is not centered in the gap, the beam undergoes weaker radial field components at the beginning of the gap compared to the radial field components at the end of the gap. This inequality in accelerating field strength is known as the *defocusing effect*, which is undesirable. If this effect is not taken into consideration during the design process, beam loss is inevitable. In the case where the radial and longitudinal electric field components (i.e., E_r and E_z) near the beam axis are nonzero, the following equation is derived from Maxwell's equations [45]:

$$\frac{1}{r}\frac{\partial}{\partial r}\left(rE_r\right) + \frac{\partial E_z}{\partial z} = 0. \tag{3.34}$$

The solution of the Equation 3.34 is:

$$E_r = -\frac{r}{2}\frac{\partial E_z}{\partial z}. \tag{3.35}$$

Equation 3.35 implies the appearance of the radial focusing effect (negative E_r component) when the longitudinal field component is increasing, as is usually the case at the beginning of each gap. On the other hand, the same equation implies the appearance of the radial defocusing effect (positive E_r component) when the longitudinal field component is decreasing, as is typically the

case at the end of each gap. By taking into account the condition for longitudinal focusing, where the longitudinal field rises over time along the gap, the radial focusing effect at the beginning of the gap will be weaker than the radial defocusing effect at the end of the gap. To overcome the defocusing effects, additional magnetic lenses are usually needed, with magnetic quadrupoles being the most widely used [84–87].

The ideal quadrupole lenses produce a constant gradient for focusing or defocusing the beam with x (horizontal) and y (vertical) coordinates in the transverse plane, and this is defined as:

$$G = \frac{\partial B_y}{\partial x} = \frac{\partial B_x}{\partial y}. \tag{3.36}$$

Along the ideal quadrupole, the particle motion in the transverse plane is best characterized by the well-known second-order differential Hill's equations, expressed as:

$$\frac{d^2x}{ds^2} + \frac{|qG(s)|}{m_0 c\gamma_p \beta(s)} x = 0, \tag{3.37}$$

$$\frac{d^2y}{ds^2} - \frac{|qG(s)|}{m_0 c\gamma_p \beta(s)} y = 0. \tag{3.38}$$

The solution of Hill's equations can be written in the form of matrices, which are more useful for circular accelerators, or in a form similar to that of a harmonic oscillator, which is more useful for linac structures. The detailed derivation of the solution of Hill's equation in matrix form is shown in [45], while the other solution form, known as the *phase-amplitude form*, will be discussed in this subsection. The solution in phase-amplitude form is provided by *Floquet's theorem* [88]:

$$x(s) = \sqrt{\varepsilon_{xx'}\beta(s)}\cos(\phi(s) + \phi_0), \tag{3.39}$$

where $\varepsilon_{xx'}$ and ϕ_0 are constants defined by the initial condition, while $\phi(s)$ and $\beta(s)$ represent the phase and amplitude functions. For transverse beam analysis, especially important parameters are the amplitude function, known as the *beta function*, and the constant $\varepsilon_{xx'}$, known as the *beam emittance* in the horizontal phase space, since both are related to the beam's shape and size. Another important parameter is the so-called *phase advance*, denoted as the $\phi(s)$ function, which is related to the $\beta(s)$ function through the following expression:

$$\phi(s) = \int \frac{ds}{\beta(s)}. \tag{3.40}$$

Besides the $\beta(s)$ function, there are two additional functions that are useful in transverse beam analysis, namely the $\alpha(s)$ and $\gamma(s)$ functions, both of which depend on the beam abscissa s. The $\alpha(s)$, $\beta(s)$, and $\gamma(s)$ functions are collectively referred to as the *Courant-Snyder parameters* or simply the *Twiss parameters*. Parameters $\alpha(s)$ and $\gamma(s)$ are defined as [88]:

$$\alpha(s) = -\frac{1}{2}\frac{d\beta(s)}{ds}, \tag{3.41}$$

$$\gamma(s) = \frac{1+\alpha^2(s)}{\beta(s)}. \tag{3.42}$$

According to Equations 3.41 and 3.42, both the $\alpha(s)$ and $\gamma(s)$ parameters depend on the $\beta(s)$ function, while the $\beta(s)$ function represents a property of the linac structure. Besides the fact that both the $\beta(s)$ and $\gamma(s)$ functions are always positive, it is important to emphasize that neither of them has any similarity to the Lorentz factor (i.e., $\gamma_p = 1/\sqrt{1-\beta^2}$), the face angle of the DTL cell (i.e., γ - consult Figure 4.5), or the relativistic particle velocity (i.e., $\beta = v/c$), so they should not be confused with them.

Furthermore, considering Twiss parameters, the so-called *Courant-Snyder invariant* can be derived from Hill's equation, which, in the horizontal plane, is formulated as:

$$\gamma(s)x^2 + 2\alpha(s)xx' + \beta(s)x'^{\,2} = \varepsilon, \tag{3.43}$$

where x represents the position and x' is the angular deviation of the particle in the horizontal plane. Similarly to Equation 3.43, the Courant-Snyder invariant can also be derived for the same particle in both vertical and longitudinal planes. However, to avoid confusion, this subsection will focus only on the Courant-Snyder invariant for the horizontal plane. Since Equation 3.43 provides a physical interpretation of the Twiss parameters, it holds significant value in the field of transverse beam dynamics for linac structures.

Equation 3.43 represents the general equation of a tilted ellipse, where the angle of rotation (θ_e) depends on the Twiss parameters through the following relation:

$$\tan(2\theta_e) = \frac{4\alpha(s)}{\gamma(s) - \beta(s)}. \tag{3.44}$$

Observing Equation 3.44, it is noticeable that the ellipse is tilted when the $\alpha(s)$ parameter has a nonzero value, while it is tilted by 45° when the $\gamma(s)$ and $\beta(s)$ parameters are equal. On the other hand, Equation 3.43 implies that the center of the Twiss ellipse is at the origin of the phase space. It can be easily shown that the area of the ellipse, as expressed in Equation 3.43, is $A_{xx'} = \pi\varepsilon_{xx'}$. This is determined by calculating the semi-minor and semi-major axes using the eigenvalues of the diagonalized form of the ellipse and then multiplying them by π. This result implies that the area of the horizontal Twiss ellipse is proportional to the beam emittance in the horizontal plane ($\varepsilon_{xx'}$). The visual representation of the Twiss ellipse in the horizontal plane, with indicated characteristic points, is shown in Figure 3.9.

Any arrangement of transverse focusing quadrupoles that repeats along the linac structure is called a *lattice*. Within the linac structures, various focusing lattices can be found, such as $FODO$, $FOFO - DODO$, and FDO. By convention, each focusing lattice is denoted using one (or more) of the three letters: F, D, and O. The letter F indicates beam focusing in

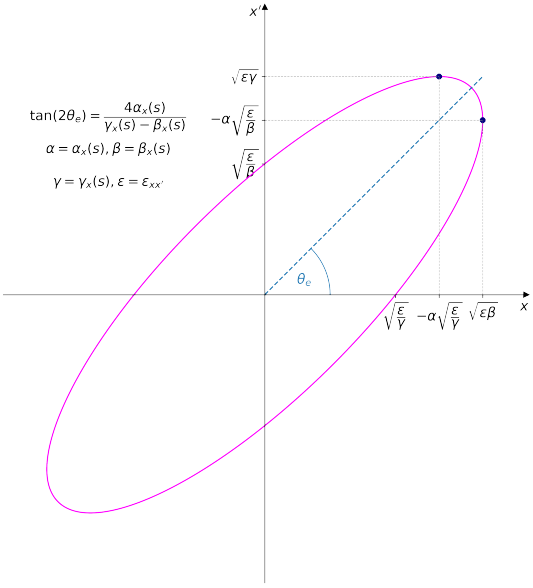


Figure 3.9: Twiss ellipse in horizontal phase space with characteristic points.

the horizontal plane and beam defocusing in the vertical plane, while the letter D denotes the opposite - beam defocusing in the horizontal plane and beam focusing in the vertical plane. The letter O represents a drift space, where the beam is neither focused nor defocused by quadrupoles.

The phase advance, defined by Equation 3.40, provides valuable information about the speed of particle motion in phase space. For example, in an $FODO$ lattice with a phase advance of 90 degrees per cell, each particle in the beam completes a full 360-degree rotation in phase space after passing through four cells.

In addition to phase advance, another significant parameter must be introduced: the amplitude of Equation 3.39, given by $\sqrt{\varepsilon_{xx'}\beta(s)}$, which is known as the *beam envelope*. The beam envelope describes the spread and/or divergence of the beam in phase space.

Figure 3.10 illustrates the beam envelope for both the horizontal plane (teal) and the vertical plane (orange), along with the Twiss ellipses at the center of each element in an $FODO$ lattice with a phase advance of 90 degrees per cell.

One of the common mathematical methods used to describe the transportation of the Twiss ellipse between two locations is the *matrix formalism*. If the matrices **X** and **R** are defined as:

$$\mathbf{X} = \begin{bmatrix} x \\ x' \end{bmatrix}, \tag{3.45a}$$

$$\mathbf{R} = \begin{bmatrix} \gamma(s) & \alpha(s) \\ \alpha(s) & \beta(s) \end{bmatrix}, \tag{3.45b}$$

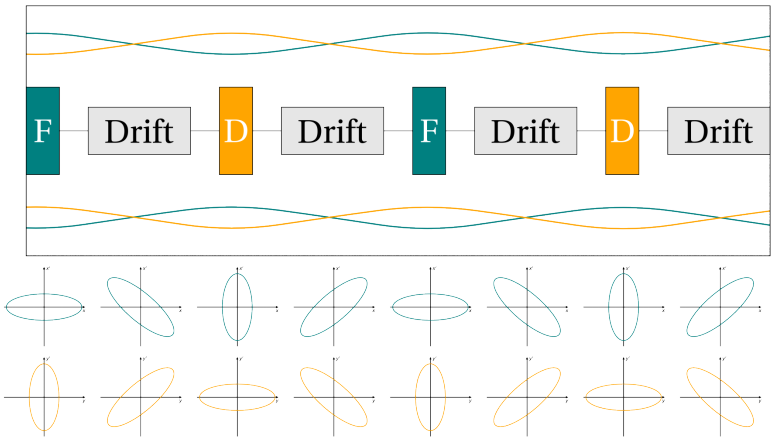


Figure 3.10: Beam envelope in the horizontal plane (teal) and vertical plane (orange), along with Twiss ellipses plotted at the center of each element in the $FODO$ lattice. The phase advance per cell is 90 degrees.

then the Courant-Snyder invariant (Equation 3.43) can be expressed in matrix form as:

$$\mathbf{X}^T\mathbf{R}^{-1}\mathbf{X} = \varepsilon, \tag{3.46}$$

where $\mathbf{X}^T$=$[x\ x']$ is the transpose matrix, and $\mathbf{R}^{-1}$ is the inverse matrix:

$$\mathbf{R}^{-1} = \begin{bmatrix} \beta(s) & -\alpha(s) \\ -\alpha(s) & \gamma(s) \end{bmatrix}. \tag{3.47}$$

Any particle movement from one position to another can be written in matrix form as $\mathbf{X}_2 = \mathbf{M}\mathbf{X}_1$, where $\mathbf{M}$ is known as the transfer matrix, with the general form given as:

$$\mathbf{M} = \begin{bmatrix} M_{11} & M_{12} \\ M_{21} & M_{22} \end{bmatrix}. \tag{3.48}$$

The transfer matrix represents an important parameter that depends on the lattice element and the type of focusing magnets. It can have one of three forms, depending on the lattice element [81]:

1. *Focusing quadrupole*

$$\mathbf{M} = \begin{bmatrix} \cos\left(\sqrt{K}l_q\right) & \left(\sqrt{K}\right)^{-1}\sin\left(\sqrt{K}l_q\right) \\ -\sqrt{K}\sin\left(\sqrt{K}l_q\right) & \cos\left(\sqrt{K}l_q\right) \end{bmatrix}, \tag{3.49}$$

2. *Defocusing quadrupole*

$$\mathbf{M} = \begin{bmatrix} \cosh\left(\sqrt{K}l_q\right) & \left(\sqrt{K}\right)^{-1}\sinh\left(\sqrt{K}l_q\right) \\ \sqrt{K}\sinh\left(\sqrt{K}l_q\right) & \cosh\left(\sqrt{K}l_q\right) \end{bmatrix}, \tag{3.50}$$

3. *Drifting space*

$$\mathbf{M} = \begin{bmatrix} 1 & l_d \\ 0 & 1 \end{bmatrix}, \tag{3.51}$$

where l_q is the quadrupole length, l_d is the drifting space, and K is a variable defined as:

$$K = \frac{|qG|}{mc\beta(s)\gamma(s)}. \tag{3.52}$$

Combining the expression for calculating the next position of a beam particle according to its current placement in phase space ($\mathbf{X}_2 = \mathbf{M}\mathbf{X}_1$) with the matrix formalism of the Twiss ellipse (Equation 3.46) both in the current and next positions ($\mathbf{X}_1^T\mathbf{R}_1^{-1}\mathbf{X}_1 = \varepsilon$ and $\mathbf{X}_2^T\mathbf{R}_2^{-1}\mathbf{X}_2 = \varepsilon$), the following relation is obtained:

$$\mathbf{R}_2 = \mathbf{M}\mathbf{R}_1\mathbf{M}^T. \tag{3.53}$$

Rearranging Equation 3.53, the Twiss parameters of the next position ($\alpha_2(s)$, $\beta_2(s)$, $\gamma_2(s)$) can be calculated based on the matrix elements of the upcoming lattice component (M_{ij}) and the values of the current Twiss parameters ($\alpha_1(s)$, $\beta_1(s)$, $\gamma_1(s)$):

$$\begin{bmatrix} \alpha_2(s) \\ \beta_2(s) \\ \gamma_2(s) \end{bmatrix} = \begin{bmatrix} 1 + 2M_{12}M_{21} & -M_{11}M_{21} & -M_{12}M_{22} \\ -2M_{11}M_{12} & M_{11}^2 & M_{12}^2 \\ -2M_{21}M_{22} & M_{21}^2 & M_{22}^2 \end{bmatrix} \begin{bmatrix} \alpha_1(s) \\ \beta_1(s) \\ \gamma_1(s) \end{bmatrix}. \tag{3.54}$$

3.2.3 Beam distributions

Earlier, it was shown that the area inside the Twiss ellipse is defined by the beam emittance ($A_{xx'} = \pi\varepsilon_{xx'}$). The unit typically used for transverse emittance is $\pi.mm.mrad$, while the unit used for longitudinal beam emittance is $\pi.deg.MeV$. The accelerated beam is constrained by *Liouville's theorem*, which applies the conservation law to the beam. In other words, according to Liouville's theorem, the beam can change its shape in phase space, but its size always remains the same-beam emittance is constant ($\varepsilon_{xx'}$ = const.).

On the contrary, a significant influence on the design process of linac structures when low-velocity particles are accelerated has the phenomenon known as *space charge*. Space charge represents repulsive electric Coulomb forces between particles within a beam. At low energies, the attractive magnetic forces are much weaker than the Coulomb repulsive forces among the particles, so Hill's equation (Equation 3.37) should be modified to take into consideration repulsive electric forces:

$$\frac{d^2x}{ds^2} + \frac{|qG(s)|}{m_0 c\gamma_p \beta(s)} x - F_{cx}(x, y, z, s) = 0, \tag{3.55}$$

where F_{cx} represents the horizontal component of Coulomb's repulsive electric force, and it is defined as:

$$F_{cx} = \frac{qE_{cx}(x, y, z, s)}{\beta^2 \gamma_p^3 mc^2}. \tag{3.56}$$

In Equation 3.56, E_{cx} represents the horizontal component of the electric field generated by the particles. By taking into account Coulomb's repulsive force, the multi-particle simulation problem is considered. In contrast to the single-particle simulation, the simulation of multiple particles requires the definition of a reasonable beam distribution in order to reproduce a realistic linac structure. Taking into account a statistical beam distribution, it is more reasonable to define the statistical measurement of emittance rather than the actual 100% emittance. In most cases, the Root Mean Square (RMS) emittance is considered as a statistical measurement, which allows for the calculation of the particle fraction inside the area of interest [89]. The unnormalized rms beam emittance is defined as:

$$\varepsilon_{rms} = \sqrt{\langle x_i^2 \rangle \langle x_i'^{\,2} \rangle - \langle x_i x_i' \rangle^2}, \tag{3.57}$$

where $\langle x_i^2 \rangle$, $\langle x_i'^{\,2} \rangle$ and $\langle x_i x_i' \rangle$ represent the beam particles' average oscillation amplitudes and their derivatives, whose detailed derivation can be found in [79], while their final form is as follows:

$$\langle x_i^2 \rangle = \varepsilon_{xx'} \cdot \beta(s), \tag{3.58a}$$

$$\langle x_i'^{\,2} \rangle = \varepsilon_{xx'} \cdot \gamma(s), \tag{3.58b}$$

$$\langle x_i x_i' \rangle = -\varepsilon_{xx'} \cdot \alpha(s). \tag{3.58c}$$

Using Equation 3.57, the beam emittance can be calculated for any arbitrary particle distribution, which is specifically important when protons or particles heavier than protons are accelerated in linac structures [79].

Unfortunately, the particle divergence depends on both transverse and longitudinal momenta, so variations in these quantities can increase or decrease the unnormalized rms emittance according to Equation 3.57. Throughout the acceleration, the transverse momentum is constant, while the longitudinal momentum increases. The disproportional change of transverse and longitudinal momenta during acceleration leads to a reduction in divergence. In order to compensate for the aforementioned change, the normalized rms emittance is introduced, which transforms angle coordinates into the transverse momentum coordinates:

$$\varepsilon_{n,rms} = \beta\gamma_p \varepsilon_{rms}. \tag{3.59}$$

In the case of low-velocity ion acceleration within linac structures, the normalized rms emittance growth ($\varepsilon^{gr}_{n,rms}$) is a useful parameter, since it provides an overall indication of the undesirable effects impacting the beam, such as beam mismatching due to space charge effects [90], and it is calculated as:

$$\varepsilon^{gr}_{n,rms}[\%] = \frac{\varepsilon^{out}_{n,rms} - \varepsilon^{in}_{n,rms}}{\varepsilon^{in}_{n,rms}} 100\%, \tag{3.60}$$

where $\varepsilon^{in}_{n,rms}$ is the normalized rms emittance at the entrance of the linac structure, and $\varepsilon^{out}_{n,rms}$ is the normalized rms emittance at the exit of the linac structure.

During the design process of linac structures, either 4D or 6D beam distribution is considered. A 4D beam distribution provides information about the beam only in the transverse planes, so it is commonly used in applications where the effects of longitudinal motion can be negligible, such as Low Energy Beam Transport (LEBT) before RFQ [91, 92]. On the other hand, a 6D beam distribution provides more details about the beam, since it includes additional information about the beam in the longitudinal plane, besides the transverse planes. Therefore, 6D beam distributions are more commonly used in multi-particle beam simulations when linac structures are designed.

One of the most popular 4D beam distributions is the *KV distribution*, discovered by Kapchinsky and Vladimirsky. The KV beam distribution does not provide a realistic beam description, but it holds an important place in theoretical studies [93]. The 6D beam representation is of special importance when the space charge effect cannot be neglected, which is the case in low-energy beam acceleration with linac structures. A good representation of a low-energy beam, with the presence of a strong Coulomb repulsive force, is the *6D-Uniform distribution*, which provides uniform beam filling inside the Twiss ellipse. A larger beam density in the center of the Twiss ellipse, but more spread outside, is provided by the *6D-Parabolic distribution*. The beam distribution similar to the 6D-Parabolic distribution is the *6D-Gaussian distribution*, which has a Gaussian profile with an even bigger spread than the parabolic distribution but a more centralized beam within the ellipse. The visual representation of the 2D projection in the horizontal phase space of each mentioned distribution is shown in Figure 3.11.

For clarity, each beam projection shown in Figure 3.11, along with all upcoming beam projections throughout this thesis, uses brighter (yellow/red) tones for higher beam density, while darker (blue/green) tones are reserved for areas with lower beam density.

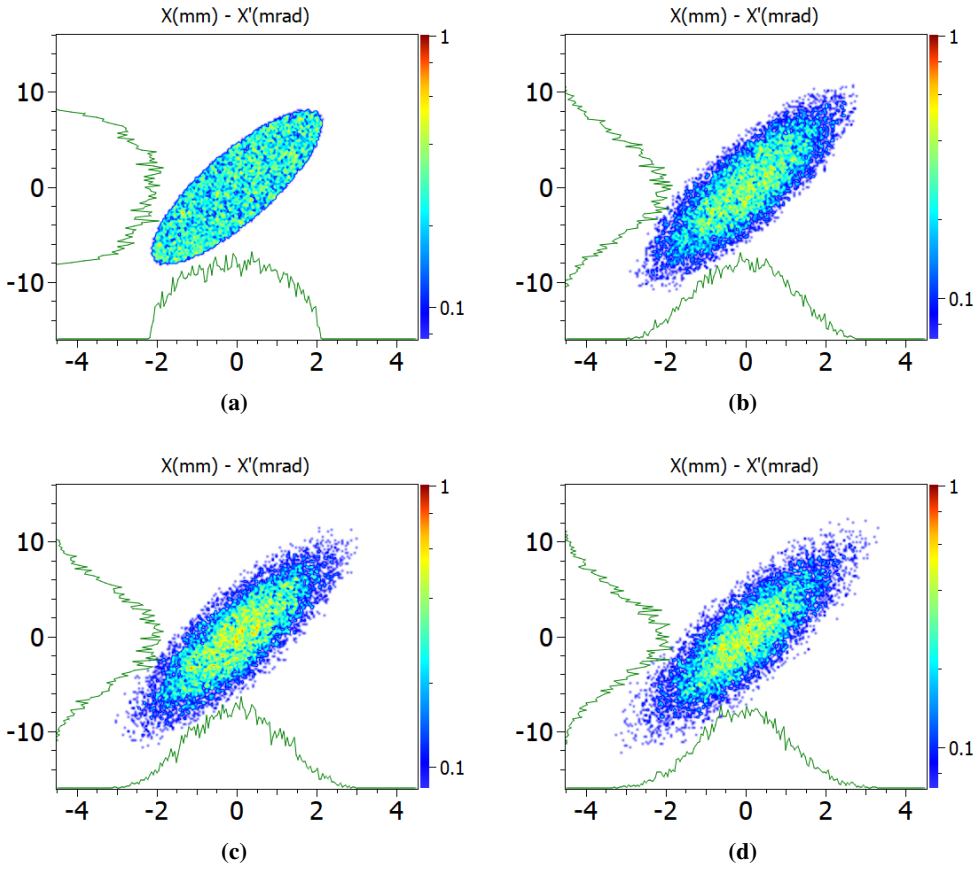


Figure 3.11: Beam distribution in horizontal phase space with: (a) 4D-KV distribution; (b) 6D-Uniform distribution; (c) 6D-Parabolic distribution; (d) 6D-Gaussian distribution. All of the beam distributions have the same rms emittances.

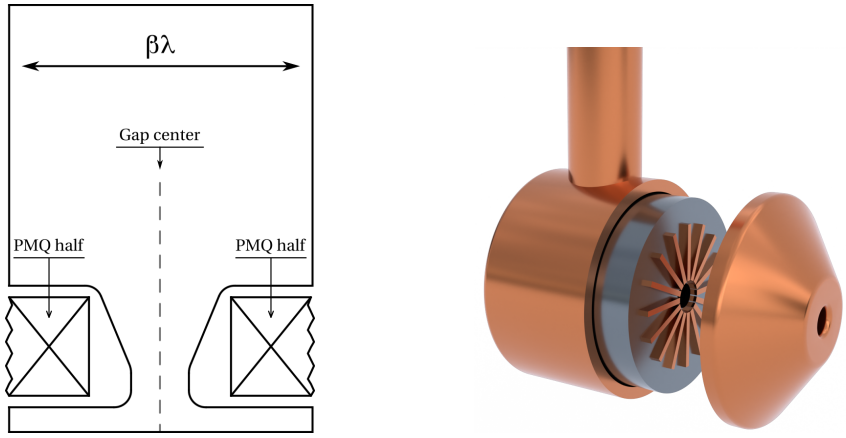
3.3 Analyzed structures for acceleration and beam manipulation

The following subsections provide a comprehensive overview of the electromagnetic and beam dynamics theories that govern both Alvarez-type and H-mode linac structures. Additionally, the RF structures used for beam manipulation, such as the Debunching Cavity (DEB) and Energy Ramping Cavity (ERC), are also elaborated, which play a pivotal role in shaping and modifying the energy and phase of the beam.

3.3.1 Alvarez drift tube linac

As a proton linac structure, the DTL has proven to be an accelerating unit with high power efficiency up to energies of around 60 MeV, beyond which it is typically replaced by more

power-efficient structures, such as the CCDTL [2]. The DTL operates in the 0-mode; therefore, to maintain synchronicity, each cell must comply with Equation 3.23a, while β increases with each cell. In modern DTL structures, transverse beam focusing is provided by Permanent Magnet Quadrupoles (PMQ) placed inside every Drift Tube (DT). A section of a single DTL cell is shown in Figure 3.12a, while a single DT is presented in Figure 3.12b.



(a) **(b)**

Figure 3.12: (a) The section of one cell of DTL; (b) A drift tube with PMQ within DTL.

Since each DT contains a PMQ, the space within it must be sufficient to accommodate the PMQ and cooling channels. Additionally, the gap distance between two consecutive drift tubes must be carefully chosen to achieve the highest efficiency by maximizing ZT^2, which ensures the highest fraction of RF power transferred to the beam. The 3D model of the DTL is shown in Figure 3.13.

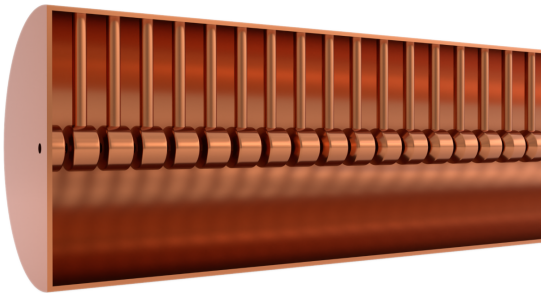


Figure 3.13: The 3D model of DTL.

The DTL resonates in TM_{010} electromagnetic mode, which is characterized by a longitudinal electric field and an azimuthal magnetic field, as shown in Figures 3.1 and 3.3a. Regarding transverse beam focusing, DTL structures typically use either FODO or FOFODODO lattices, where F represents a PMQ that focuses the beam in the horizontal direction and defocuses it in

the vertical direction, D indicates a PMQ that defocuses the beam in the horizontal direction and focuses it in the vertical direction, and O denotes the drift space between two PMQs located within neighboring drift tubes where the beam is neither focused nor defocused in both the horizontal and vertical planes.

There are numerous DTL structures currently in operation worldwide, including well-known examples such as LINAC2 and LINAC4 at CERN, the ISIS linac at Rutherford Appleton Laboratory (RAL), the linac at the European Spallation Source (ESS), the SNS linac at Oak Ridge National Laboratory (ORNL), and many others.

3.3.2 Quasi-Alvarez drift tube linac

At low particle velocities, the cell length in the DTL becomes very short, resulting in a correspondingly short drift tube that does not provide sufficient space for a quadrupole magnet. To overcome this limitation, the QA-DTL was proposed by D.J. Warner in the 1990s [94], which allows for longer drift tubes to accommodate a quadrupole. The main modification compared with the DTL is a reduction in the number and an increase in the length of drift tubes that accommodate PMQs for transverse beam focusing. Due to the lack of PMQs within each DT, the concept of a *cell* (the distance between the halves of neighboring DTs) is no longer of primary interest. Instead, the *super-period* (the distance between the halves of DTs containing the PMQ) becomes the key consideration during the design process. This approach significantly increases the complexity of the design, as DTs of different sizes need to be optimized for the highest effective shunt impedance per unit length, rather than one, as is the case with the DTL. Similarly to the DTL, the QA-DTL also uses PMQs for transverse beam focusing (consult Figure 3.12b). The magnet arrangement within the QA-DTL is FO...ODO..O.

As with the DTL, the QA-DTL is also a 0-mode structure. Therefore, the distance between the centers of two consecutive gaps around the DTs that do not contain the PMQ is $\beta\lambda$ (according to Equation 3.23a). On the other hand, the distance between the centers of two consecutive gaps around the DTs that contain the PMQ is $2\beta\lambda$. Taking these two factors into consideration, the length of one super-period becomes $(n_p+2)\beta\lambda$, where n_p is the *periodicity factor* and represents the number of DTs without PMQs within one super-period ($n_p \in \mathbb{N}$ and $n_p \geq 1$). Figure 3.14 shows some QA-DTL configurations compared with the DTL.

The periodicity factor n_p is a very important parameter that directly affects the efficiency of the linac structure, so it needs to be chosen carefully. From the beam dynamics point of view, the periodicity factor is selected as a trade-off between the PMQ gradient strength and beam transmission. The QA-DTL reaches its highest efficiency when the periodicity factor is two ($n_p = 2$) [15, 16]. In this case, the super-period consists of two drift tubes without PMQs and two halves of drift tubes containing PMQs, as shown in Figure 3.15.

The QA-DTL reaches its highest efficiency when the periodicity factor is two ($n_p = 2$) [15, 16], in which case the super-period consists of two drift tubes without PMQs and two halves of DTs containing PMQs as shown in Figure 3.15.

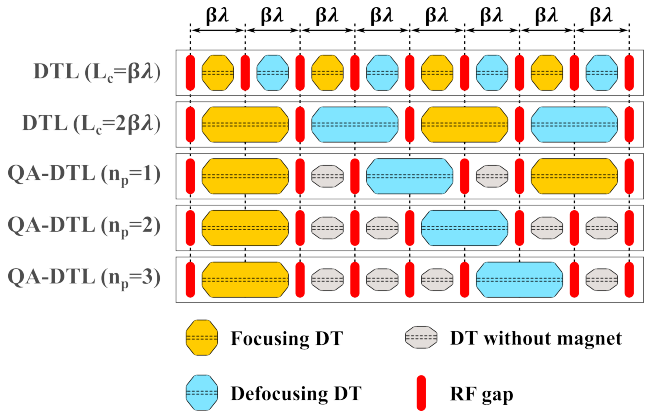


Figure 3.14: Comparison between different QA-DTL configurations and DTL (adapted from [15]).

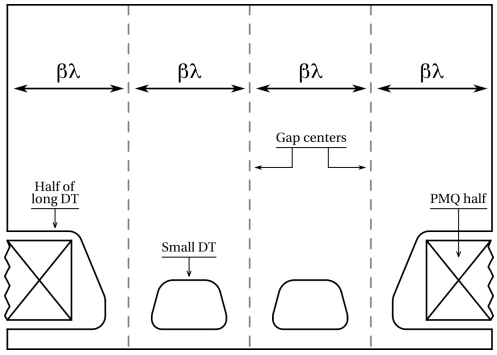


Figure 3.15: One super-period of QA-DTL with periodicity factor of two.

The 3D model of the QA-DTL segment, featuring super-periods with a periodicity factor of two, is shown in Figure 3.16.

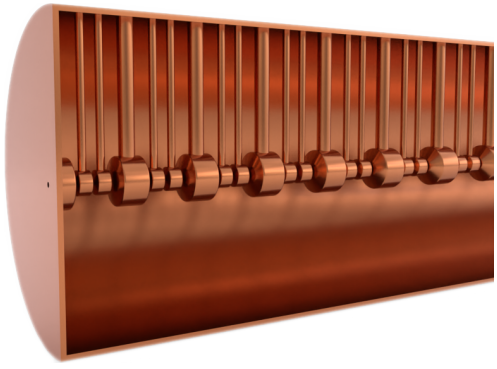
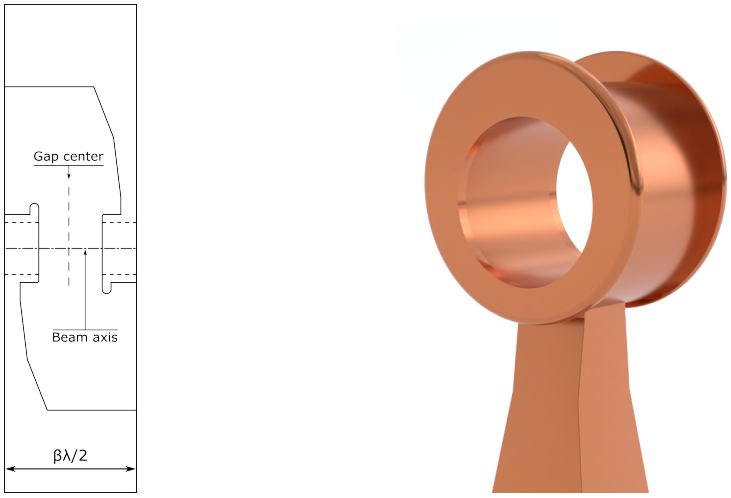


Figure 3.16: The 3D model of QA-DTL featuring super-periods with the periodicity factor of two.

Similarly to the DTL, the QA-DTL also resonates in the TM_{010} electromagnetic mode, which is characterized by a longitudinal electric field and an azimuthal magnetic field, as shown in Figures 3.1 and 3.3a.

3.3.3 H-mode linac structures

The most widely used H-mode linac structure for the acceleration of particles heavier than protons is the IH-DTL. A variation of the IH-DTL that was proposed, but never built, is the S-IH-DTL. Both linac structures are π-mode structures, with the length of each cell defined by Equation 3.23c. According to Equations 3.23a and 3.23c, for a given energy, the cell of a π-mode structure (IH-DTL and S-IH-DTL) is two times shorter than the cell of a 0-mode structure (DTL and QA-DTL). Both IH-DTL and S-IH-DTL resonate in the TE_{110} electromagnetic mode, which is characterized by a longitudinal magnetic field and an azimuthal electric field, as shown in Figures 3.1 and 3.3b. One cell of an H-mode linac structure is shown in Figure 3.17a, while one DT of the same structure is presented in Figure 3.17b.



(a) **(b)**

Figure 3.17: (a) The section of one cell of H-mode cavity; (b) A drift tube within H-mode drift tube linac.

The transverse focusing and defocusing in IH-DTL are achieved using quadrupole doublets, triplets, or solenoid lenses [95], which are placed after a certain number of cells, as shown in Figure 3.18.

Due to the inconsistent presence of quadrupoles within IH-DTL, the beam shape is affected, and undesirable effects may occur. Therefore, the beam dynamics of IH-DTL, known as the *combined zero degree structure* (KONUS) beam dynamics, presents a challenge during the design process. In KONUS dynamics, there is no longitudinally stable particle (synchronous phase is zero), and the process is highly non-linear, leading to complex beam distributions in

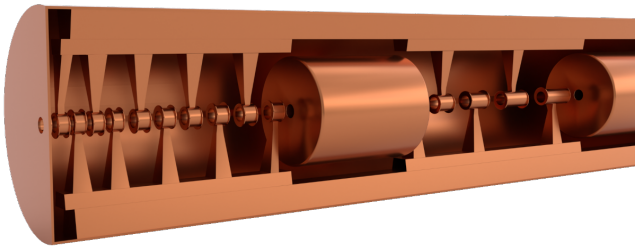


Figure 3.18: The 3D model of IH-DTL.

the longitudinal plane and consequent beam loss. The main difference between IH-DTL and S-IH-DTL is the placement of quadrupoles - in the case of S-IH-DTL, the quadrupoles are located outside the accelerating structure, with two neighboring cavities surrounding it, as shown in Figure 3.19.

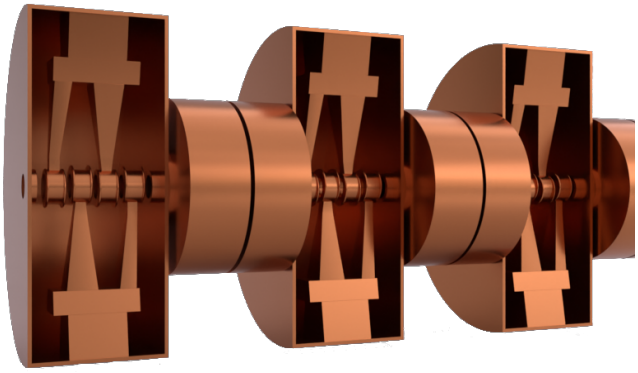


Figure 3.19: The 3D model of S-IH-DTL.

Each cavity of the S-IH-DTL is physically separated, allowing adjustment of geometric parameters such as the cavity radius, thereby enabling the S-IH-DTL to resonate at higher frequencies than the IH-DTL.

3.3.4 Other RF structures for beam manipulation within linacs

For more efficient beam injection into a synchrotron, an additional RF structure known as a *debunching cavity* (DEB) is required. The primary goal of the DEB is to reduce energy spread as much as possible, which contributes to a longer phase spread in longitudinal phase space. Depending on the application, the DEB can consist of one or more cells, making it much shorter and simpler to design than accelerating structures.

The position of the DEB, situated between the linac section and the therapy synchrotron, is crucial and must be carefully calculated. To effectively reduce energy spread, sufficient drifting space must be provided between the last accelerating cell and the DEB. Ideally, the drifting space should be long enough for the phase spread to reach $\pm 45^{\circ}$ in the longitudinal phase space. If the

phase spread exceeds $\pm 45°$, part of the bunch will be out of the linear region of the sinusoidal voltage, and filamentation will occur, leading to beam loss. It should be noted that the available space is usually limited, posing additional challenges in the design of the DEB.

Through the drift space, the beam expands in the longitudinal phase space, resulting in an elongated and narrower Twiss ellipse. During DEB operation, the EM field within the structure is excited in such a way that the zero-crossing phase from Figure 3.7 is positioned at the center of the cell gap. The interaction between the EM field (and thus the voltage) and the beam results in beam rotation in the longitudinal phase space, as illustrated in Figure 3.20.

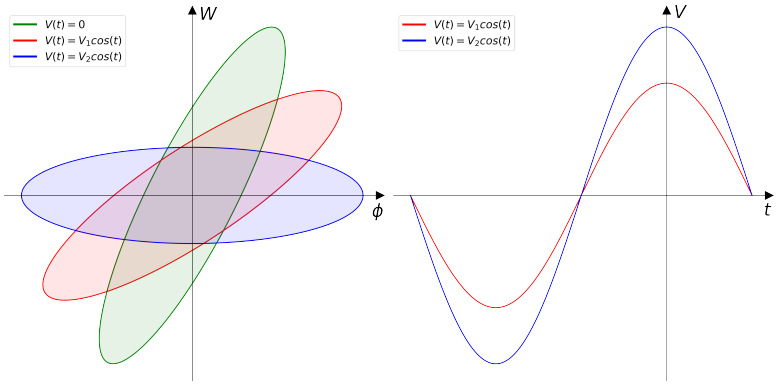


Figure 3.20: (Left) Twiss ellipses within the DEB in the presence of voltage with different amplitudes; (Right) the voltage with different amplitudes corresponding to the ellipses on the left. The green Twiss ellipse occurs when the DEB is not in operation.

The angle of beam rotation depends on the EM field amplitude, which directly corresponds to the voltage applied to the cavity. A stronger voltage amplitude will lead to a stronger beam rotation in longitudinal phase space. The main goal of the DEB is to rotate the beam in longitudinal phase space until it is horizontally positioned, minimizing the energy spread. As the energy spread is reduced, the phase spread increases. The increase in beam phase spread is not a problem, as the beam will be rebunched within the synchrotron. However, the maximum voltage within the DEB cell is limited by the Kilpatrick criterion (Equation 3.19). The voltage limitation results in an increase in the number of DEB cells, which in turn requires additional space within the linac configuration.

On the other hand, the Energy Ramping Cavity (ERC) is optional and can be used for a more advanced technique of beam injection into the synchrotron, known as *longitudinal beam painting*. The goal of the ERC is to slightly ramp the energy of each beam bunch. Ramping the beam energy results in the injection of the beam into the synchrotron at different positions relative to the longitudinal phase space, thereby increasing injection efficiency. To achieve this energy displacement, the EM field is excited in such a way that its phase constantly oscillates between $\varphi_0 - \Delta\varphi$ and $\varphi_0 + \Delta\varphi$, ensuring that each successive beam bunch experiences the desired phase, as illustrated in Figure 3.21.

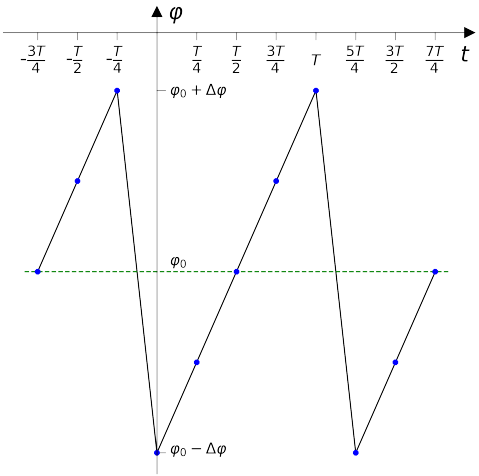


Figure 3.21: Phase oscillation within the ERC; φ_0 corresponds to the zero-crossing phase. The blue points represent the phase of each beam bunch at the center of the gap.

For better visualization, the beam bunches with extreme energy displacements (those with the highest and lowest energy values), along with the beam bunch that remains unaffected by the ERC, are shown in Figure 3.22.

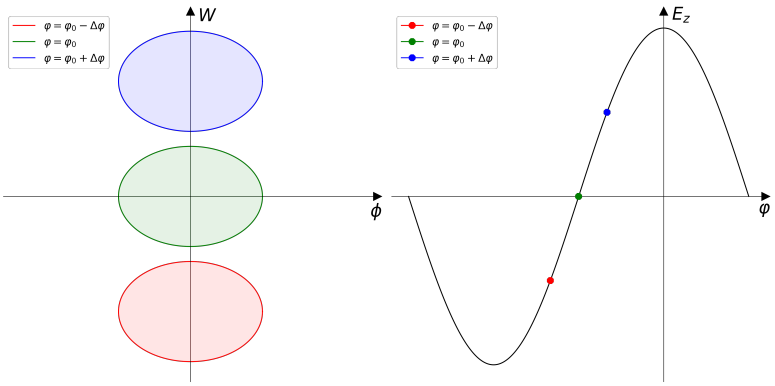
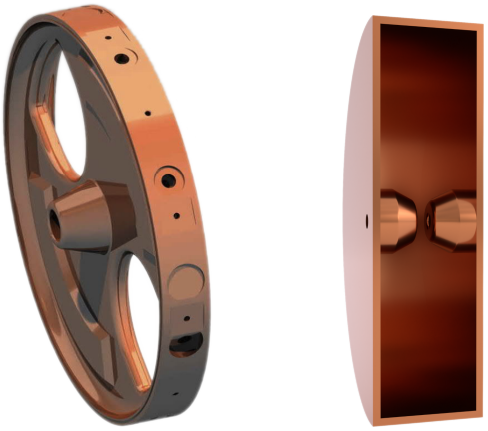


Figure 3.22: (Left) Twiss ellipse within the ERC in the presence of an external EM field with different phases in the middle of the gap; (Right) the external EM field corresponding to the ellipses on the left.

Both DEB and ERC share a similar geometry, with slight differences in gap size and/or cell length. Different types of single-cell DEB and ERC are shown in Figure 3.23.



(a) **(b)**

Figure 3.23: (a) π-mode structure (Source: [2]) and (b) 0-mode structure used as DEB or ERC units.

3.4 Cost efficiency of Alvarez-type linac structures

One of the key factors influencing the selection of an accelerating structure is the cost of the RF system and the cost of the accelerating structure, collectively referred to as the total cost. Accordingly, a calculation and comparison of the total costs of conventional DTL and QA-DTL structures for low-velocity ion acceleration applications (up to 5 MeV/u) has been conducted. But before stepping into linac economics, a few important variables need to be defined first:

- C_p is the capital cost of the radio-frequency system, measured in €/W;
- C_l is the capital cost of the accelerating structure, measured in €/m;
- l is the length of the cavity;
- P_b is the beam power (power delivered to the beam);
- P_d is the power dissipation in the cavity;

Now the total cost of the linac structure (C_{tot}) can be expressed as follows [45]:

$$C_{tot} = lC_l + (P_d + P_b)C_p \simeq lC_l + P_dC_p. \tag{3.61}$$

Since the beam power is small compared to the power dissipation, and it is independent of the choice of the accelerating structure, from now on the beam power will be neglected in all the calculations, as it has been done in Equation 3.61. Furthermore, rearranging Equations 3.8, 3.14 and 3.18, and then substituting them into Equation 3.61, the following is obtained:

$$l = \frac{\Delta W}{q(E_0T)\cos(\phi)} \simeq \frac{\Delta W}{q(E_0T)}, \tag{3.62}$$

$$P_d = \frac{(E_0T)^2}{ZT^2} l = \frac{(E_0T)^2}{ZT^2} \frac{\Delta W}{q(E_0T)} = \frac{(E_0T)\Delta W}{ZT^2 q}, \tag{3.63}$$

$$C_{tot} = \frac{\Delta W}{q} \frac{C_l}{(E_0T)} + \frac{\Delta W}{q} \frac{(E_0T)C_p}{ZT^2},$$

$$C_{tot} = \frac{\Delta W}{q} \left(\frac{C_l}{(E_0T)} + \frac{(E_0T)C_p}{ZT^2} \right). \tag{3.64}$$

All the calculations were performed with the assumption that the value of $\cos(\phi)$ is equal to one regardless of the selected accelerating structure. Observing Equation 3.64 it can be noticed that it depends on E_0T. Now, if this equation is differentiated with respect to E_0T and then set equal to zero, the condition of minimum cost is achieved:

$$\frac{\partial C_{tot}}{\partial E_0T} = \frac{\Delta W}{q} \left(-\frac{C_l}{(E_0T)^2} + \frac{C_p}{ZT^2} \right),$$

$$\frac{\partial C_{tot}}{\partial E_0T} = 0 \Rightarrow \frac{\Delta W}{q} \left(-\frac{C_l}{(E_0T)^2} + \frac{C_p}{ZT^2} \right) = 0,$$

$$\frac{C_l}{(E_0T)^2} = \frac{C_p}{ZT^2}, \tag{3.65}$$

$$C_p = \frac{ZT^2}{(E_0T)^2} C_l. \tag{3.66}$$

According to Equation 3.64, there is only one value of accelerating field (E_0T) at which the total cost of the structure is minimal, as shown in Figure 3.24.

In other words, the total cost is minimal when the cost of the accelerating structure (length cost - first term in Equation 3.64) is equal to the cost of the RF system (power cost - second term in Equation 3.64), which is exactly what Equation 3.65 is showing. Furthermore, substituting Equation 3.66 into Equation 3.61, the total cost can be related to the cavity cost per unit length (C_l):

$$C_{tot} = lC_l + P_d \frac{ZT^2}{(E_0T)^2} C_l = \left(l + \frac{P_d ZT^2}{(E_0T)^2} \right) C_l,$$

$$C_{tot} = \left(l + \frac{P_d ZT^2}{(\frac{\Delta W}{ql})^2} \right) C_l. \tag{3.67}$$

The capital cost of the accelerating structure can be further expanded as follows:

- cost for producing the cavity (tank) - C_{tank};
- cost for producing all drift tubes - C_{dt};
- cost for producing all permanent magnet quadrupoles - C_{pmq};

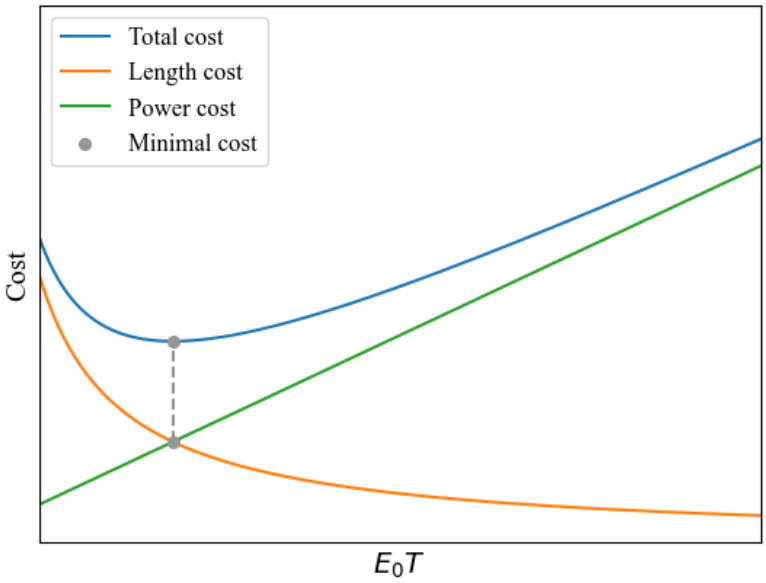


Figure 3.24: Total cost of the structure as a function of the accelerating field, with the emphasis on the minimal cost.

In other words, the capital cost of the accelerating structure can be written as:

$$C_l = \frac{C_{tank} + C_{dt} + C_{pmq}}{l} = C'_{tank} + \frac{C_{dt} + C_{pmq}}{l}, \tag{3.68}$$

where C'_{tank} represents the cost for producing 1 m of cavity. Depending on the linac structure, Equation 3.68 can be further expanded. In the case of the conventional DTL, each drift tube has the same geometry. Therefore, their price can be estimated as $N_{cell}C'_{dt}$, where N_{cell} is the number of cells and C'_{dt} is the cost for producing one drift tube. Similarly to drift tubes, the cost of producing the permanent magnet quadrupoles can be approximated as $N_{cell}C'_{pmq}$, where C'_{pmq} represents the cost for producing one permanent magnet quadrupole.

Papers [15, 96] have provided cost estimates for producing the components within proton DTL and carbon QA-DTL cavities. The absolute costs are irrelevant for this case, but the cost estimate can be used to calculate the ratio between the cost of the tank, the cost of the drift tubes, and the cost of the permanent magnet:

$$C'_{tank} \simeq 5.1 C'_{dt}, \tag{3.69}$$

$$C'_{pmq} \simeq 0.2 C'_{dt}. \tag{3.70}$$

The ratio of costs provided by Equations 3.69 and 3.70 is coherent with the costs of Linac4, the linear accelerator currently operating at CERN [2].

Furthermore, substituting Equations 3.69 and 3.70 into Equation 3.68, and taking into account all mentioned estimations, the capital cost of the conventional DTL is obtained:

$$\begin{aligned} C_l^{DTL} &= C'_{tank} + \frac{N_{cell}C'_{dt} + N_{cell}C'_{pmq}}{l}, \\ C_l^{DTL} &= 5.1C'_{dt} + \frac{N_{cell}C'_{dt} + 0.2N_{cell}C'_{dt}}{l}, \\ C_l^{DTL} &= \frac{(5.1l + 1.2N_{cell})}{l}C'_{dt}. \end{aligned} \tag{3.71}$$

In the case of QA-DTL, an additional parameter needs to be defined - the periodicity factor (n_p), which throughout this manuscript is set to two. Additionally, since the QA-DTL contains two drift tubes of different sizes, the cost of producing these drift tubes is divided into:

- cost of producing the bigger drift tubes, which are the same as those present in the conventional DTL, hence their production cost is C'_{dt}, and
- cost of producing the smaller drift tubes, which are two times smaller compared to the bigger drift tubes, and their production cost is estimated to be two times lower ($0.5C'_{dt}$).

One of the reasons for the cost difference between smaller and bigger drift tubes is the fabrication, which does not require expensive and complicated electromagnetic beam welding in the case of smaller drift tubes due to the absence of the quadrupole magnet. The other reason is the alignment system, which, in the case of smaller drift tubes, does not need to be as precise as that for bigger drift tubes, again due to the absence of the quadrupole magnets (alignment tolerances are defined by the quadrupole magnets).

Regarding permanent magnet quadrupoles, they are only present within the bigger drift tubes, resulting in a reduced number in comparison to the conventional DTL. In other words, the capital cost of the QA-DTL is as follows:

$$\begin{aligned} C_l^{QA} &= 5.1C'_{dt} + \frac{N_{cell}}{3l}C'_{dt} + \frac{2N_{cell}}{3l}\frac{C'_{dt}}{2} + \frac{N_{cell}}{3l}2(0.2C'_{dt}), \\ C_l^{QA} &= \left[5.1 + \left(\frac{1}{3} + \frac{1}{3} + \frac{2 \cdot 0.2}{3}\right)\frac{N_{cell}}{l}\right]C'_{dt}, \\ C_l^{QA} &= \left[5.1 + \frac{2.4}{3l}N_{cell}\right]C'_{dt} \simeq \frac{(5.1l + 0.8N_{cell})}{l}C'_{dt}. \end{aligned} \tag{3.72}$$

To ensure an accurate estimation of the cost ratio between the QA-DTL and the DTL, both designs have the same beam parameters. Additionally, the QA-DTL design has been slightly adjusted so that the input and output energies match those of the DTL from [1]. All necessary data from both studies have been summarized in Table 3.1.

Table 3.1: List of data regarding conventional DTL and QA-DTL

	DTL	**QA-DTL**	**Units**
l	6.4	4.65	m
P_d	1077.3	570	kW
ZT^2	31.5	67.7	MΩ/m
ΔW	48	48	MeV
q	4	4	-
N_{cell}	104	57	-

It can already be seen from Table 3.1 that the QA-DTL is 27% shorter and requires 47% less RF power for the same energy gain. Now, substituting the data from Table 3.1 into Equations 3.71 and 3.72, the capital costs of both the conventional DTL and QA-DTL are obtained:

$$\begin{aligned} C_l^{DTL} &= \frac{(5.1 l^{DTL} + 1.2 N_{cell}^{DTL})}{l^{DTL}} C'_{dt}, \\ C_l^{DTL} &= \frac{(5.1 \cdot 6.4 + 1.2 \cdot 104)}{6.4} C'_{dt}, \\ C_l^{DTL} &\simeq 24.6 C'_{dt}, \end{aligned} \tag{3.73}$$

$$\begin{aligned} C_l^{QA} &= \frac{\left(5.1 l^{QA} + 0.8 N_{cell}^{QA}\right)}{l^{QA}} C'_{dt}, \\ C_l^{QA} &= \frac{(5.1 \cdot 4.65 + 0.8 \cdot 57)}{4.65} C'_{dt}, \\ C_l^{QA} &\simeq 14.9 C'_{dt}. \end{aligned} \tag{3.74}$$

The difference between the capital costs of the conventional DTL and the QA-DTL is obtained by comparing Equations 3.73 and 3.74:

$$C_l^{cmp} = \frac{C_l^{DTL} - C_l^{QA}}{C_l^{DTL}} \cdot 100\% = \frac{24.6 C'_{dt} - 14.9 C'_{dt}}{24.6 C'_{dt}} \cdot 100\% \simeq 39\%. \tag{3.75}$$

Observing Equation 3.75, it can be noticed that the capital cost of the QA-DTL is 39% lower in comparison to the conventional DTL.

In order to compute the total cost for both the conventional DTL and QA-DTL, the rest of the data from Table 3.1 is substituted into Equation 3.67:

$$C_{tot}^{DTL} = \left(l^{DTL} + \frac{P_d^{DTL} Z T_{DTL}^2}{(\frac{\Delta W^{DTL}}{q l^{DTL}})^2} \right) C_l^{DTL},$$
$$C_{tot}^{DTL} = \left(6.4 + \frac{1077.3 \cdot 10^3 \cdot 31.5 \cdot 10^6}{(\frac{48 \cdot 10^6}{4 \cdot 6.4})^2} \right) 24.6 C'_{dt},$$
$$C_{tot}^{DTL} = 394.8 C'_{dt}, \tag{3.76}$$
$$C_{tot}^{QA} = \left(l^{QA} + \frac{P_d^{QA} Z T_{QA}^2}{(\frac{\Delta W^{QA}}{q l^{QA}})^2} \right) C_l^{QA},$$
$$C_{tot}^{QA} = \left(4.65 + \frac{570 \cdot 10^3 \cdot 67.7 \cdot 10^6}{(\frac{48 \cdot 10^6}{4 \cdot 4.65})^2} \right) 14.9 C'_{dt},$$
$$C_{tot}^{QA} = 155.7 C'_{dt}. \tag{3.77}$$

Ultimately, the difference in total cost between the conventional DTL and QA-DTL is obtained by comparing Equations 3.77 and 3.76:

$$C_{tot}^{cmp} = \frac{C_{tot}^{DTL} - C_{tot}^{QA}}{C_{tot}^{DTL}} \cdot 100\% = \frac{394.8 C'_{dt} - 155.7 C'_{dt}}{394.8 C'_{dt}} \cdot 100\% \simeq 61\%. \tag{3.78}$$

The result of Equation 3.78 shows that the total cost of the QA-DTL is 61% lower than that of the conventional DTL, making it a more cost-effective option for low-energy ion acceleration applications.

3.5 Conclusions

In this chapter, the fundamental principles governing electromagnetic waves and beam behavior within linac structures were discussed. A detailed overview of the key parameters and expressions used in accelerator physics to describe wave propagation inside linac structures was provided. The working principles of both Alvarez-type and H-mode accelerating structures, along with the DEB and ERC cavities, were elaborated. Additionally, the beam dynamics within these structures were discussed, followed by an analysis of the cost efficiency of various DTL-type structures. Through this chapter, a comprehensive understanding of the underlying physics essential for the design of linac structures was established.

4. Mathematical Model for Optimizing Geometry Parameters of Linac Structures

In this chapter, the software tools used for EM field simulations and beam dynamics analysis within linac structures are discussed. All results presented in this thesis were obtained either using the 2D EM simulation software Poisson/SUPERFISH or the 3D EM simulation software CST Studio Suite. Beam dynamics analysis was conducted using the TraceWin codes. In addition to the mentioned software, the algorithms for the optimization of linac structure designs are elaborated in detail. Furthermore, two additional graphical user interfaces (GUIs) are presented, which automate the design process of Alvarez-type accelerating structures by combining the developed algorithms with the Poisson/SUPERFISH codes.

4.1 Simulation software

In this thesis, the choice of EM simulation software was based on the type of linac structure. Due to its simplicity, the 2D EM software was preferred and used for simulating the operation of DTL and QA-DTL. In contrast, the complexity of H-mode linac structures necessitated the use of 3D EM software. Beam dynamics for all the developed linac structures presented in this thesis were performed using the TraceWin software.

Poisson/SUPERFISH codes

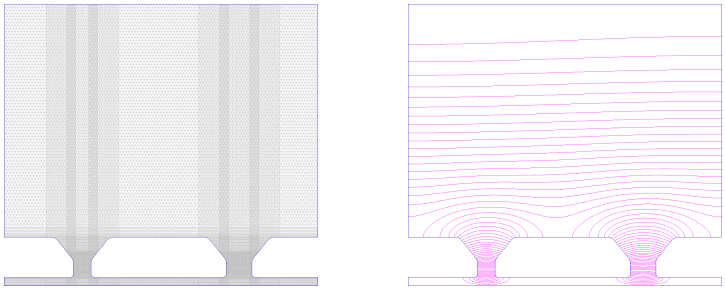
The RF designs of DTL and QA-DTL were carried out using Poisson/SUPERFISH codes, a 2D EM simulation software developed at Los Alamos National Lab (LANL) [97]. Poisson/SUPERFISH was selected since it has been benchmarked against most of the linac structures currently in operation. Poisson/SUPERFISH is a suite of programs designed for the computation of magnetostatic and electrostatic fields, and for simulating the field distribution within accelerating structures in a 2D Cartesian system [3].

Among the various programs available within Poisson/SUPERFISH, only four are relevant to this thesis: DTLfish, MDTfish, Automesh, and Autofish. DTLfish is used to create the geometry for individual DTL cells. It assumes a symmetric cell configuration, setting up Automesh and

Autofish for only half of the cell, thereby reducing execution time. The symmetry plane is positioned at the center of the gap, between two neighboring DTs. Additionally, DTLfish tunes the cell by adjusting one of the following parameters: drift tube diameter, cavity diameter, face angle, or cell gap, where the face angle refers to the angle between the DT face and the vertical axis in the perpendicular cross-section [98].

MDTfish generates the geometry for multiple DTL cells. Typically, each cell is first designed with DTLfish, and then MDTfish is used to combine all the cells, creating the complete DTL structure. MDTfish also accounts for the effects of stems and post-couplers in the power and frequency calculations. Automesh and Autofish are more complex to use compared to DTLfish and MDTfish, but their added flexibility makes them more suitable for designing QA-DTL structures. Automesh first generates the mesh data and then optimizes the triangular mesh for all available solvers and tuning programs [99]. Autofish is a powerful tool within Poisson/SUPERFISH that integrates Automesh, the RF field solver Fish, and a postprocessor into a single program [99]. The Fish solver calculates the solution to Ampere's Law over a closed region formed by triangular plates, which are generated by Automesh [100].

As an example, a two-cell structure with defined points is illustrated in Appendix A-1. The segment of the code from the Automesh control file, which defines the geometry of the mentioned two-cell structure and its material properties, is shown in Appendix A-2. Figure 4.1a represents the triangular mesh of the two-cell structure generated with Automesh, and Figure 4.1b shows the EM field distribution after applying the Fish solver to the output data provided by Automesh.



(a) **(b)**

Figure 4.1: (a) Triangular mesh of a two-cell structure generated with Automesh; (b) EM field distribution obtained after applying the Fish solver to the output data provided by Automesh.

CST Studio Suite

In the case of 3D EM simulation software, *CST Studio Suite* was used due to its versatility, high accuracy in solving Maxwell's equations, and its eigenmode solver, particularly suited for high-frequency linac structure design [4].

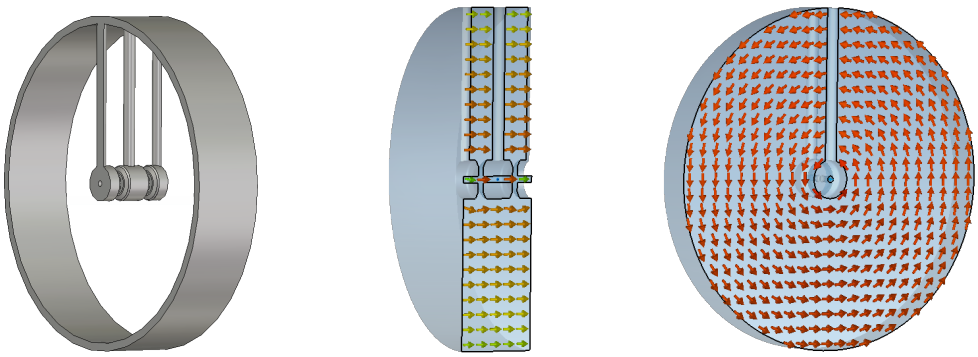
CST Studio Suite has a built-in template named *Particle Dynamics*, which contains various workflows. The one relevant to this thesis is titled *Cavities* and is located under the *Accelerator*

Components application area. Within this template, analyses such as *Eigenmode Analysis*, *Wakefields*, or *Particle Analysis* can be performed.

CST Studio Suite includes a dedicated panel for creating 3D objects essential for modeling linac structures. One of its most notable features is the ability to parameterize models, allowing users to modify any geometric parameter simply by selecting the object and editing its properties [101]. To further enhance convenience, users can create a list of variables and assign them to specific dimensions of the objects, making parameter adjustments more efficient and streamlined.

One of the most commonly used solvers for designing accelerating structures is the Eigenmode solver, which calculates a finite number of EM field modes within a closed device [101]. Since simulation time depends on the number of modes being calculated, it is preferable to compute only the necessary modes. Additionally, CST Studio Suite provides three symmetry planes, each of which reduces simulation time by a factor of two. Users can also define the starting frequency for mode calculations to help the solver converge more quickly to a solution. Once the simulation is complete, all required output data can be accessed through the *post-processing* section of CST Studio Suite.

For clarity, a two-cell structure has been modeled in CST Studio Suite. The Eigenmode solver was then used to calculate the first occurring mode. The 3D model of the cavity, along with the calculated electric and magnetic field distributions, is illustrated in Figure 4.2.



(a) **(b)** **(c)**

Figure 4.2: (a) The 3D model, (b) the electric field distribution, and (c) the magnetic field distribution, created in CST Studio Suite.

TraceWin codes

The beam dynamics simulations were performed using TraceWin codes due to their capability to simulate complex beamline configurations, accurately account for space charge effects, and provide detailed insights into particle trajectories, phase space evolution, and beam losses. In addition, they offer powerful optimization tools to enhance accelerator performance and minimize emittance growth [5]. TraceWin contains the Partran codes, which allow the use of multi-particle simulations and the selection of the input beam distribution. Additionally, TraceWin includes

the PlotWin tool, which plots the transverse and longitudinal beam phase spaces after each component and estimates their emittances in the different planes [102].

Before running TraceWin, the input beam's normalized rms emittances for all three phase spaces (i.e., XX', YY', and ZZ') need to be provided. Additionally, parameters such as peak beam current, input kinetic energy, number of injected particles, and the accelerating structure's resonant frequency need to be defined before initiating beam simulations.

TraceWin includes a nuclear data table containing over 4,390 particles available for simulation. If the desired particle is not listed, the user can manually define it by specifying its charge number and rest mass. Under the multi-particle section, the user can select the Partran codes and use one of the predefined input beam distributions, such as 4D-KV distribution, 6D-Uniform distribution, 6D-Parabolic distribution, or 6D-Gaussian distribution. These distributions are illustrated in Figure 3.11.

TraceWin includes a set of components that the user can use. Specifically, for linac structures, the key components essential for their design are QUAD, DRIFT, and GAP.

The QUAD component specifies the properties of quadrupole magnets, including quadrupole length, gradient strength, and bore radius, which are necessary for studying transverse beam focusing.

The DRIFT component represents regions within the linac where the beam is not subjected to a magnetic field for transverse focusing or an electric field for acceleration. The parameters defining this component are drift length and bore radius.

The GAP component describes the space between neighboring drift tubes, where particles are exposed to an external EM field and undergo acceleration. To properly model the gap, parameters such as effective gap voltage, synchronous phase, and bore radius must be defined.

Before running TraceWin, the Twiss parameters at the input of the linac, as explained in Subsection 3.2.2, must be defined. Upon successful completion of the simulation, TraceWin provides the user with envelopes, phase spaces, and other required data. Alternatively, instead of Twiss parameters at the input of the linac, it is possible to define the lattice and specify transverse phase advance, which will trigger the beam matching after running TraceWin. In this case, TraceWin calculates the $\beta(s)$ function using Equation 3.40, followed by the calculation of $\alpha(s)$ function using Equation 3.41, and $\gamma(s)$ function using Equation 3.42. In this case, by running TraceWin, the gradient strength for each quadrupole magnet will be calculated.

4.2 Graphical User Interface for optimization of Alvarez and Quasi-Alvarez DTL cells

During the design process of DTL and QA-DTL cavities, it is necessary to run Poisson/ SUPERFISH codes multiple times to achieve the optimized results, which can be a very time-consuming process. To streamline this, the author developed two Graphical User Interfaces (GUIs) using the programming language C#. These GUIs incorporate the algorithms described in Section 4.3.1 to optimize each cell and thus provide the most efficient linac structure based

on the given input data. One of the developed GUIs, called A-GUI, is used for optimizing DTL structures by maximizing effective shunt impedance per unit length (ZT^2), while the other, named QA-GUI, is specifically designed for the optimization of QA-DTL, also maximizing ZT^2. The interface of A-GUI is shown in Figure 4.3.

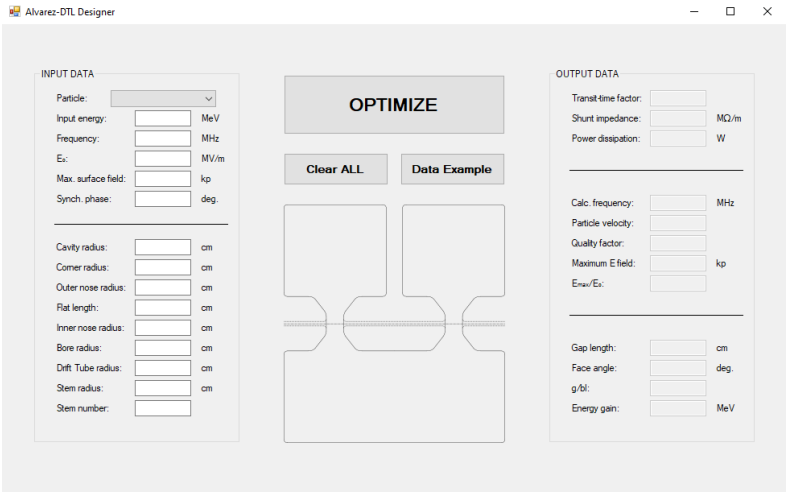


Figure 4.3: Interface of A-GUI used for optimization of DTL cells.

The developed A-GUI, presented in Figure 4.3, is divided into two sections: the input data section and the output data section. In the input data section (left side of Figure 4.3), the user must provide all necessary data to initiate the simulation, including input energy, operating (resonant) frequency, average axial electric field, maximum allowed electric field, and several geometry parameters. For clarity, selecting any input field related to geometry data automatically updates the image in the center of A-GUI with the corresponding drawing to guide the user. This dynamic change in the image, based on the selected input field of geometry data, is illustrated in Appendix B-1.

In addition to the image that visually represents the geometry corresponding to the selected input field, the middle part of the A-GUI contains three buttons: *Optimize*, *Clear ALL*, and *Data Example*. The *Data Example* button automatically populates all input fields on the left side of the A-GUI with reasonable default values to assist the user in understanding what values are expected to be entered (for more details, see Appendix B-2). The *Clear ALL* button clears the data from all input and output fields within the A-GUI. The most important button, *Optimize*, performs the complete optimization of one DTL cell by running Poisson/SUPERFISH codes consecutively in the background. This process carefully adjusts the cell geometry based on the algorithms described in Section 4.3.1, while respecting the input data provided by the user. After each run of the Poisson/SUPERFISH codes, key data such as the transit-time factor, effective shunt impedance per unit length, and power dissipation are automatically filled in the output fields on the right side of the A-GUI.

For visualization purposes, the interface of the A-GUI after the successful optimization of one cell using the example input data provided by the *Data Example* button, is shown in Appendix B-3.

On the other hand, the second developed GUI (QA-GUI) is considerably more complex than A-GUI. It facilitates the optimization of QA-DTL super-periods, which can be divided into three independent sub-cells. The interface of QA-GUI is shown in Figure 4.4.

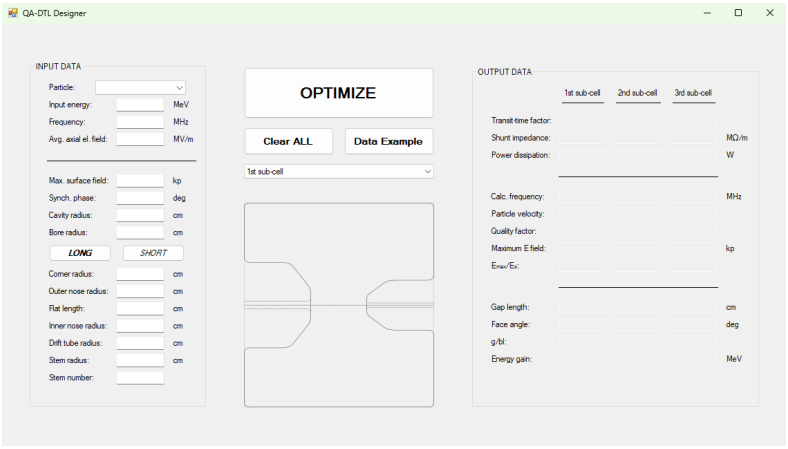


Figure 4.4: Interface of QA-GUI used for the optimization of QA-DTL super-periods.

The first noticeable difference between QA-GUI and A-GUI is the inclusion of a drop-down list for selecting the sub-cell, along with a corresponding descriptive image. QA-GUI is specifically adapted for QA-DTL structures with a periodicity factor of $n_p = 2$, as described in Subsection 3.3.2. The first and third sub-cells contain DT halves with different geometric parameters, which trigger two additional buttons to appear when the user is inputting data for them, named *LONG* and *SHORT*. The middle (second) sub-cell, which consists of two identical DT halves, does not require these buttons, and therefore they disappear in this context.

Another key difference between QA-GUI and A-GUI is the format of the output data. While A-GUI provides output data for individual cells, QA-GUI provides output for super-periods, offering three different sets of data corresponding to each sub-cell. Similar to A-GUI, QA-GUI also includes a *Data Example* button, which serves the same purpose - to populate the fields with reasonable example values to guide the user. The interface of QA-GUI after interacting with the *Data Example* button is shown in Appendix B-4.

Once the user provides all the required input data, the *OPTIMIZE* button can be activated. This initiates the optimization of the QA-DTL super-period and cannot be interrupted until the simulation is complete. Upon finishing the optimization, the descriptive image updates to show the complete super-period, clearly highlighting each sub-cell. Additionally, all computed data are presented in the corresponding fields of the output data section, as illustrated in Appendix B-5. Lastly, the *Clear ALL* button can be activated to reset all input and output fields. The interface of QA-GUI after activating the *Clear ALL* button can be found in Appendix B-6.

4.3 RF design and beam dynamics procedures

Regardless of the type of linac structure, four key parameters must be determined before the design process: input energy (W_{IN}), output energy (W_{OUT}), resonant frequency (f_{res}), and the desired particle for acceleration (designed particle). The design process starts by defining the type of linac structure, followed by the calculation of the length of the first cell, which is determined by the synchronicity condition. In other words, the cell length is computed using one of the corresponding equations, ranging from Equation 3.23a to Equation 3.23c, depending on the SW mode of the linac structure.

After calculating the length of the first cell, the corresponding algorithms are applied iteratively until the most efficient cell is obtained. The efficiency of the cell is reflected by one of the figures of merit, the effective shunt impedance per unit length (ZT^2), which must be maximized to ensure the optimal performance for beam acceleration.

After obtaining the optimized geometry parameters of the most efficient first cell, the *Panofsky equation* (Equation 3.8) is applied to calculate the energy gain within the designed cell and, therefore, determine the input energy of the next cell. In this process, it is necessary to define the synchronous phase, which is important for longitudinal beam dynamics, as described in Subsection 3.2.1. Along with the synchronous phase, the average axial electric field must satisfy Equation 3.66, which ensures that the total cost of the structure is minimal. The transit-time factor is obtained after a successful EM simulation of the designed cell.

The process of obtaining the most efficient cell is repeated until the output energy of the last designed cell exceeds the desired output energy of the linac structure, which was defined at the beginning of the design process. In other words, the design process stops as soon as the following condition is no longer satisfied:

$$W_{IN}^{(i)} + \Delta W^{(i)} \leq W_{OUT}, \tag{4.1}$$

where the $W_{IN}^{(i)}$ is the input energy of the designed cell, and $\Delta W^{(i)}$ is the energy gain in that cell.

Usually, the most efficient design of a linac structure (cavity) takes the shape of a cone, as its radius decreases with each following cell, maintaining the maximal ZT^2 and desired resonant frequency. Unfortunately, the conical shape of the linac structure is more complicated to produce, and its manufacturing cost is much higher than that of the cylindrical shape. Therefore, a compromise must be made, and the average value of the cavity radii of all optimized cells has been chosen as the cavity radius for the designed linac, shaping it into a cylinder. The expression for the cavity radius (R_{cav}) is as follows:

$$R_{cav} = \frac{\sum_{i=1}^{N} R_{cav}^{(i)}}{N}, \tag{4.2}$$

where N represents the total number of cells and $R_{cav}^{(i)}$ is the cavity radius of the i-th cell. After defining the cavity radius for the linac structure, the geometry of each cell must be adjusted to

maintain the resonant frequency at the desired value.

It is important to emphasize that during the design process, there is always one parameter that needs to be adjusted to maintain the resonant frequency at the desired value. In other words, one parameter is reserved for fine-tuning, while the remaining parameters must be optimized to achieve the highest possible ZT^2.

After completing the design of each cell and obtaining all the geometry values, beam dynamics analysis must be performed using multi-particle simulation software, such as TraceWin. During this process, both transverse and longitudinal beam dynamics are analyzed, as they influence the dimensions, strength, and type of quadrupoles used for transverse beam focusing. The quadrupole is characterized by its gradient strength, calculated using Equation 3.36, which in the case of a linac at the pole tip of a quadrupole magnet becomes [45]:

$$G = \frac{B}{R_b}, \tag{4.3}$$

where B is the magnetic induction generated by the quadrupole, and R_b is the bore radius. One of the main considerations during beam dynamics simulations is to prevent high quadrupole gradients. For instance, in the case where the quadrupole is made of samarium cobalt (Sm_2Co_{17}) material, the magnetic induction of quadrupoles should not exceed 1 T at any moment [103]. If the gradient cannot be reduced below the maximum allowed value, adjustments to the linac structure must be made. One option is to increase the input energy (if possible), which would result in the removal of the first few critical cells of the structure, while another is to modify some of the geometry parameters of the drift tubes. Regardless of how small the adjustment to the geometry may be, every step of the RF simulation, as explained at the beginning of this section, must be redone.

4.3.1 Optimization algorithms used in RF design of Alvarez-type structures

As long as the chosen linac structure is of the Alvarez type, the RF design process remains generally the same. In the case of QA-DTL, each super-period is divided into three independent sub-cells. The following algorithms are applied to each of these sub-cells, with a slight difference in the first and last sub-cells, as they consist of DTs with different geometric parameters.

The geometry of each cell is optimized for maximum ZT^2. During the design process, several constraints must be respected:

1. Every DT within the DTL, or every long DT within the QA-DTL, must be long enough to accommodate the quadrupole magnet.

2. The maximum electric field within the linac structure must not exceed the defined Kilpatrick limit in order to prevent potential electrical breakdowns.

3. The bore radius must be large enough to prevent beam interaction with the DT walls, thus avoiding unnecessary beam losses.

4. Every cell must resonate at the desired resonant frequency.

To meet all the aforementioned constraints, the geometry parameters shown in Figure 4.5 must be carefully selected for each cell during the design process.

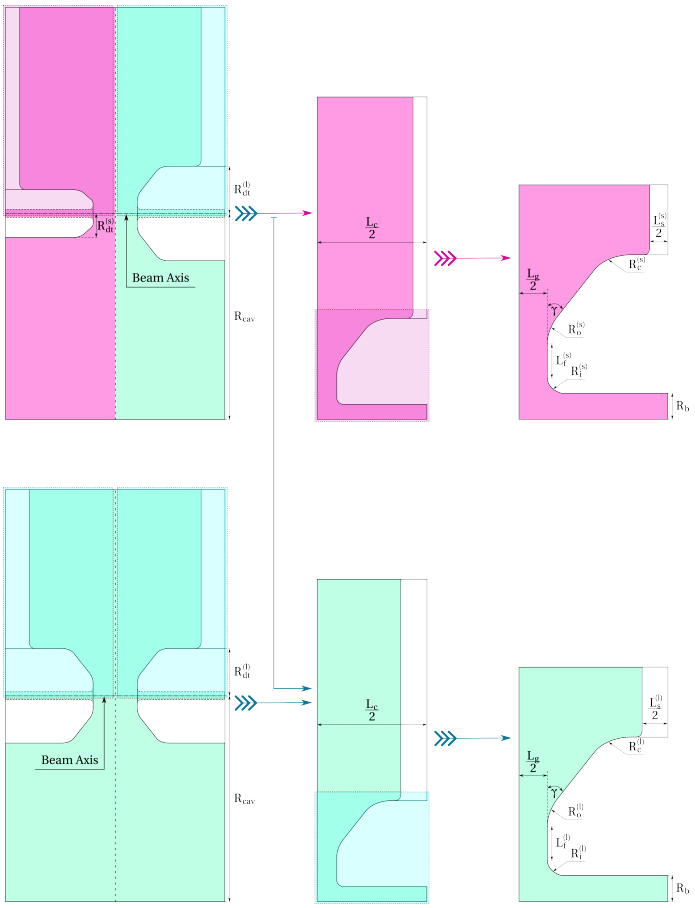


Figure 4.5: (Top) First or last sub-cell of QA-DTL super-period; (bottom) middle sub-cell of QA-DTL super-period or cell of DTL; with geometry parameters: L_s - Stem diameter, L_g - Gap length, L_c - Cell length, R_{cav} - Cavity radius, R_{dt} - Drift tube radius, R_c - Corner radius, γ - Face angle, R_o - Outer nose radius, L_f - Flat edge length, R_i - Inner nose radius, R_b - Bore radius (adapted from [98]). Index s exists only in QA-DTL and denotes the shorter DT, while the index l exists in both QA-DTL (for the longer DT) and DTL (for every DT).

From Figure 4.5, the reader can observe eleven parameters that fully define the DTL cell and seventeen parameters that fully define the QA-DTL super-period. All of these parameters influence the EM field distribution and the efficiency of the linac structure. The parameters optimized for each cell individually include the cavity radius (R_{cav} - explained in Section 4.3), face angle (γ), cell length (L_c), and gap length (L_g), while the remaining parameters are kept constant for all cells within the designed linac structure.

Since both DTL and QA-DTL are 0-mode structures, the length of each cell is determined according to Equation 3.23a. The other three mentioned parameters must be optimized by any means to achieve the most efficient design - maximizing ZT^2. Given their importance, corresponding algorithms have been developed. Regarding the gap length, it influences both the effective shunt impedance per unit length and the maximum electric field in DTL and QA-DTL cells. The effect of gap length variation on each parameter is illustrated in Figure 4.6.

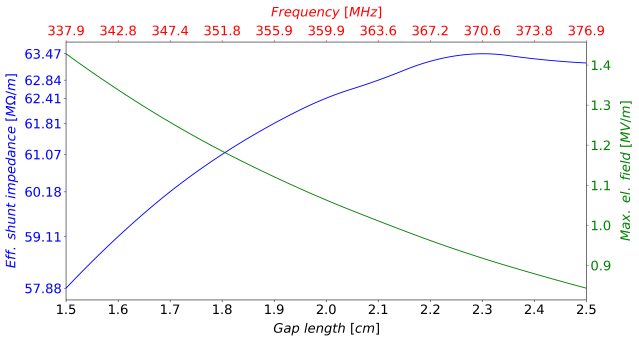


Figure 4.6: The impact of different gap lengths on the effective shunt impedance per unit length, maximum electric field in the cell, and resonant frequency of the cell. The rest of the parameters are fixed: R_{cav} = 25 cm, γ = 10 ° and L_c = 10 cm.

As shown in Figure 4.6, increasing the distance between two neighboring drift tubes leads to an increase in the effective shunt impedance per unit length, which reaches a maximum at a specific gap length, and a decrease in the maximum electric field - both of which are positive outcomes. However, the resonant frequency also increases rapidly and must be compensated for by adjusting other parameters.

Along with the gap length, the optimal value of the cavity radius plays a crucial role in the design process. The effect of different cavity radii on the effective shunt impedance per unit length, maximum electric field, and resonant frequency is illustrated in Figure 4.7.

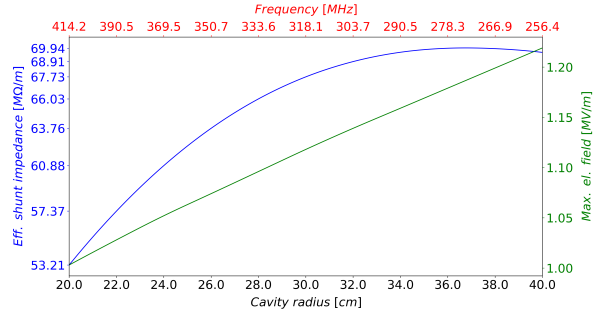


Figure 4.7: The impact of different cavity radii on the effective shunt impedance per unit length, maximum electric field in the cell, and resonant frequency of the cell. The rest of the parameters are fixed: L_g = 2 cm, γ = 10 ° and L_c = 10 cm.

By observing Figure 4.7, the reader can notice the linear increase of the maximum electric field inside the cell, while the resonant frequency decreases rapidly. By adjusting both the cavity radius and gap length, it is possible to find the optimal values that maximize the effective shunt impedance per unit length, while keeping the resonant frequency at the designed value. However, it is often preferable to have the same cavity radius for all cells rather than different radii for each cell due to the significant difference in manufacturing costs and complexity. Therefore, to design the linac structure, besides cell length and cavity radius, one additional parameter must be considered, which, in the case of DTL and QA-DTL, is the face angle (γ).

Since the face angle directly impacts the size of the DT, when it is adjusted, an additional boundary needs to be considered: the space for the quadrupole magnets within every DT in the case of DTL or within every long DT in the case of QA-DTL. The effect of different face angles on the effective shunt impedance per unit length, maximum electric field, resonant frequency, and available space for the permanent magnet quadrupole (PMQ) is shown in Figure 4.8.

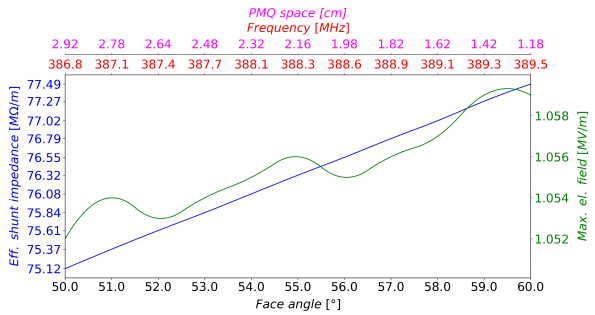


Figure 4.8: The impact of different face angles on the effective shunt impedance per unit length, the maximum electric field in the cell, the resonant frequency of the cell, and space for the PMQ within the DT. The rest of the parameters are fixed: L_g = 2 cm, R_{cav} = 25 cm and L_c = 10 cm.

When the face angle is changed by more than 10°, the maximum electric field remains practically the same. However, this becomes a significant factor and cannot be neglected when designing the cells for the acceleration of low-velocity particles due to the small gap length. The effective shunt impedance per unit length does not change much but increases linearly. The resonant frequency also changes slowly, while the space for the PMQ within the DT decreases rapidly. Based on the observed characteristics, the face angle is well-suited for fine-tuning, as the high precision of the desired parameters can be achieved by adjusting it.

Now, the logical question arises: how can the mentioned parameters be optimized to obtain the most efficient cell with the highest possible ZT^2? To answer this question, several algorithms have been developed. The algorithm outlining the complete procedure for designing DTL and QA-DTL from start to finish is presented in Figure 4.9.

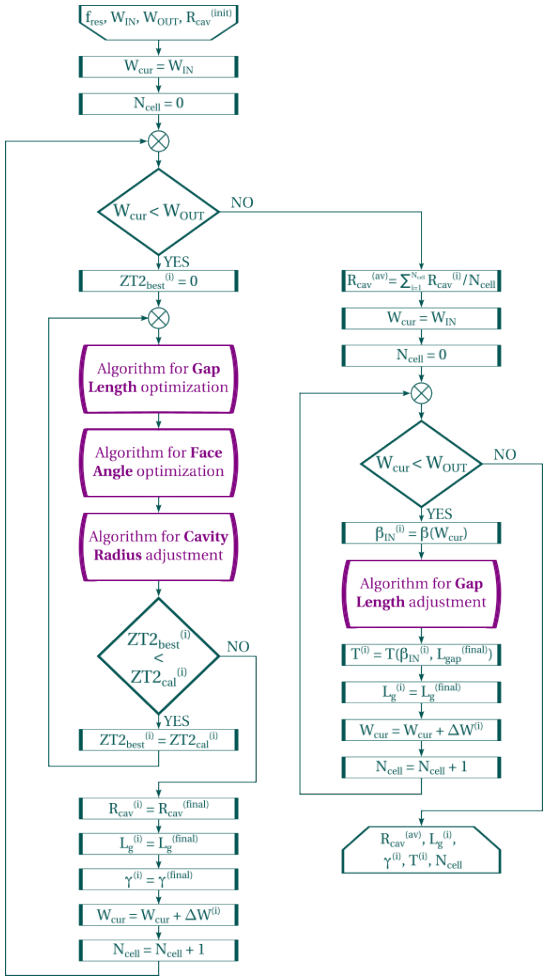


Figure 4.9: Algorithm for designing the most optimal DTL and QA-DTL for the highest effective shunt impedance per unit length.

The parameters in Figure 4.9 are defined as follows:

- W_{cur} - Input energy of the cell currently being designed;
- N_{cell} - Number of cells within the designed linac structure;
- $ZT2_{best}$ - Maximum effective shunt impedance per unit length obtained for the designed cell;
- $ZT2_{cal}$ - Calculated effective shunt impedance per unit length for the cell currently being designed;
- ΔW - Energy gain in the cell being designed, calculated using Equation 3.8;

- $\beta(W_{cur})$ - Particle velocity corresponding to the W_{cur} energy;

The Figure 4.9 illustrates the procedure for optimizing each cell individually of the Alvarez-type structure to achieve the highest ZT^2, given the input (W_{IN}) and output (W_{OUT}) energies. The optimization is achieved through the interchangeable use of three separate algorithms, each developed for optimizing or adjusting different parameters: gap length, face angle, and cavity radius. The goal is to design all cells with the highest effective shunt impedance per unit length (i.e., the highest value of $ZT2_{best}$).

After designing each cell, the values of cavity radius, gap length, and face angle are stored. Once all cells are designed and the linac structure is complete, the average cavity radius across all cells is calculated. The design process is then repeated using the calculated average cavity radius. As previously mentioned, even a small change in cavity radius affects the resonant frequency in each gap, which requires subsequent correction. This correction is achieved by adjusting the gap length, for which an additional algorithm has been developed.

The algorithm in Figure 4.9 consists of two sub-algorithms for optimization and two sub-algorithms for adjusting the linac structure parameters, namely gap length, face angle, and cavity radius. The algorithm for optimizing the gap length is shown in Figure 4.10.

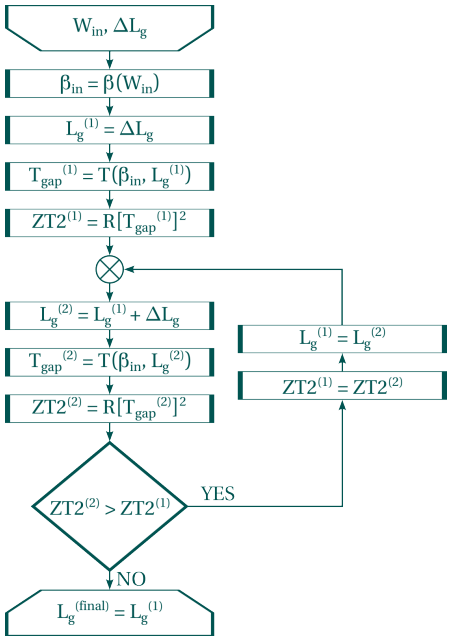


Figure 4.10: Algorithm for optimizing gap length to achieve the highest effective shunt impedance per unit length.

By observing Figure 4.10, it can be noted that each gap is optimized for the highest effective shunt impedance per unit length, calculated according to Equation 3.14. A more complex algorithm for the optimization of the face angle of each drift tube was developed, which is shown in Figure 4.11.

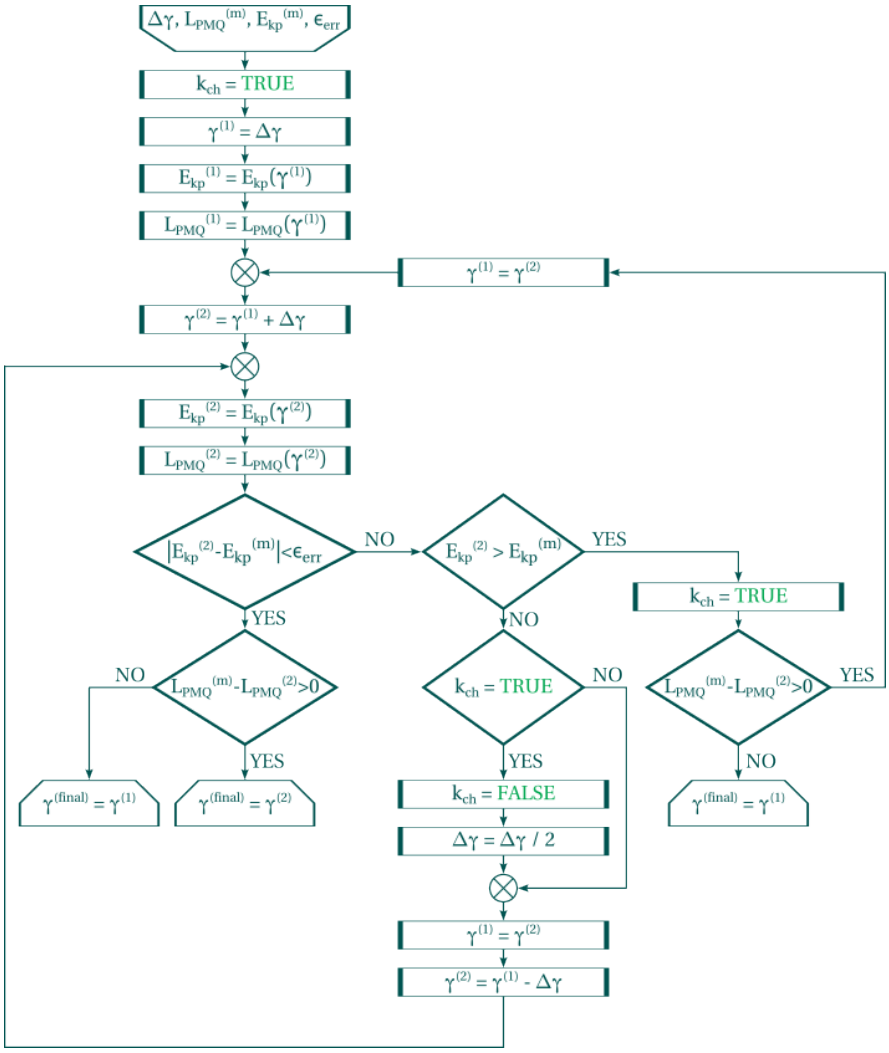


Figure 4.11: Algorithm for the optimization of the face angle to achieve the highest effective shunt impedance per unit length.

In the algorithm shown in Figure 4.11, the step value for increasing or decreasing the face angle in the next iteration ($\Delta\varphi$) is controlled by the auxiliary variable k_{ch}. The variable ϵ_{err} represents the maximum acceptable difference between the calculated and allowed Kilpatrick field value (E_{kp}), which is defined by Equation 3.19. Finally, L_{PMQ} provides information about the available space for the PMQ within the designed drift tube. Additionally, the algorithm for adjusting the cavity radius is shown in Figure 4.12.

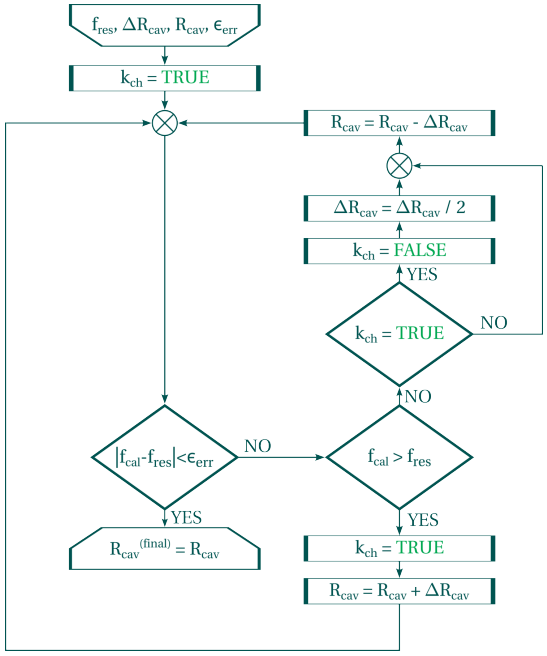


Figure 4.12: Algorithm for adjusting the cavity radius to achieve the resonant frequency.

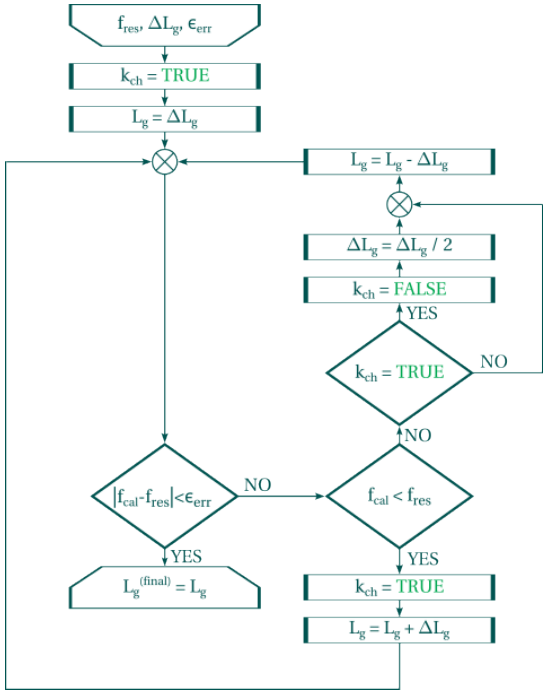


Figure 4.13: Algorithm for adjusting the gap length to achieve the resonant frequency.

Similarly to the previous algorithm, the variables ϵ_{err} and k_{ch} are required for the same purpose, but refer to different parameters. In the case of the algorithm for adjusting the cavity radius, the auxiliary variable k_{ch} is used to control the step size for increasing or decreasing the cavity radius in the following iteration. On the other hand, ϵ_{err} represents the maximum acceptable difference between the calculated and desired resonant frequency. Lastly, the algorithm for adjusting the gap length has been developed, as shown in Figure 4.13. In comparison to the algorithm from Figure 4.12, the variable k_{ch} in this case is used to control the step size for increasing or decreasing the gap length instead of the cavity radius.

4.3.2 Optimization algorithms used in RF design of H-mode type structures

Since the main focus of this thesis is the development of the QA-DTL, the design process of the H-mode type structures will not be presented in as much detail as the Alvarez-type structures. Still, all the required steps for obtaining a power-efficient structure will be introduced. Firstly, the RF design process of the IH-DTL is shown in this subsection, followed by the design process of its modification, the S-IH-DTL.

Due to the complexity of the geometry, the RF design of the IH-DTL cannot be performed with 2D EM simulation software such as Poisson/SUPERFISH codes. Instead, more sophisticated 3D EM software, such as CST Studio Suite, must be used.

One of the characteristics of the IH-DTL is the absence of quadrupole magnets within the drift tubes, which are normally used for transverse beam focusing. Instead, IH-DTL employs quadrupoles in a doublet or triplet configuration after a certain number of cells, depending on the design. This arrangement considerably increases the complexity of the beam dynamics.

The drift tubes of the IH-DTL do not have face angles, as in the case of DTL and QA-DTL. Instead, they feature *bulges* at the end of each drift tube, which are used for electric dipole compensation to prevent the parallel displacement of the beam [104]. Since the IH-DTL operates in the TE mode rather than the TM mode, special attention must be paid to undercuts, as they affect the gap voltage distribution along the structure [104]. Considering all the mentioned aspects of the IH-DTL, the procedure for designing this linac structure is shown in Figure 4.14.

The first two columns of the algorithm shown in Figure 4.14 are similar to those in the algorithm demonstrated in Figure 4.9, with the difference being the absence of the sub-algorithm for face angle optimization. The sub-algorithms for gap length optimization, cavity radius adjustment, and gap length adjustment are the same as those developed for the DTL, and they are shown in Figures 4.10, 4.12, and 4.13, respectively. During the design of the IH-DTL, two additional sub-algorithms were introduced. One of these sub-algorithms is developed specifically for quadrupole placement within the structure, which heavily depends on beam dynamics analysis and is explained in detail in the following subsection. The other sub-algorithm illustrates the design process of the undercuts, which are responsible for guiding the total magnetic flux of the cavity [105], while also having an impact on the gap voltage distribution along the structure. The

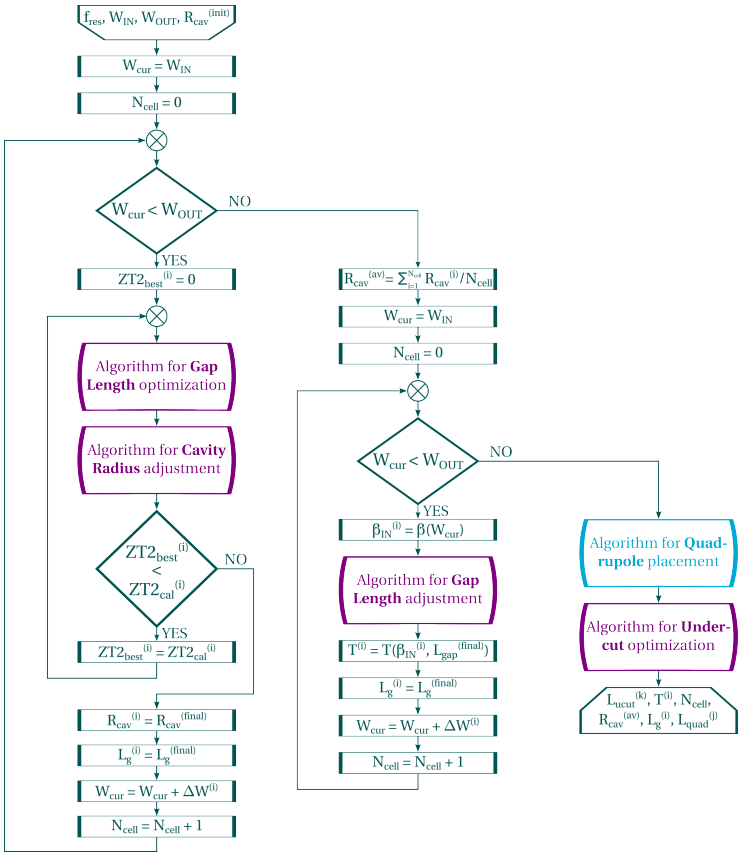


Figure 4.14: Algorithm for designing the IH-DTL for the highest effective shunt impedance per unit length.

procedure for designing the undercuts is shown in Figure 4.15.

Observing Figure 4.14, the reader can notice that the initial steps of the IH-DTL design process are the same as those for the DTL, while the final steps differ. While searching for the most optimal cavity radius, each cell is carefully simulated without considering quadrupoles. Once the cavity radius has been calculated for each cell, the average value is computed and taken as the final cavity radius. With the cavity radius defined, all gaps are slightly adjusted to ensure that each cell resonates at the desired frequency.

Subsequently, the number and optimal locations of the quadrupole magnets must be determined, which heavily depends on beam dynamics. Therefore, the design steps for selecting the number and optimal placement of quadrupoles are explained in the following subsection. After placing all required quadrupoles, the undercuts must be designed. The undercuts are denoted as $L_{ucut}^{(1)}$ and $L_{ucut}^{(2)}$, as illustrated in Figure 4.16.

Both $L_{ucut}^{(1)}$ and $L_{ucut}^{(2)}$ must be carefully chosen during the design process. The length $L_{ucut}^{(2)}$ is always greater than $L_{ucut}^{(1)}$. Any change in $L_{ucut}^{(2)}$ affects the cavity's resonant frequency. To

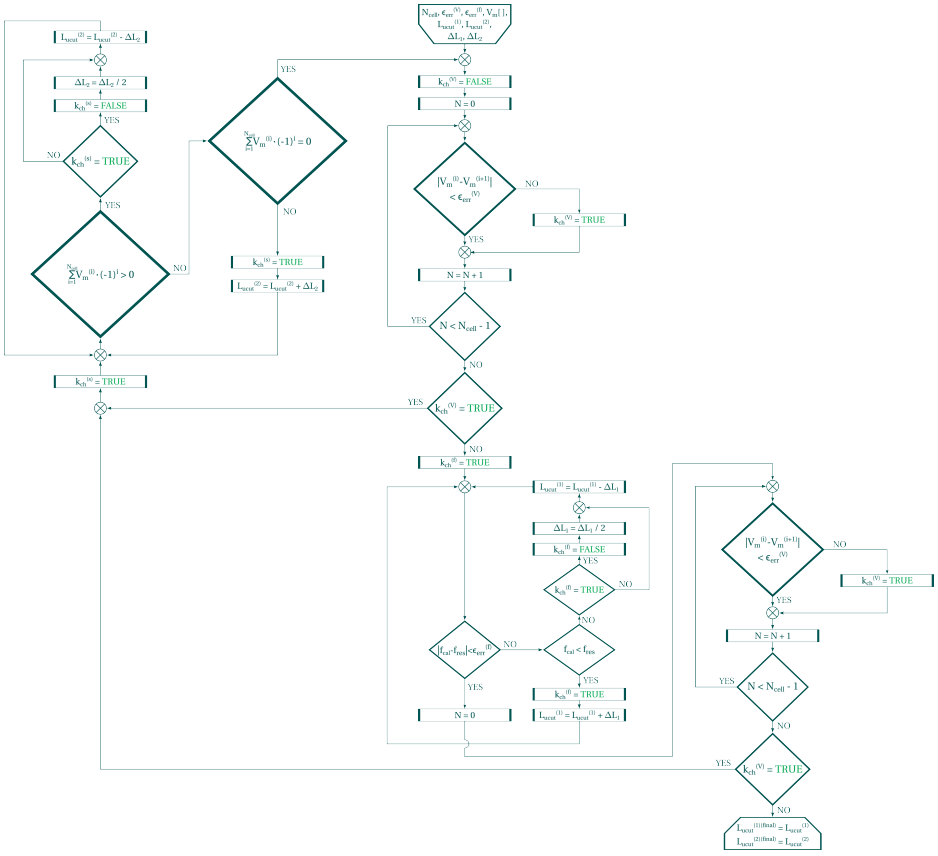


Figure 4.15: Algorithm for designing undercut of H-mode type structures.

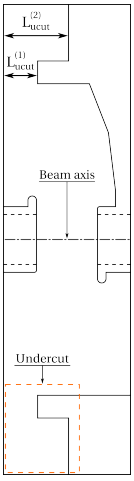


Figure 4.16: The section of the H-mode type cell with highlighted undercuts.

correct this, $L_{ucut}^{(1)}$ must be adjusted, which in turn slightly influences the voltage distribution within gaps. This iterative process of selecting $L_{ucut}^{(1)}$ and $L_{ucut}^{(2)}$ is repeated until both a uniform gap distribution and the desired cavity resonant frequency are achieved.

By following all the above-mentioned design steps, the complete IH-DTL structure is obtained. In contrast, the design process of the S-IH-DTL differs slightly from that of the IH-DTL - the algorithms used for designing the complete IH-DTL structure are now applied to the design of each S-IH-DTL cavity. Unlike the IH-DTL, the S-IH-DTL consists of multiple shorter cavities separated by quadrupole magnets. This design approach provides greater flexibility, since the radius of each cavity can be independently optimized. Consequently, the S-IH-DTL can operate at higher frequencies compared to the IH-DTL. According to Equation 3.23c, an increase in operating frequency results in a more compact accelerating structure. However, a drawback of the S-IH-DTL is the need for additional copper walls to enclose each cavity, leading to higher power dissipation within the structure. The algorithm outlining all the design steps for the S-IH-DTL is shown in Figure 4.17, where the block enclosed by dashed lines represents the procedure for designing individual cavities.

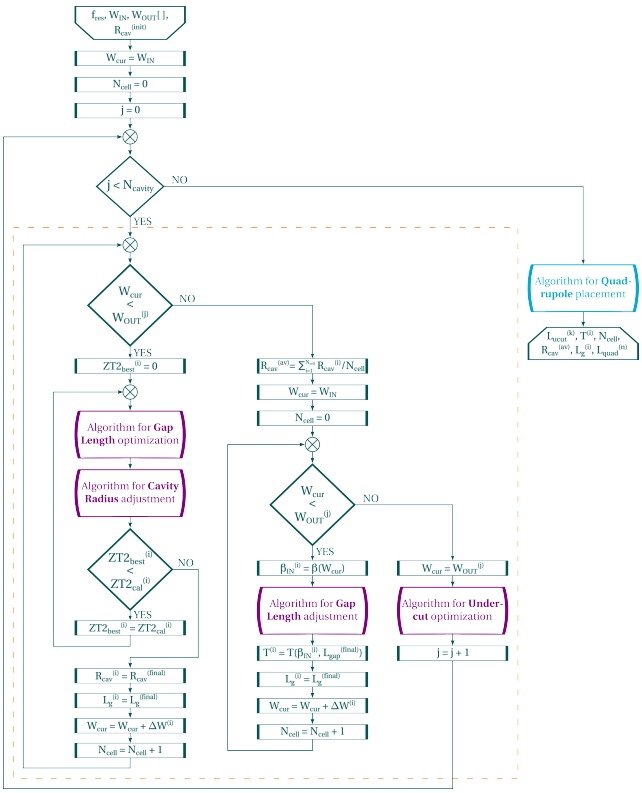


Figure 4.17: Algorithm for designing the S-IH-DTL for the highest shunt impedance per unit length.

4.3.3 Beam dynamics analysis

After performing EM simulations of the linac structures, as described in the previous subsection, the beam dynamics are analyzed. First, the obtained geometry data must be entered into multi-particle simulation software. In this study, TraceWin was chosen for this purpose, in which each cell is modeled as a combination of quadrupoles (QUAD), the drift tube space not occupied by quadrupoles (DRIFT), and the space between two drift tubes (GAP).

Every DTL presented in this thesis uses a FODO lattice, while every QA-DTL follows a FO..ODO..O configuration. On the other hand, the IH-DTL presented in this thesis employs KONUS beam dynamics.

For DTL and QA-DTL, the process begins by defining the initial length and gradient strength of each quadrupole magnet, which is adjusted by TraceWin during the matching process. After defining the length of the permanent magnet, the remaining drift tube space and bore radius are specified. The process continues by entering data for the gap between two neighboring drift tubes, a space where particles are exposed to an external electric field and gain energy. The gap in TraceWin is defined by gap voltage and synchronous phase, with particle velocity and transit time factor as optional parameters. The following steps include specifying the remaining drift space, quadrupole length, and gradient strength for the second drift tube, completing the definition of one cell of DTL.

In the case of QA-DTL, the additional two short DTs must be defined, after which the super-period is fully specified. Since the additional drift tubes do not have quadrupoles within them, in TraceWin they are entered as drifts. The same procedure is repeated for all other cells and super-periods within TraceWin. Initially, the beam must be matched, and the quadrupole gradient must be adjusted accordingly. The quadrupole gradient and particle positions are then computed while accounting for space charge effects. It is necessary to verify whether the new quadrupole gradient is physically achievable and whether beam loss occurred.

The process continues by inspecting beam envelopes and phase space to ensure they remain within acceptable boundaries. The design processes of the DTL and QA-DTL are considered complete once all these steps are successfully followed. However, if any design requirement is not met, adjustments to the quadrupoles should be made first. Since this also affects the drift space, the process in TraceWin must be repeated from the beginning. If a feasible solution cannot be found by modifying the quadrupole length, the bore radius must be adjusted. Since changing the bore radius affects the resonant frequency and transit-time factor, the entire design elaborated in Section 4.3.1 must be repeated with the updated geometry.

In the case of the S-IH-DTL, the number of cells per cavity is determined before the beam dynamics simulations, with the number being limited to five, allowing each cell to operate with a fixed negative synchronous phase, which ensures longitudinal beam stability, as explained in Subsection 3.2.1. The geometry of the drift tubes and the gap properties of the first cavity are entered into TraceWin. Subsequently, quadrupole doublets or triplets are introduced as the next elements. This process is repeated until the S-IH-DTL is fully defined. Following this, beam simulations are initiated with TraceWin to determine the appropriate quadrupole lengths and

gradients, ensuring loss-free beam transport within the cavity.

On the other side, the beam dynamics of IH-DTL are more complex than those of Alvarez-type structures or S-IH-DTL due to the irregular placement of quadrupoles along the accelerating structure, forming a *KONUS* (Combined Zero-Degree Structure) lattice. As a result, quadrupoles for transverse focusing within each drift tube are not required. To establish the KONUS lattice, quadrupole doublets or triplets are employed. Quadrupole doublets produce asymmetric beam envelopes, whereas quadrupole triplets ensure a more symmetric beam profile [106]. A doublet consists of two quadrupoles of equal length with opposite polarities, while a triplet comprises three quadrupoles, with the inner quadrupole having a polarity opposite to the outer ones, forming either an *FDF* or *DFD* configuration. Typically, the length of the inner quadrupole is approximately equal to the combined length of the outer quadrupoles [107]. Since the synchronous phase in the KONUS lattice is equal to zero, additional longitudinal beam focusing and matching are necessary. This is achieved by introducing a negative synchronous phase in the short sections following each doublet or triplet, depending on the chosen focusing system [108].

Before initiating the beam dynamics simulations, the lengths of all drift tubes and the gap properties computed using CST Studio Suite (as described in Subsection 4.3.2) are entered in TraceWin. Then, a doublet or triplet (depending on the design choice) is inserted in place of the second drift tube, and the TraceWin simulation is executed. Once the simulation is complete, the previously replaced drift tube is restored to its original position, and the next drift tube is replaced with the same type of quadrupole lens, and the process is repeated. If the quadrupole gradient exceeds the permissible limit or beam loss occurs in one of the cells before the quadrupole, the previous drift tube is replaced with a quadrupole lens, and another quadrupole lens is installed in place of the next drift tube. This sequence is repeated until the entire linac structure is defined, and the required number of quadrupole lenses is recorded.

After determining the final quadrupole positions, their lengths and gradients are fine-tuned to ensure that the beam waist in both transverse planes is positioned near the midpoint between two adjacent quadrupoles.

4.4 Conclusions

This chapter provided a comprehensive overview of the simulation tools and optimization algorithms essential for designing linac structures. The developed algorithms offer insight into the systematic approach taken throughout this study. Additionally, the graphical user interfaces (GUIs) created by the author were introduced, combining developed algorithms and Poisson/SUPERFISH codes. Lastly, the influence of geometrical parameters on output data was analyzed, highlighting their impact on the overall performance of linac structures.

5. Research Results

In this chapter, the obtained results are shown, detailing the design, analysis, and comparison of various linac structures developed for three different applications. Therefore, this chapter is divided into three sections.

The first section aims to design a linac for carbon ions, as required by the HITRI*plus* project. This linac configuration operates as a synchrotron injector for carbon ion therapy and is adaptable to any future particle therapy center that specializes in treating patients with carbon ions.

The second section is dedicated to the development of a linac for helium ions, as required by the NIMMS study at CERN. This linac will serve as a synchrotron injector for helium cancer therapy and, at the same time, for the production of radioisotopes. The benefit of the presented linac configuration within this section is its adaptability to any future particle therapy center that specializes in treating patients with helium ions.

In the last section, the design of a linac structure developed exclusively for radioisotope production is presented, without the capability to operate as a synchrotron injector. This section provides the design of a linac structure optimized for the production of ^{211}At, one of the most promising alpha-emitting radioisotopes for cancer treatment.

Throughout this chapter, comparisons between different linac structures are made, leading to the identification of optimized linac designs for two types of ion therapy, and for the production of radioisotopes, either in parallel or in standalone mode. Regarding beam simulations, a uniform 6D beam distribution has been chosen for all designs presented in this thesis.

5.1 HITRI*plus* carbon linac designs

As stated in Section 2.3, the HITRI*plus* linac consists of three sections. For the first section, two linac structures were developed: QA-DTL and S-IH-DTL, both designed to accelerate carbon ions from 0.7 MeV/u to 5 MeV/u. The conventional DTL structure was not considered at this stage, as its feasibility had already been evaluated in [1]. That study demonstrated the inefficiency in accelerating low-velocity carbon ions with the DTL due to physical constraints, stating that the lowest achievable energy for carbon ions is 1 MeV/u - significantly higher than 0.7 MeV/u, which is defined as the starting energy for the first section. However, despite its inefficiency at very low energies compared to the other linac structures presented in this chapter, the DTL remains a reliable and power-efficient structure for the acceleration of ions at energies above 3 MeV/u. Therefore, the second and third sections are composed of two DTL structures,

designed to further accelerate helium ions from 5 MeV/u to 7.1 MeV/u, and then from 7.1 MeV/u to 10 MeV/u, respectively.

5.1.1 Quasi-Alvarez Drift Tube Linac for carbon injection into synchrotron

The RF design of the QA-DTL for accelerating carbon ions from 0.7 MeV/u to 5 MeV/u was performed using the Poisson/SUPERFISH codes (Figure 5.1). Based on experience with LINAC4 at CERN, samarium cobalt (Sm_2Co_{17}) was selected as the magnetic material for the permanent magnet quadrupoles (PMQs) due to its high radiation resistance [109]. Since the strongest magnetic field that samarium cobalt can produce (remanence) is 0.9 - 1.1 T [103], the maximum allowable magnetic induction during the design was set to 1 T to ensure reliable performance during operation.

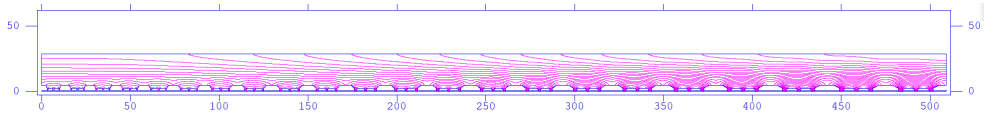


Figure 5.1: Electric field distribution in QA-DTL for carbon ion acceleration from 0.7 MeV/u to 5 MeV/u, simulated with Poisson/SUPERFISH codes.

Since this linac should also be used for the production of radioisotopes with a helium beam, the QA-DTL needs to have the ability to accelerate helium ions as well, with a nominal beam current of 5 mA, up to 5 MeV/u with 100% beam transmission.

The developed QA-DTL operates at a frequency of 352.2 MHz. The peak beam current is set at 0.6 mA for carbon ions and 5 mA for helium ions, while the average axial electric fields are 3.5 MV/m and 2.3 MV/m, respectively. In the case of helium ions, the average axial electric field, and hence the axial RF voltage, is 0.67 of the value required for carbon ions due to the difference in the charge-to-mass ratio of the accelerated particles. For carbon ions, the charge-to-mass ratio is 4/12, while for alpha particles it is 2/4, leading to a value of 0.67. At a frequency of 352.2 MHz, the Kilpatrick field level is 18.4 MV/m. For the carbon ion beams, the peak surface fields at the drift tube ends have been limited to 1.8 Kp. The synchronous phase starts at -35° for the first super-period, and increases linearly by 1° per super-period until the value of -24° is reached, ensuring stable particle acceleration. The linac structure has a total length of 5.1 meters, with a radius of 28.7 cm. The power dissipation of QA-DTL is 626 kW in case of carbon ion acceleration and 280 kW when helium ions are accelerated. The QA-DTL incorporates 22 super-periods (with a periodicity factor of 2), with an effective shunt impedance per unit length of 67.68 MΩ/m. These parameters are summarized in Table 5.1.

Table 5.1: RF and geometry parameters of the QA-DTL for carbon ion acceleration from 0.7 MeV/u to 5 MeV/u

	C-ions	**He-ions**	**Units**
Operating frequency	352.2		MHz
Input energy	8.4	2.8	MeV
Output energy	60	20	MeV
RF duty cycle	10		%
Peak beam current	0.6	5	mA
Accelerating field	3.5	2.3	MV/m
Maximal surface field	1.8	1.2	kp
Synchronous phase	-35 to -24		deg
Length	5.1		m
Cavity radius	28.7		cm
Total RF power	634	323	kW
No. of super-periods	22		-
Effective shunt impedance	67.68		MΩ/m
Nominal tank voltage	14.7	9.8	MV
Power dissipation	626	280	kW
Beam power	8	43	kW

To analyze the beam dynamics, and to define the quadrupole gradients, the TraceWin multi-particle simulation software was used. For the bore radius of 7.5 mm, the maximum allowed gradient strength for the QA-DTL design is 133.3 T/m, corresponding to a maximal magnetic induction of 1 T at the pole tip. A transverse phase advance of 64° has been chosen as a compromise between beam excursions and quadrupole gradient strength. Following the successful simulation, the length and gradient strength computed with TraceWin of each PMQ are presented in Table 5.2.

The developed QA-DTL ensures 100% beam transmission for both carbon and helium ions. The input transverse normalized rms emittance is 0.25 π.mm.mrad for carbon ions and 0.30 π.mm.mrad for helium ions, while the output values are slightly increased to 0.299 π.mm.mrad (corresponding to a 19.6% normalized rms emittance growth) and 0.317 π.mm.mrad (corresponding to a 5.7% normalized rms emittance growth), respectively, in the horizontal plane. Similarly, in the vertical plane, the output normalized rms emittance values of 0.278 π.mm.mrad (corresponding to an 11.2% normalized rms emittance growth) for carbon ions and 0.351 π.mm.mrad (corresponding to a 17% normalized rms emittance growth) for helium ions were obtained.

Table 5.2: PMQ parameters of the QA-DTL for carbon ion acceleration from 0.7 MeV/u to 5 MeV/u

No.	Grad. Str. [T/m]	Length [mm]	·	No.	Grad. Str. [T/m]	Length [mm]
1.	125.74	40	·	**12.**	-75.62	60
2.	-125.98	40	·	**13.**	72.33	60
3.	119.61	40	·	**14.**	-72.36	60
4.	-119.66	40	·	**15.**	70.07	60
5.	113.57	40	·	**16.**	-70.08	60
6.	-113.62	40	·	**17.**	67.08	60
7.	107.92	40	·	**18.**	-67.09	60
8.	-107.98	40	·	**19.**	65.39	60
9.	102.94	40	·	**20.**	-65.41	60
10.	-103.01	40	·	**21.**	63.45	60
11.	102.61	40	·	**22.**	-63.45	60

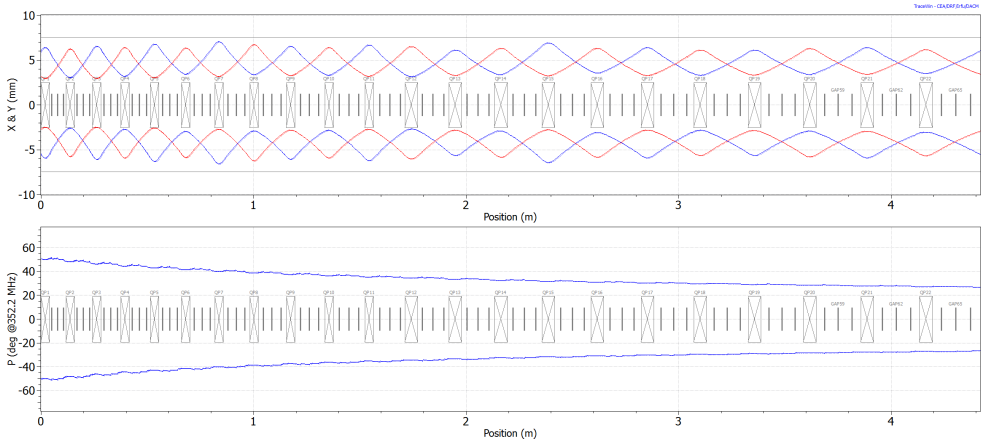
The longitudinal normalized rms emittance at the input is 1.191 π.deg.MeV for carbon ions and 0.473 π.deg.MeV for helium ions, increasing to 1.215 π.deg.MeV (corresponding to a 2.02% normalized rms emittance growth) and 0.613 π.deg.MeV (corresponding to a 29.6% normalized rms emittance growth) at the output, respectively. The final energy spread (for 95% of the beam) remains well-controlled at $\pm$0.77% for carbon ions and $\pm$1.49% for helium ions. It is important to mention that the higher longitudinal normalized rms emittance growth for helium ions does not present any issue, since the helium beam is intended to be used exclusively for radioisotope production by directing the beam onto a target positioned perpendicular to the linac. On the other hand, the carbon beam is intended for injection into the therapy synchrotron, and its normalized rms emittance growth should be kept minimal.

The beam dynamics parameters confirm the effectiveness of the QA-DTL in providing stable acceleration, and they are summarized in Table 5.3.

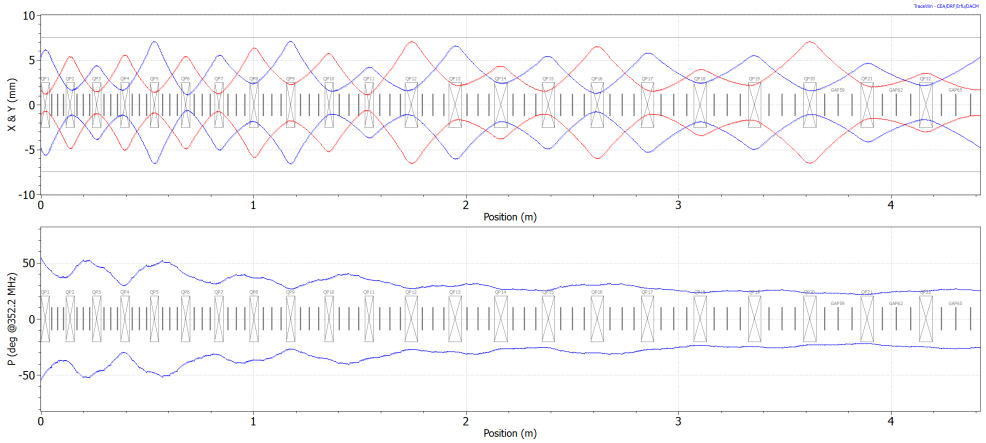
The transverse and longitudinal beam envelopes from the entrance of the QA-DTL (at 0.7 MeV/u) to its exit (at 5 MeV/u) are shown in Figure 5.2 for carbon ions at a nominal beam current of 0.6 mA, and for helium ions at a beam current of 5 mA. These envelopes provide valuable insight into the beam's evolution through the linac. To make the graphs compact and comparable, both transverse planes are plotted on one graph, with the envelope in the horizontal plane represented by the red line, and the envelope in the vertical plane highlighted by the blue line. Since the linac was optimized primarily for carbon ion injection into the therapy synchrotron, the envelopes exhibit uniform oscillations. The helium ions used for radioisotope production also ensure 100% beam transmission, but exhibit small fluctuations that do not pose a problem for the beam.

Table 5.3: Beam parameters of the QA-DTL for carbon ion acceleration from 0.7 MeV/u to 5 MeV/u

	C-ions	**He-ions**	**Units**
Bore radius	7.5		mm
Max. grad. str.	133.3		T/m
Input tran. norm. emittance (rms)(xx')	0.250	0.300	π.mm.mrad
Input tran. norm. emittance (rms)(yy')	0.250	0.300	π.mm.mrad
Output tran. norm. emittance (rms)(xx')	0.299	0.317	π.mm.mrad
Output tran. norm. emittance (rms)(yy')	0.278	0.351	π.mm.mrad
Input long. norm. emittance (rms)	1.191	0.473	π.deg.MeV
Output long. norm. emittance (rms)	1.215	0.613	π.deg.MeV
Energy spread (for 2σ (95% beam))	$\pm$0.77	$\pm$1.49	%
α_x (at output)	-2.84	-8.507	-
β_x (at output)	1.264	2.820	mm/π.mrad
α_y (at output)	0.887	0.370	-
β_y (at output)	0.345	0.116	mm/π.mrad
Transmission	100	100	%



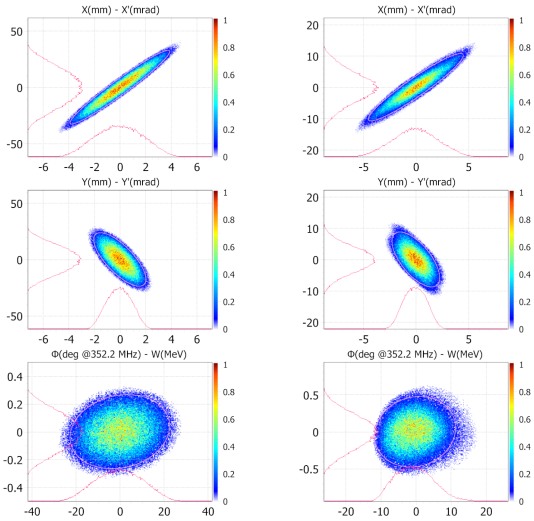
(a)



(b)

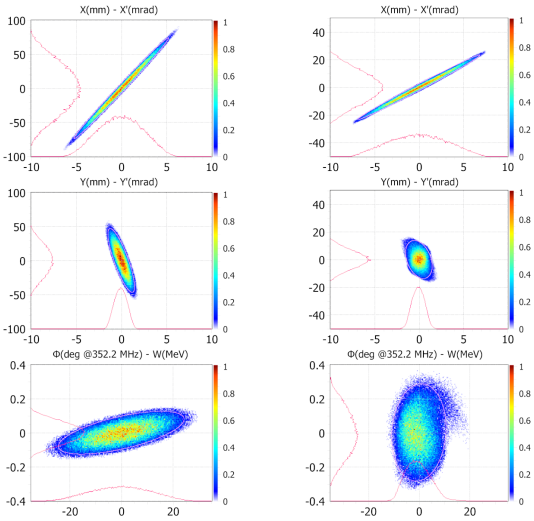
Figure 5.2: Beam envelopes along the QA-DTL from 0.7 MeV/u to 5 MeV/u for (a) carbon ions and (b) helium ions. For each accelerated ion, the top plot represents transverse beam envelopes in the xz and yz planes, while the bottom plot shows the phase envelope.

Additionally, the phase spaces showing the beam of carbon ions in the transverse and longitudinal planes at the entrance and exit of the QA-DTL are presented in Figure 5.3. The beam contains 10^5 particles.



(a) **(b)**

Figure 5.3: Carbon ion phase space (left column) at 0.7 MeV/u and (right column) at 5 MeV/u with the nominal beam current of 0.6 mA within QA-DTL.



(a) **(b)**

Figure 5.4: Helium ion phase space (left column) at 0.7 MeV/u and (right column) at 5 MeV/u with the nominal beam current of 5 mA within QA-DTL.

Similarly, the transverse and longitudinal phase spaces of helium ions, before and after

passing through the QA-DTL structure (at energies of 0.7 MeV/u and 5 MeV/u, respectively), are computed with TraceWin and are shown in Figure 5.4.

5.1.2 H-mode Drift Tube Linac for carbon injection into synchrotron

The QA-DTL design for carbon ions developed in this thesis has been compared with an alternative design of the HITRI*plus* linac, based on a 217 MHz IH-DTL, presented in [110].

Since the IH-DTL has high power efficiency (shunt impedance per unit length), but presents longitudinally unstable motion due to KONUS beam dynamics, this thesis explored a design based on a 352 MHz S-IH-DTL, which contains more quadrupole magnets, allowing for stable motion in the longitudinal phase space by using a negative synchronous phase in every gap. The RF design of the S-IH-DTL for accelerating carbon ions from 0.7 MeV/u to 5 MeV/u was performed using CST Studio Suite. The 3D model of one cavity of the S-IH-DTL structure, along with the electric field distribution within it, is shown in Figure 5.5.

The S-IH-DTL can use either quadrupole doublets or triplets for transverse beam focusing. In this thesis, both configurations were designed: the S-IH-DTL with quadrupole doublets and the S-IH-DTL with quadrupole triplets.

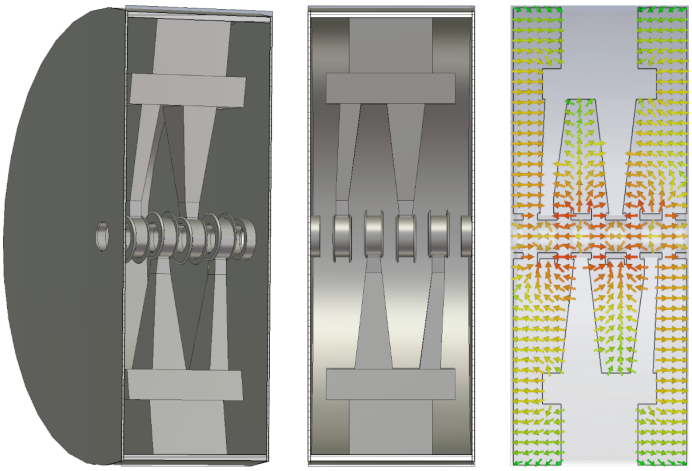


Figure 5.5: (Left and middle)The 3D model of one S-IH-DTL cavity and (right) electric field distribution within S-IH-DTL designed for carbon ion acceleration from 0.7 MeV/u up to 5 MeV/u, simulated with CST Studio Suite.

The S-IH-DTL is optimized for carbon ions, but it is also capable of accelerating helium ions. It consists of a total of 26 cavities, each with 5 cells. The quadrupoles are not placed within drift tubes, but in the space between cavities. To maintain comparability with the previous design (QA-DTL), the peak beam current of 0.6 mA for carbon ions and 5 mA for helium ions was simulated, with the average accelerating fields being 3.5 MV/m and 2.3 MV/m, respectively. The maximum surface fields for all the cavities are limited to 1.9 Kp when accelerating carbon

ions and 1.4 Kp for helium ions, thereby preventing the possible electrical breakdowns. The synchronous phase is fixed at -24°, ensuring stable motion in longitudinal phase space.

The S-IH-DTL has a total length of 5.9 meters for the configuration with quadrupole doublets and 7.3 meters for the configuration with quadrupole triplets. The cavity radius ranges from 6.6 cm in the first cavity to 10.4 cm in the last cavity, while the power dissipation of the S-IH-DTL, regardless of the quadrupole configuration, is 614 kW for carbon ions and 273 kW for helium ions.

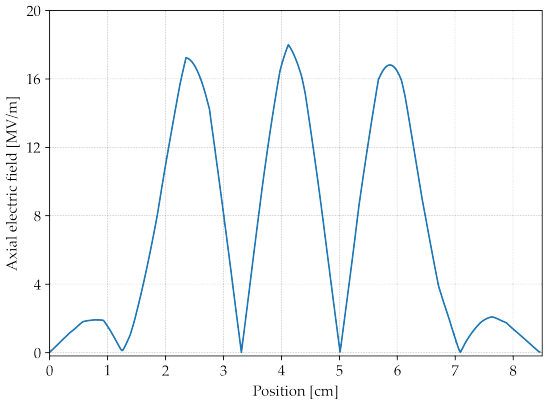
The effective shunt impedance per unit length of the first cavity is 58.93 MΩ/m and increases slightly with each subsequent cavity, reaching a value of 60.04 MΩ/m within the last cavity. The mentioned RF parameters are presented in Table 5.4.

Table 5.4: RF and geometry parameters of the S-IH-DTL for carbon ion acceleration from 0.7 MeV/u to 5 MeV/u

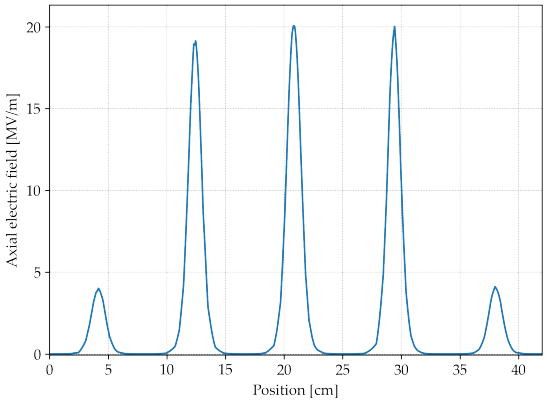
	C-ions	**He-ions**	**Units**
Operating frequency	352.2		MHz
Input energy	8.4	2.8	MeV
Output energy	60	20	MeV
RF duty cycle	10		%
Peak beam current	0.6	5	mA
Accelerated field	3.5	2.3	MV/m
Maximal surface field	1.9	1.4	kp
Synchronous phase	-24		deg
Length	5.9 / 7.3**		m
Cavity radius	6.6 - 10.4*		cm
Total RF power	622	316	kW
No. of cavities	26		-
No. of cells per cavity	5		-
Effective shunt impedance	58.93 - 60.04*		MΩ/m
Nominal tank voltage	10.4	6.9	MV
Power dissipation	614 (20.4 - 26.6*)	273 (9.1 - 11.8*)	kW
Beam power	8	43	kW
$L_{ucut}^{(1)}$	1.0 - 1.5*		cm
$L_{ucut}^{(2)}$	5.0 - 6.0*		cm

*: *First number refers to first cavity of S-IH-DTL; Second number refers to last cavity of S-IH-DTL*
**: *First number refers to S-IH-DTL with doublets; Second number refers to S-IH-DTL with triplets*

The undercut window increases from cavity to cavity of the S-IH-DTL structure, ensuring uniform axial electric fields. For visualization purposes, the axial electric fields in the first and last tanks of the S-IH-DTL are illustrated in Figure 5.6.



(a)



(b)

Figure 5.6: Axial electric field in (a) first and (b) last S-IH-DTL cavities for carbon ion acceleration from 0.7 MeV/u to 5 MeV/u, simulated with CST Studio Suite.

The S-IH-DTL with quadrupole doublets contains a total of 52 PMQs, while the version with quadrupole triplets contains 78 PMQs. Both versions of the S-IH-DTL are designed to use samarium cobalt permanent magnets, limiting the magnetic induction to 1 T at the pole tip, which must not be exceeded at any time. Since the bore radius of the S-IH-DTL is 8 mm in both cases, the maximum allowable gradient strength is 125 T/m. A transverse phase advance of 56° for S-IH-DTL with doublets, and 60° for S-IH-DTL with triplets, has been chosen as a compromise between beam excursions and quadrupole gradient strength. The length and gradient strength of each PMQ in the S-IH-DTL with quadrupole doublets and triplets are summarized in Table 5.5 and Table 5.6, respectively.

Table 5.5: PMQ parameters of the S-IH-DTL with quadrupole doublets for carbon ion acceleration from 0.7 MeV/u to 5 MeV/u

No.	Grad. Str. [T/m]	Length [mm]	·	No.	Grad. Str. [T/m]	Length [mm]
1.	120.79 -118.83	50 50	·	**14.**	120.76 -119.66	50 50
2.	121.21 -119.32	50 50	·	**15.**	118.23 -117.39	50 50
3.	121.47 -119.68	50 50	·	**16.**	119.85 -118.84	50 50
4.	121.67 -119.94	50 50	·	**17.**	119.24 -118.27	50 50
5.	121.94 -120.28	50 50	·	**18.**	118.54 -117.62	50 50
6.	122.13 -120.54	50 50	·	**19.**	117.78 -116.91	50 50
7.	122.08 -120.57	50 50	·	**20.**	116.96 -116.12	50 50
8.	122.15 -120.71	50 50	·	**21.**	116.09 -115.29	50 50
9.	122.09 -120.72	50 50	·	**22.**	115.12 -114.35	50 50
10.	121.95 -120.62	50 50	·	**23.**	114.13 -113.39	50 50
11.	121.76 -120.51	50 50	·	**24.**	113.06 -112.36	50 50
12.	121.54 -120.33	50 50	·	**25.**	111.93 -111.26	50 50
13.	121.18 -120.02	50 50	·	**26.**	112.75 -112.11	50 50

Table 5.6: PMQ parameters of the S-IH-DTL with quadrupole triplets for carbon ion acceleration from 0.7 MeV/u to 5 MeV/u

No.	Grad. Str. [T/m]	Length [mm]	·	No.	Grad. Str. [T/m]	Length [mm]
	93.68	40			108.82	40
1.	-85.24	80	·	**14.**	-103.76	80
	93.68	40			108.82	40
	95.38	40			109.31	40
2.	-87.29	80	·	**15.**	-104.46	80
	95.38	40			109.31	40
	96.99	40			109.69	40
3.	-89.22	80	·	**16.**	-105.05	80
	96.99	40			109.69	40
	98.53	40			109.98	40
4.	-91.05	80	·	**17.**	-105.53	80
	98.53	40			109.98	40
	99.98	40			110.17	40
5.	-92.79	80	·	**18.**	-105.91	80
	99.98	40			110.17	40
	101.35	40			110.26	40
6.	-94.43	80	·	**19.**	-106.19	80
	101.35	40			110.26	40
	102.61	40			110.24	40
7.	95.94	80	·	**20.**	-106.37	80
	102.61	40			110.24	40
	103.78	40			110.15	40
8.	-97.38	80	·	**21.**	-106.46	80
	103.78	40			110.15	40
	105.29	40			109.94	40
9.	-99.13	80	·	**22.**	-106.42	80
	105.29	40			109.94	40
	105.83	40			109.65	40
10.	-99.91	80	·	**23.**	-106.31	80
	105.83	40			109.65	40
	106.76	40			109.26	40
11.	-101.04	80	·	**24.**	-106.09	80
	106.76	40			109.26	40
	107.55	40			108.78	40
12.	-102.06	80	·	**25.**	-105.78	80
	107.55	40			108.78	40
	108.23	40			110.27	40
13.	-102.96	80	·	**26.**	-107.29	80
	108.23	40			110.27	40

After a thorough analysis of beam dynamics within the S-IH-DTL, the key parameters for both designs were obtained and summarized in Table 5.7.

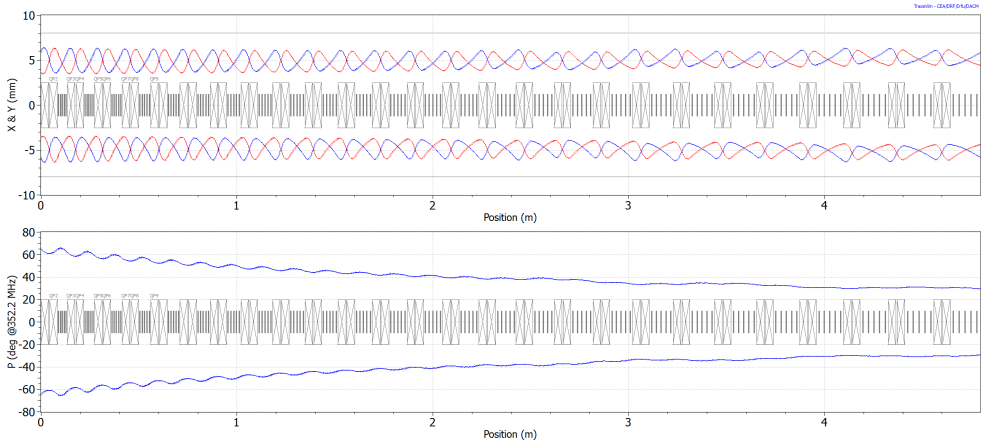
Table 5.7: Beam parameters of the S-IH-DTL for carbon ion acceleration from 0.7 MeV/u to 5 MeV/u

	C-ions		**He-ions**		**Units**
	Doublets	**Triplets**	**Doublets**	**Triplets**	
Bore radius	8				mm
Max. grad. str.	125				T/m
Input tran. norm. emittance (rms)(xx')	0.250	0.250	0.300	0.300	π.mm.mrad
Input tran. norm. emittance (rms)(yy')	0.250	0.250	0.300	0.300	π.mm.mrad
Output tran. norm. emittance (rms)(xx')	0.261	0.263	0.312	0.312	π.mm.mrad
Output tran. norm. emittance (rms)(yy')	0.262	0.261	0.311	0.319	π.mm.mrad
Input long. norm. emittance (rms)	1.191	1.191	0.473	0.473	π.deg.MeV
Output long. norm. emittance (rms)	1.230	1.228	0.486	0.497	π.deg.MeV
Energy spread (for 2σ (95% beam))	$\pm$1.02	$\pm$0.93	$\pm$1.31	$\pm$1.22	%
α_x (at output)	-1.575	-0.298	-1.655	-0.366	-
β_x (at output)	0.672	0.547	0.434	0.408	mm/π.mrad
α_y (at output)	0.632	-0.305	0.273	-0.483	-
β_y (at output)	0.392	0.441	0.168	0.239	mm/π.mrad
Transmission	100	100	100	100	%

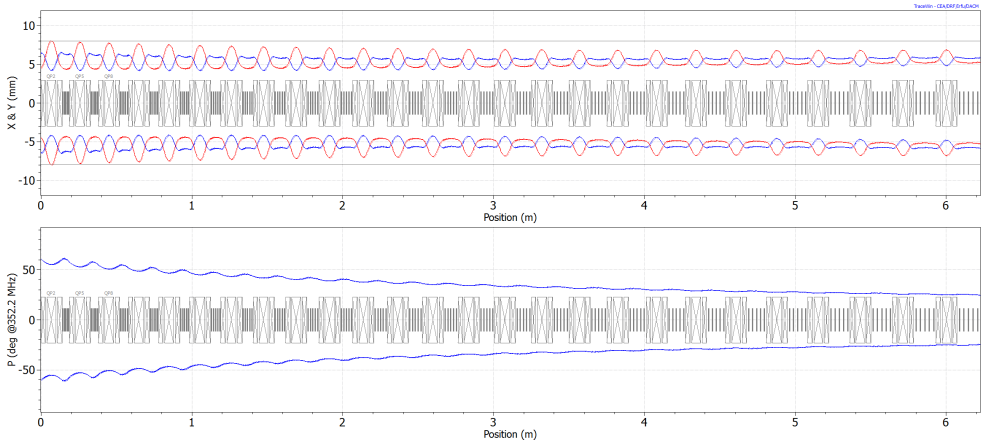
The bore radius for all configurations is fixed at 8 mm, ensuring 100% beam transmission. The transverse normalized rms emittance growth in the horizontal plane is 4.4%, while the increase of 4.8% is observed in the vertical plane, and a rise of 3.3% is noted in the longitudinal plane when carbon ions are accelerated with the S-IH-DTL using doublets. When triplets are used, the carbon ions show a normalized rms emittance growth of 5.2% in the horizontal plane, a 4.4% increase in the vertical plane, and a 3.1% growth in the longitudinal plane.

Regarding the acceleration of helium ions with the S-IH-DTL using doublets, the normalized rms emittance growth of 4% is observed in the horizontal plane, while in the vertical and longitudinal planes, the growths of 3.7% and 2.7% are recorded, respectively. For the S-IH-DTL with triplets, the normalized rms emittance growths are similar, resulting in 4% in the horizontal

plane, 6.3% in the vertical plane, and 5.1% in the longitudinal plane.



(a)

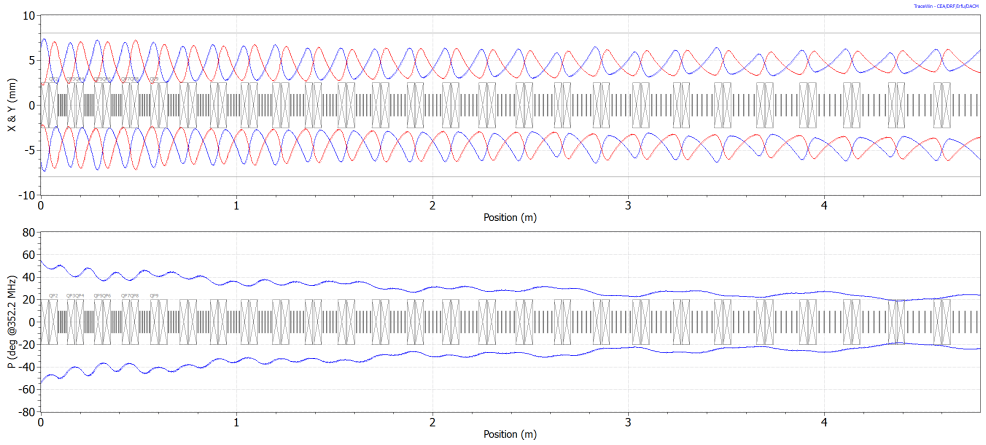


(b)

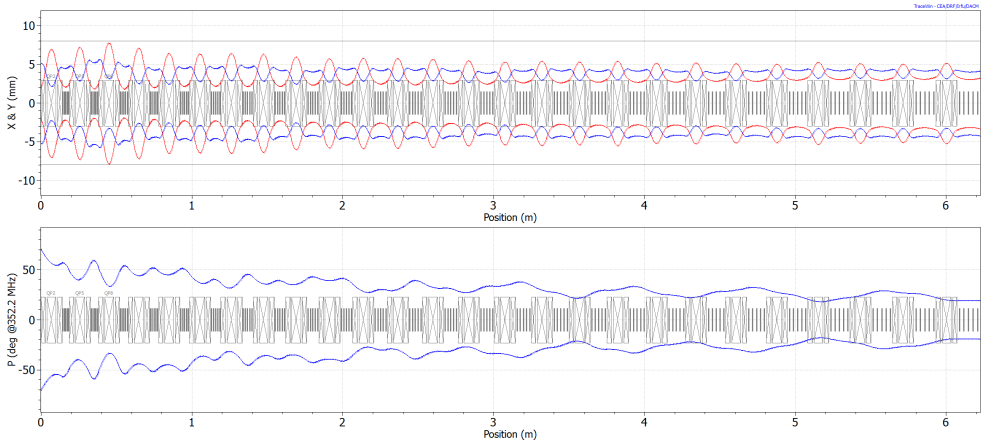
Figure 5.7: Beam envelopes along the (a) S-IH-DTL with doublets and (b) S-IH-DTL with triplets from 0.7 MeV/u to 5 MeV/u for carbon ions. For each structure, the top plot represents transverse beam envelopes in the xz and yz planes, while the bottom plot shows the phase envelope.

The energy spread (for 2σ, or 95% of the beam) for carbon ions is $\pm 1.02\%$ for doublets and $\pm 0.93\%$ for triplets, while for helium ions, it is slightly higher at $\pm 1.31\%$ for doublets and $\pm 1.22\%$ for triplets.

At a nominal beam current of 0.6 mA, the transverse and longitudinal beam envelopes for carbon ions within the S-IH-DTL using quadrupole doublets and triplets are shown in Figure 5.7, while Figure 5.8 illustrates the corresponding transverse and longitudinal envelopes for helium ions accelerated with the same structure, utilizing quadrupole doublets and triplets.



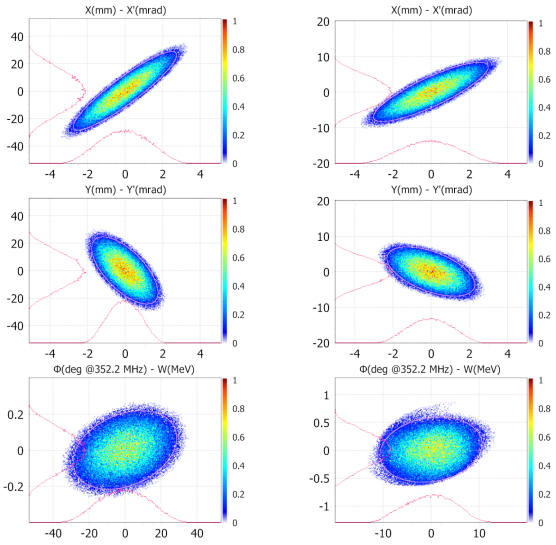
(a)



(b)

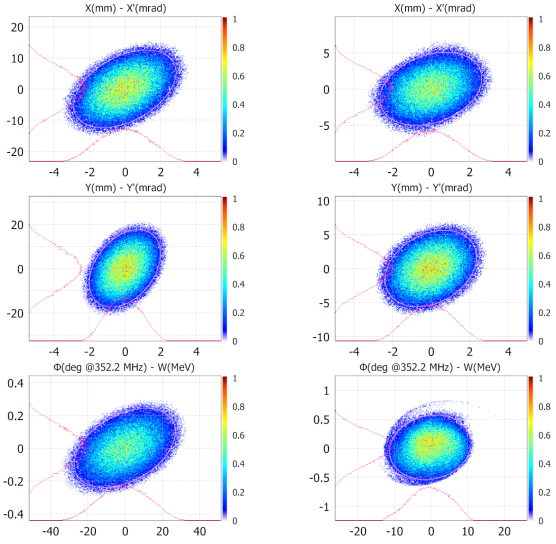
Figure 5.8: Beam envelopes along the (a) S-IH-DTL with doublets and (b) S-IH-DTL with triplets from 0.7 MeV/u to 5 MeV/u for helium ions. For each structure, the top plot represents transverse beam envelopes in the xz and yz planes, while the bottom plot shows the phase envelope.

The phase space for carbon ions at the input and output of the S-IH-DTL with doublets are shown in Figure 5.9, while Figure 5.10 presents the phase spaces for carbon ions at the input and output of the S-IH-DTL with triplets.



(a) **(b)**

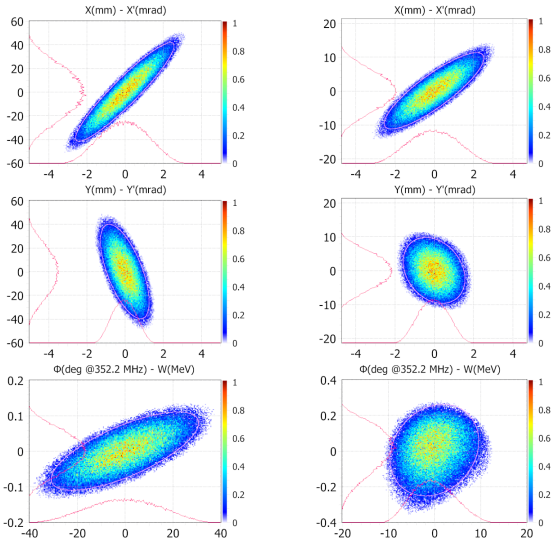
Figure 5.9: Carbon ion phase space (left column) at 0.7 MeV/u and (right column) at 5 MeV/u with the nominal beam current of 0.6 mA within S-IH-DTL with quadrupole doublets.



(a) **(b)**

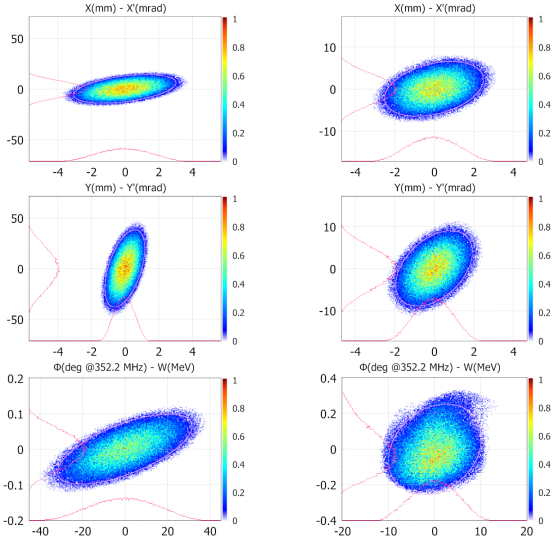
Figure 5.10: Carbon ion phase space (left column) at 0.7 MeV/u and (right column) at 5 MeV/u with the nominal beam current of 0.6 mA within S-IH-DTL with quadrupole triplets.

On the other hand, the phase spaces for helium ions at the entrance and exit of the S-IH-DTL with doublets are shown in Figure 5.11, while Figure 5.12 illustrates the phase spaces for the same particles at the same energies but for the S-IH-DTL with triplets.



(a) **(b)**

Figure 5.11: Helium ion phase space (left column) at 0.7 MeV/u and (right column) at 5 MeV/u with the nominal beam current of 5 mA within S-IH-DTL with quadrupole doublets.



(a) **(b)**

Figure 5.12: Helium ion phase space (left column) at 0.7 MeV/u and (right column) at 5 MeV/u with the nominal beam current of 5 mA within S-IH-DTL with quadrupole triplets.

5.1.3 Alvarez Drift Tube Linac for radioisotope production

To extend the acceleration of helium ions up to 10 MeV/u in the HITRI*plus* design, the first section is followed by two separate Drift Tube Linacs (DTL cavities) that are powered only when radioisotopes are produced. When the beam is injected into the synchrotron, both DTL cavities are off. The design uses two DTL structures instead of one to allow for the radioisotope production with helium ions at two different energies. When the first DTL is in operation and the second is off, the helium ions reach an energy of 7.1 MeV/u, the optimal value for producing one of the most promising alpha-emitting radioisotopes for cancer treatment, 211-Astatine [49]. In the case where both DTL structures are in operation, the helium ions are accelerated to an energy of 10 MeV/u and then used for the production of commonly demanded radioisotopes, such as 18-Fluorine, the most widely used radiotracer in PET (Positron Emission Tomography) imaging for early detection of tumors [111]. The RF design of both DTLs was carried out with the Poisson/SUPERFISH codes, while the beam dynamics were simulated using TraceWin.

The first DTL, referred to as DTL1, is responsible for accelerating helium ions from 5 MeV/u to 7.1 MeV/u. The second DTL, denoted as DTL2, takes over and further accelerates the helium ions from 7.1 MeV/u up to 10 MeV/u. Electric field distributions inside both DTL1 and DTL2, computed with the Poisson/SUPERFISH codes, are shown in Figure 5.13.

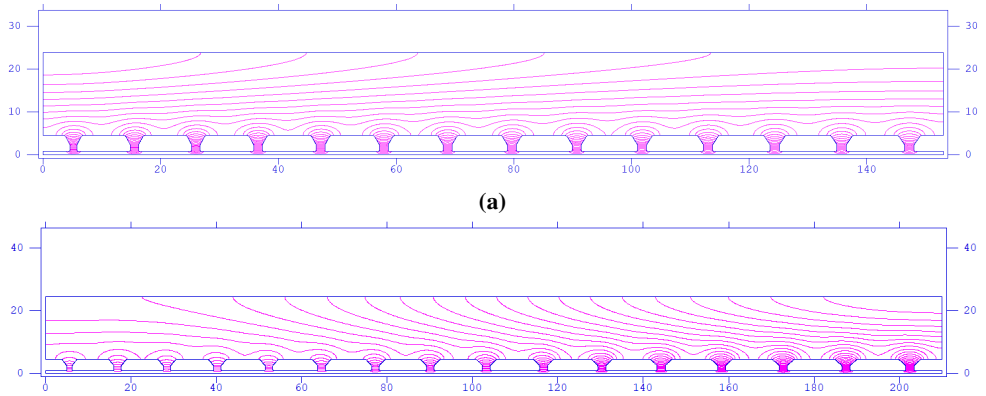


Figure 5.13: Electric field distribution in (a) DTL1, and (b) DTL2, for acceleration of 5 mA helium ions from (a) 5 MeV/u to 7.1 MeV/u, and (b) 7.1 MeV/u to 10 MeV/u, respectively, simulated with Poisson/SUPERFISH codes.

The RF and geometry parameters for DTL1 and DTL2, designed for the acceleration of helium ions from 5 MeV/u to 10 MeV/u, are summarized in Table 5.8. Both structures operate at a frequency of 352.2 MHz, with a 10% RF duty cycle. The peak beam current is 5 mA for both DTL1 and DTL2, and the accelerated field is 3.1 MV/m. The synchronous phase is set to -24 ° for both structures.

In terms of physical dimensions, DTL1 has a length of 1.53 meters and a cavity radius of 23.8 cm, while DTL2 has a length of 2.09 meters and a slightly larger cavity radius of 24.5 cm.

The total RF power dissipation for DTL1 is 181 kW, while for DTL2 it is 253 kW. Both DTL1 and DTL2 exhibit high effective shunt impedance, with values of 66.77 MΩ/m and 67.53 MΩ/m, respectively.

Table 5.8: RF and geometry parameters of the DTL1 and DTL2 for acceleration of 5 mA helium ions from 5 MeV/u to 10 MeV/u

	DTL1	**DTL2**	**Units**
Operating frequency	352.2		MHz
Input energy	20	28.4	MeV
Output energy	28.4	40	MeV
RF duty cycle	10		%
Peak beam current	5		mA
Accelerated field	3.1		MV/m
Maximal surface field	1.3		kp
Synchronous phase	-24		deg
Length	1.53	2.09	m
Cavity radius	23.8	24.5	cm
Total RF power	202	282	kW
No. of cells	14	16	-
Effective shunt impedance	66.77	67.53	MΩ/m
Nominal tank voltage	4.3	6.0	MV
Power dissipation	181	253	kW
Beam power	21	29	kW

The DTL1 contains 14 PMQs, while the DTL2 has 16 PMQs. Since the bore radius of both DTL1 and DTL2 is 7.5 mm, the maximal allowed gradient strength is 133.3 T/m. A transverse phase advance of 50° for both DTL1 and DTL2, has been chosen as a compromise between beam excursions and quadrupole gradient strength. The length and gradient strength of each PMQ within the DTL1 and DTL2 are collected in Table 5.9 and Table 5.10, respectively.

Table 5.9: PMQ parameters of the DTL1 for acceleration of 5 mA helium ions from 5 MeV/u to 7.1 MeV/u

No.	Grad. Str. [T/m]	Length [mm]	·	No.	Grad. Str. [T/m]	Length [mm]
1.	118.81	40	·	**8.**	-110.63	40
2.	-118.81	40	·	**9.**	107.94	40
3.	116.06	40	·	**10.**	-107.94	40
4.	-116.06	40	·	**11.**	105.31	40
5.	113.34	40	·	**12.**	-105.31	40
6.	-113.35	40	·	**13.**	102.66	40
7.	110.63	40	·	**14.**	-102.66	40

Table 5.10: PMQ parameters of the DTL2 for acceleration of 5 mA helium ions from 7.1 MeV/u to 10 MeV/u

No.	Grad. Str. [T/m]	Length [mm]	·	No.	Grad. Str. [T/m]	Length [mm]
1.	84.26	50	·	**9.**	80.45	50
2.	-84.26	50	·	**10.**	-80.45	50
3.	83.82	50	·	**11.**	77.97	50
4.	-83.31	50	·	**12.**	-77.97	50
5.	83.38	50	·	**13.**	75.52	50
6.	-83.38	50	·	**14.**	-75.52	50
7.	82.96	50	·	**15.**	75.28	50
8.	-82.96	50	·	**16.**	-75.27	50

The beam parameters for DTL1 and DTL2, designed to accelerate 5 mA helium ions from 5 MeV/u to 7.1 MeV/u and from 7.1 MeV/u to 10 MeV/u, respectively, are summarized in Table 5.11. Both structures maintain a bore radius of 7.5 mm, ensuring beam acceleration without any losses. The normalized rms transverse emittances remain unchanged throughout acceleration in both DTL1 and DTL2, with values of 0.317 π.mm.mrad in the horizontal plane and 0.351 π.mm.mrad in the vertical plane at both the entrance and exit of each linac structure.

In the longitudinal plane, a slight normalized rms emittance growth is observed. In DTL1, the normalized rms longitudinal emittance increases from 0.613 π.deg.MeV (at the input) to 0.629 π.deg.MeV (at the output), corresponding to a normalized rms emittance growth of 2.6%. Similarly, in DTL2, the normalized rms emittance increases from 0.629 π.deg.MeV to 0.633 π.deg.MeV, resulting in a smaller normalized rms emittance growth of 0.6%. The energy spread (for 2σ, or 95% of the beam) at the exit of DTL1 is $\pm$1.12%, while at the exit of DTL2, it

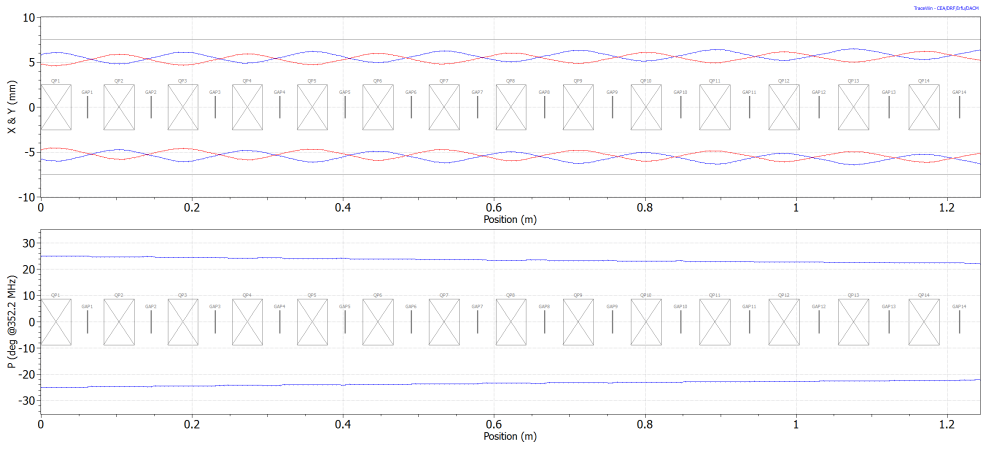
is $\pm$0.89%.

Table 5.11: Beam parameters of the DTL1 and DTL2 for acceleration of 5 mA helium ions from 5 MeV/u to 10 MeV/u

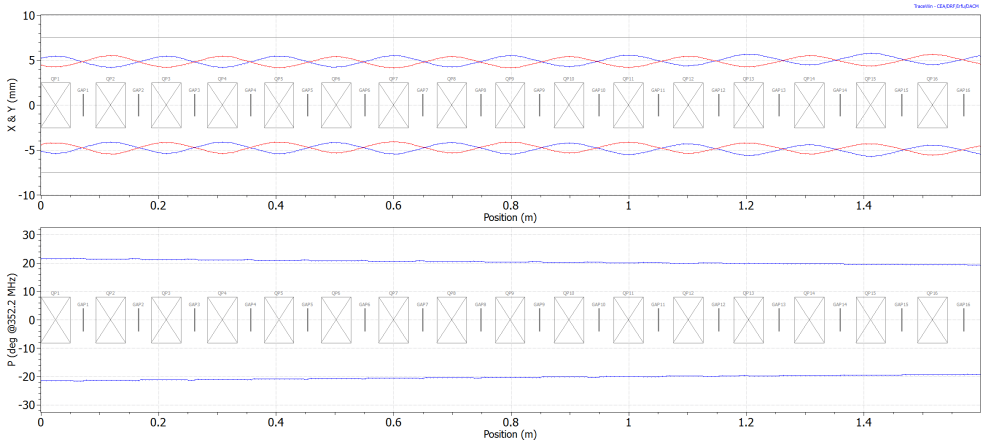
	DTL1	**DTL2**	**Units**
Bore radius	7.5		mm
Max. grad. str.	133.3		T/m
Input tran. norm. emittance (rms)(xx')	0.317	0.317	π.mm.mrad
Input tran. norm. emittance (rms)(yy')	0.351	0.351	π.mm.mrad
Output tran. norm. emittance (rms)(xx')	0.317	0.317	π.mm.mrad
Output tran. norm. emittance (rms)(yy')	0.351	0.351	π.mm.mrad
Input long. norm. emittance (rms)	0.613	0.629	π.deg.MeV
Output long. norm. emittance (rms)	0.629	0.633	π.deg.MeV
Energy spread (for 2σ (95% beam))	$\pm$1.12	$\pm$0.89	%
α_x (at output)	-1.722	-1.766	-
β_x (at output)	0.587	0.355	mm/π.mrad
α_y (at output)	1.188	1.003	-
β_y (at output)	0.426	0.194	mm/π.mrad
Transmission	100	100	%

Figure 5.14 illustrates the transverse and longitudinal beam envelopes as helium ions travel through DTL1 and DTL2. The envelopes are shown from the entrance of DTL1 at 5 MeV/u to its exit at 7.1 MeV/u, and from the entrance of DTL2 at 7.1 MeV/u to its exit at 10 MeV/u, with a nominal beam current of 5 mA.

Meanwhile, the phase spaces of 10^5 helium ions in both transverse and longitudinal planes at the input and output energies of DTL1 are presented in Figure 5.15, while those at the entrance and exit of DTL2 are shown in Figure 5.16.

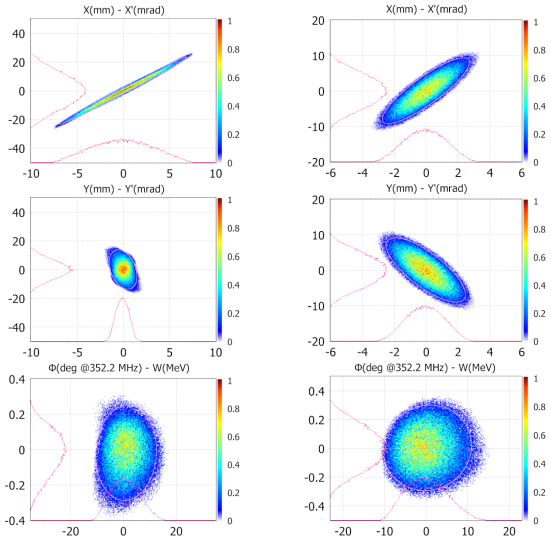


(a)



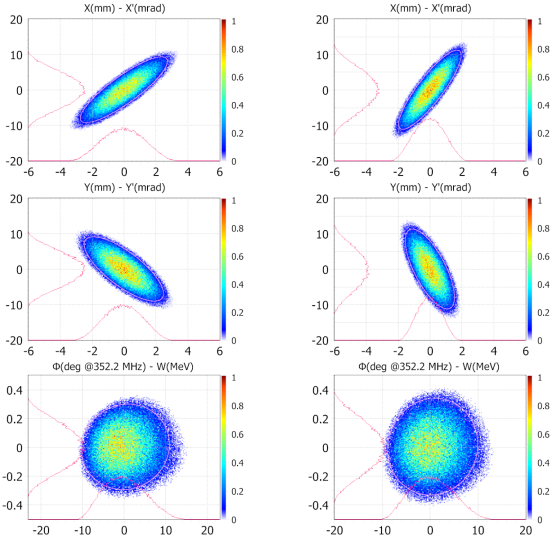
(b)

Figure 5.14: Beam envelopes along the (a) DTL1 from 5 MeV/u to 7.1 MeV/u and (b) DTL2 from 7.1 MeV/u to 10 MeV/u for helium ions. For each structure, the top plot represents transverse beam envelopes in the xz and yz planes, while the bottom plot shows the phase envelope.



(a) **(b)**

Figure 5.15: Helium ion phase space (left column) at 5 MeV/u and (right column) at 7.1 MeV/u with the nominal beam current of 5 mA within DTL1.



(a) **(b)**

Figure 5.16: Helium ion phase space (left column) at 7.1 MeV/u and (right column) at 10 MeV/u with the nominal beam current of 5 mA within DTL2.

5.1.4 Debunching cavity before injection into carbon synchrotron

To minimize the beam energy spread prior to its injection into the therapy synchrotron, an additional cavity, known as the debunching cavity (DEB), is required. Since the debunching cavity is a bunch rotator like the bunching cavity, the buncher of LINAC4 at CERN has been used as a reference, as it operates at a similar energy as the QA-DTL, namely 3 MeV. The LINAC4's bunching cavity is used in combination with focusing elements for beam matching from the RFQ to the DTL [2]. Rather than designing a completely new DEB from scratch, the LINAC4 buncher has been adapted to meet the specific requirements of this project.

The optimal position for the DEB is between DTL1 and DTL2. The EM simulations were performed using the Poisson/SUPERFISH codes, and the resulting electric field distribution is presented in Figure 5.17.

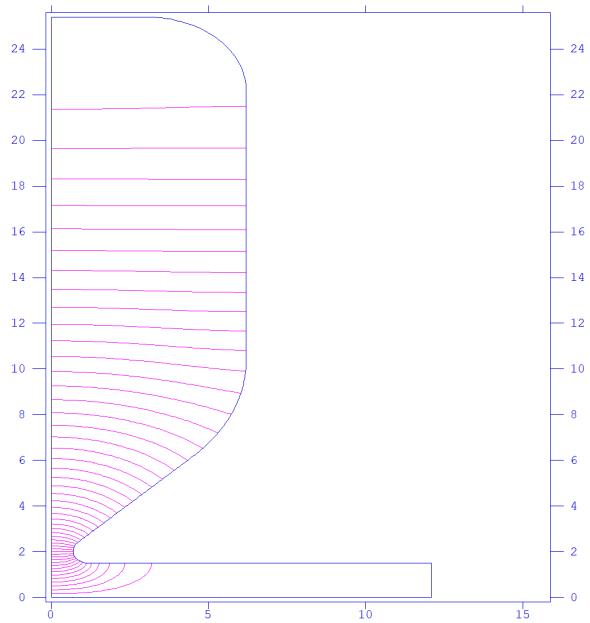


Figure 5.17: Electric field distribution in DEB used for reducing energy spread of carbon ions before injection into therapy synchrotron, simulated with Poisson/SUPERFISH codes.

The DEB consists of a single cell with a bore radius of 15 mm and an inner cavity radius of 254 mm. Its total length is 242 mm, ensuring compact integration into the beamline between DTL1 and DTL2. To minimize the energy spread, a voltage of 130 kV is required, corresponding to an accelerating field of 0.765 MV/m. The maximal surface field does not exceed 0.9 Kp, preventing the risk of electric breakdowns. The synchronous phase is set to -90° to avoid beam acceleration. Additionally, the structure features an effective shunt impedance per unit length of 8.14 MΩ/m and requires 17 kW for proper operation. These parameters are summarized in Table 5.12.

Table 5.12: RF and geometry parameters of DEB used for reducing energy spread of carbon ions before injection into therapy synchrotron

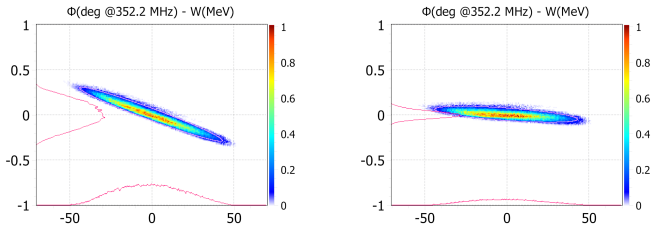
	DEB	Units
No. of cells	1	-
Bore radius	15	mm
Cavity radius	254	mm
Length	242	mm
Accelerated field	0.765	MV/m
Maximal surface field	0.9	kp
Synchronous phase	-90	deg
Effective shunt impedance	8.14	MΩ/m
Nominal tank voltage	130	kV
Power dissipation	17	kW

To assess the impact on beam quality, the energy spread of 95% of the beam and the normalized rms longitudinal emittances at both the entrance and exit of the DEB were computed using TraceWin. These values are provided in Table 5.13.

Table 5.13: Beam parameters of DEB used for reducing energy spread of carbon ions before injection into therapy synchrotron

	DEB	Units
Input long. norm. emittance (rms)	1.399	π.deg.MeV
Output long. norm. emittance (rms)	1.403	π.deg.MeV
Input energy spread (for 2σ (95% beam))	$\pm$1.62	%
Output energy spread (for 2σ (95% beam))	$\pm$0.38	%

Given the specific function of the DEB, the longitudinal phase space is the primary area of interest. Therefore, only the longitudinal phase space at both the entrance and exit of the DEB, corresponding to the data in Table 5.13, is shown in Figure 5.18.



(a) **(b)**

Figure 5.18: Carbon ion phase space (left column) before and (right column) after DEB.

5.1.5 Comparison and choice of the ideal linac configuration

In the previous section, various linac structures were examined. As mentioned, the HITRI*plus* linac is composed of three sections, each designed to accelerate particles in a different energy range. Three options have been considered for the first linac section: QA-DTL, S-IH-DTL with doublets, and S-IH-DTL with triplets. The remaining two sections consist of two DTL structures.

The QA-DTL is 15.7% shorter than the S-IH-DTL with quadrupole doublets and 43.1% shorter than the S-IH-DTL with triplet lenses, while the power dissipation is practically the same between the QA-DTL and the S-IH-DTL structures. Additionally, for QA-DTL design the normalized rms emittance growth in the transverse plane is 11.2% and 2.02% in the longitudinal plane. In the case of the S-IH-DTL designs with doublets and triplets the transverse normalized rms emittance growths are 4.8% and 4.4%, while the longitudinal normalized rms emittance growths are 3.3% and 3.1%, respectively. Since the S-IH-DTL is composed of 26 cavities with the power dissipation from 20.4 to 26.6 kW, they cannot use a klystron as the RF source, but instead have to use Solid State Amplifiers (SSAs), which will significantly increase the RF system's cost. Additionally, S-IH-DTL with doublets requires 52 quadrupoles and S-IH-DTL with triplets requires 78 quadrupoles, while QA-DTL needs only 22 quadrupole magnets, which will further increase the cost of S-IH-DTL compared to QA-DTL. The parameters of each designed linac structure are shown in Table 5.14.

Table 5.14: Comparison between QA-DTL and S-IH-DTL for carbon ion acceleration

	Power diss. [kW]	**Power source**	**Length [m]**	**Norm. trans. / long. rms emit. growth [%]**
QA-DTL	626	klystron	5.1	11.2 / 2.02
S-IH-DTL (doublets)	614	SSA	5.9	4.8 / 3.3
S-IH-DTL (triplets)	614	SSA	7.3	4.4 / 3.1

Since the QA-DTL requires less space than both variants of the S-IH-DTL, requires practically the same power with a more cost-efficient RF source (klystrons over SSAs), and requires

fewer quadrupole magnets than both S-IH-DTL with doublets and with triplets, the QA-DTL was selected as the preferred linac structure over the S-IH-DTL.

A detailed study of the IH-DTL operating at 217 MHz has been reported in [110]. Due to the absence of quadrupoles within drift tubes and since it is a π-mode structure, the IH-DTL is 35.1% shorter (corresponding to 1.8 meters) and has almost half the power dissipation (45.7% lower losses) compared to the proposed QA-DTL. However, despite its lower power dissipation and shorter length, the IH-DTL has some disadvantages compared to the QA-DTL. As mentioned in Subsection 5.1.2, the IH-DTL operates effectively at frequencies below 300 MHz, which excludes the possibility of using klystrons as the RF source, restricting it to the use of SSAs [112]. According to [112], for applications requiring frequencies between 300 MHz and 1 GHz, klystrons are significantly more power efficient than SSAs. As a result, the use of klystrons can significantly reduce the RF system's cost, making the QA-DTL comparable to the IH-DTL in terms of the overall cost of the RF system. At the exit of the IH-DTL, the longitudinal normalized rms emittance growth of 25.7% has been reported [110], while in the case of the QA-DTL, it is only 2.02%, which demonstrates the strong longitudinal beam control of the QA-DTL over the IH-DTL. On the other hand, the transverse normalized rms emittance growth is comparable for both structures. An overview of parameters concerning the QA-DTL and IH-DTL is shown in Table 5.15.

Table 5.15: Comparison between QA-DTL and IH-DTL for carbon ion acceleration

	Power diss. [kW]	**Power source**	**Length [m]**	**Norm. trans. / long. rms emit. growth [%]**
QA-DTL	626	klystron	5.1	11.2 / 2.02
IH-DTL	340	SSA	3.31	10.0 / 25.7

Following the first section, the second and third sections accelerate helium ions from 5 MeV/u to 10 MeV/u. In this thesis, two DTL structures have been chosen for these sections and compared with the IH-DTL structures designed for the same energy range, as presented in [110]. The IH-DTL in the second section has a power dissipation of 265 kW, while the IH-DTL in the third section has a power dissipation of 425 kW. Referring to Table 5.8, the DTL1 designed for the second section has a power dissipation of 181 kW, which is 31.7% lower than the IH-DTL for the same energy range, while DTL2 for the third section dissipates 253 kW, representing a 40.5% reduction compared to the IH-DTL. The length of both designs remains comparable. While at very low energies, IH-DTL shows significantly lower power losses than QA-DTL in the first section, at higher energies the power dissipation of IH-DTL surpasses that of DTL in both the second and third sections. In the case of normalized rms emittance growth, neither the IH-DTL nor DTL1 and DTL2 showed any significant change. Additionally, for proper operation, both as a synchrotron injector and for radioisotope production, the IH-DTL requires two debunching cavities with a total power dissipation of 20 kW, and an additional length of 4.6 m [104]. On the other hand, the Alvarez-type linac configuration presented in this thesis requires only one

debunching cavity with a similar power dissipation of 17 kW, which is positioned between DTL cavities, resulting in minimal additional space required. The power dissipation and length of each linac structure, including the estimated length of beam transport lines (BTL) between them, are shown in Table 5.16.

Table 5.16: Comparison between Alvarez-type and H-mode type linac configurations for carbon ion acceleration

	Power diss. [kW]	**Length [m]**
QA-DTL	626	5.1
DTL1 + BTL	181	1.83
DTL2 + BTL	253	2.27
DEB + BTL	17	0.54
Alvarez-type (total)	**1077**	**9.74**
IH-DTL1	340	3.31
IH-DTL2 + BTL	265	1.6
IH-DTL3 + BTL	425	2.04
DEB1 + BTL	10	1.13
DEB2 + BTL	10	3.47
H-mode type (total)	**1050**	**11.55**

In the case where the linac structure is required to operate only as a carbon injector for a synchrotron at an energy of 5 MeV/u, the IH-DTL is preferable due to its low power requirements and short length. However, for applications where the ions need to be accelerated beyond 5 MeV/u, as is the case for HITRI*plus* linac, the combination of Alvarez-type linac structures is preferable, due to their lower overall length, practically the same total power requirements with a more cost-efficient RF source solution (klystrons over SSA), and superior longitudinal beam control. Unfortunately, the combination of IH-DTL and Alvarez-type DTL within the same linac configuration is not possible due to the different beam dynamics (IH-DTL uses KONUS, while Alvarez-type DTL uses FODO beam dynamics). According to the aforementioned, the final layout proposed for HITRI*plus* linac consists of QA-DTL as the first section, followed by DTL1 and DTL2 as the second and third sections, respectively. As mentioned in Subsection 5.1.4, the DEB has been placed between the DTL1 and DTL2 cavities. The overall layout of the HITRI*plus* linac with DEB, as proposed in this thesis, is illustrated in Figure 5.19.

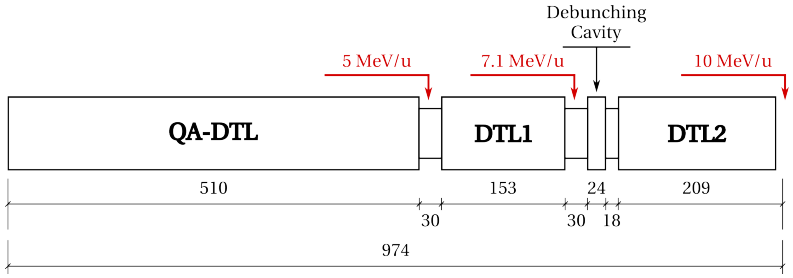


Figure 5.19: Layout of preferred HITRI*plus* linac configuration. Dimensions are given in cm.

Furthermore, the Alvarez-type linac configuration (QA-DTL for acceleration of low-velocity particles as the first section, and two DTL cavities for further acceleration as the second and third sections) has been chosen by the NIMMS study as its baseline linac, due to its superior longitudinal beam dynamics, and comparable power and length to the H-mode alternative (three IH-DTL cavities for each section).

5.2 NIMMS helium linac designs

The NIMMS helium linac is composed of three distinct linac sections, each designed to serve a specific purpose within the system. For the first accelerating stage of the NIMMS linac, two types of linac structures were considered: the QA-DTL, which operates at a frequency of 352.2 MHz, and the IH-DTL, which resonates at a frequency of 176 MHz - half that of the QA-DTL. For the second and third sections of the NIMMS linac, two DTL structures were selected to accelerate ions efficiently.

The NIMMS helium linac has to achieve the acceleration of helium ions with a nominal beam current of 5 mA before their injection into a cancer therapy synchrotron. Furthermore, in the case where the NIMMS linac is intended for radioisotope production, it must accommodate a significantly higher beam current of up to 30 mA. The linac has to be capable of accelerating deuterons with a nominal beam current of up to 30 mA, allowing for the production of a wider variety of radioisotopes, as reported in Table 2.1.

In addition to the linac structures, two RF structures for beam manipulation were designed: the Debunching Cavity (DEB) and the Energy Ramping Cavity (ERC). Although the ERC is completely optional, the DEB is a critical component of the system. Both the DEB and ERC were developed and integrated in the NIMMS linac layout.

5.2.1 Quasi-Alvarez Drift Tube Linac for helium injection into synchrotron and radioisotope production

The QA-DTL has been designed to accelerate helium ions with a nominal beam current of 5 mA up to 5 MeV/u, and inject them into the cancer therapy synchrotron. In addition to this, the QA-DTL can also accelerate deuterons or helium ions at higher currents of 30 mA, reaching the same energy of 5 MeV/u, but instead of the synchrotron, the beam is directed to the target for radioisotope production. The RF design of this QA-DTL structure was carried out using the Poisson/SUPERFISH codes, and the electric field distribution within it has been computed (see Figure 5.20).

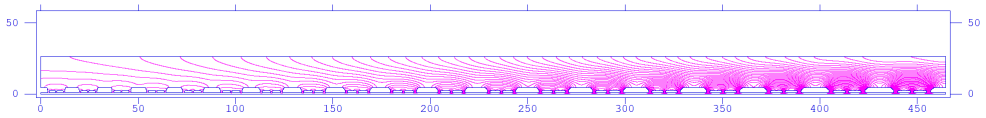


Figure 5.20: Electric field distribution in QA-DTL for helium ion acceleration from 1 MeV/u to 5 MeV/u, simulated with Poisson/SUPERFISH codes.

The QA-DTL presented in this subsection operates at a frequency of 352.2 MHz with a 10% RF duty cycle. The input energy for both helium ions and deuterons is 1 MeV/u, corresponding to a total energy of 4 MeV for helium ions and 2 MeV for deuterons.

The QA-DTL operates with an average accelerating field of 3.5 MV/m, limiting the peak surface field within the cavity at 1.8 Kp. The synchronous phase is adjusted between -35° and -24°, starting at -35° in the first super-period and increasing linearly by 1° per super-period until reaching -24°, after which it remains constant throughout the rest of the QA-DTL. The total length of the structure is 4.65 m, with a cavity radius of 26.6 cm.

The QA-DTL consists of 19 super-periods and achieves an effective shunt impedance per unit length of 60.12 MΩ/m. The power dissipation of the structure is 570 kW. The RF and geometry parameters of the QA-DTL are summarized in Table 5.17.

The bore radius of the developed QA-DTL is slightly larger compared to the linac structure designed for the HITRI*plus* project. This increase is necessary to accommodate the acceleration of higher-current beams, resulting in a bore radius of 10 mm and ensuring 100% beam transmission in all examined cases. To limit magnetic induction at the pole tip to 1 T for each of 19 PMQs, the gradient strength of 100 T/m must not be exceeded. A transverse phase advance of 68° has been chosen as a compromise between beam excursions and quadrupole gradient strength. The length and gradient strength of each PMQ within the QA-DTL are listed in Table 5.18.

Table 5.17: RF and geometry parameters of the QA-DTL for acceleration of 5mA and 30mA helium ions from 1 MeV/u to 5 MeV/u

	Synch.	Isoto.	Units
Operating frequency	352.2		MHz
Input energy	4		MeV
Output energy	20		MeV
RF duty cycle	10		%
Peak beam current	5	30	mA
Accelerated field	3.5		MV/m
Maximal surface field	1.8		kp
Synchronous phase	-35 to -24		deg
Length	4.65		m
Cavity radius	26.6		cm
Total RF power	610	810	kW
No. of super-periods	19		-
Effective shunt impedance	60.12		MΩ/m
Nominal tank voltage	12.8		MV
Power dissipation	570		kW
Beam power	40	240	kW

Table 5.18: PMQ parameters of the QA-DTL for helium ion acceleration from 1 MeV/u to 5 MeV/u

No.	Grad. Str. [T/m]	Length [mm]	·	No.	Grad. Str. [T/m]	Length [mm]
1.	70.72	60	·	**11.**	62.23	60
2.	-70.62	60	·	**12.**	-62.21	60
3.	67.29	60	·	**13.**	61.49	60
4.	-67.18	60	·	**14.**	-61.46	60
5.	65.02	60	·	**15.**	60.84	60
6.	-64.98	60	·	**16.**	-60.83	60
7.	63.99	60	·	**17.**	60.27	60
8.	-63.96	60	·	**18.**	-60.26	60
9.	63.07	60	·	**19.**	59.99	60
10.	-63.04	60	·	-	-	-

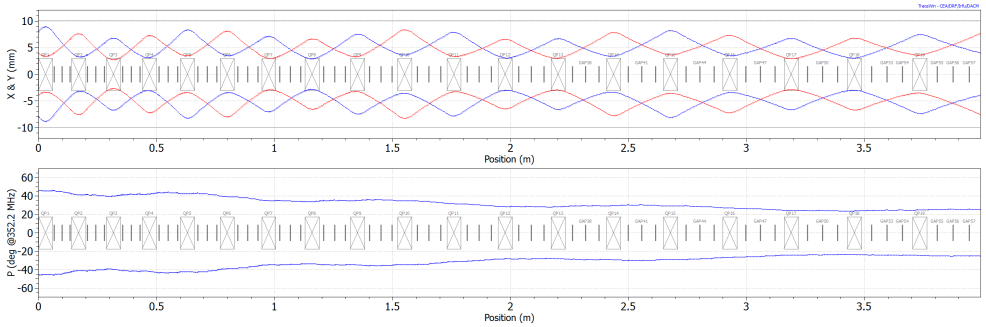
At the QA-DTL output, a slight increase in normalized rms emittance is observed. The normalized rms emittance growth in the horizontal plane reaches 2.8% for 5 mA helium ions, and 4% for 30 mA helium ions. In the vertical plane, the normalized rms emittance growth follows a similar trend, with values of 3.2%, and 6% for the same respective cases.

In the longitudinal plane, the normalized rms emittance growth for helium ions is 2.5% at a beam current of 5 mA and 6.3% at 30 mA. Despite these increases, the energy spread for 95% of the beam remains below 1% in both scenarios. The beam parameters of the QA-DTL are summarized in Table 5.19.

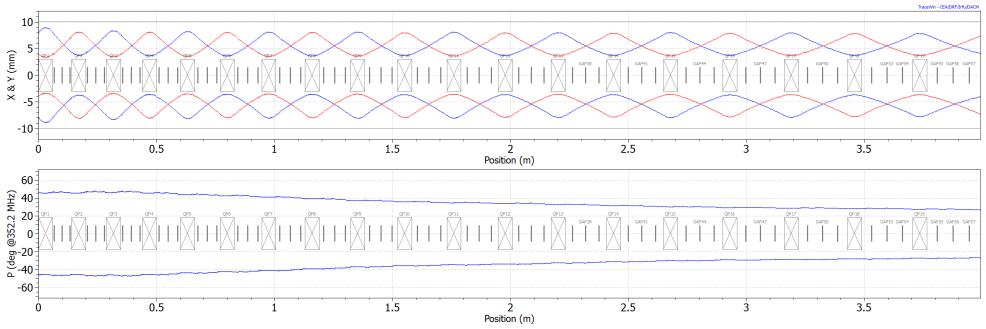
Table 5.19: Beam parameters of the QA-DTL for helium ion acceleration from 1 MeV/u to 5 MeV/u

	Synch.	**Isoto.**	**Units**
Bore radius	10		mm
Max. grad. str.	100		T/m
Input tran. norm. emittance (rms)(xx')	0.250	0.250	π.mm.mrad
Input tran. norm. emittance (rms)(yy')	0.250	0.250	π.mm.mrad
Output tran. norm. emittance (rms)(xx')	0.257	0.260	π.mm.mrad
Output tran. norm. emittance (rms)(yy')	0.258	0.265	π.mm.mrad
Input long. norm. emittance (rms)	0.394	0.394	π.deg.MeV
Output long. norm. emittance (rms)	0.404	0.419	π.deg.MeV
Energy spread (for 2σ (95% beam))	$\pm$0.97	$\pm$0.94	%
α_x (at output)	1.158	1.101	-
β_x (at output)	0.375	0.351	mm/π.mrad
α_y (at output)	-3.331	-3.867	-
β_y (at output)	1.413	1.582	mm/π.mrad
Transmission	100	100	%

The beam envelopes were computed for helium ions used for both synchrotron injection and radioisotope production. These results are illustrated in Figure 5.21.



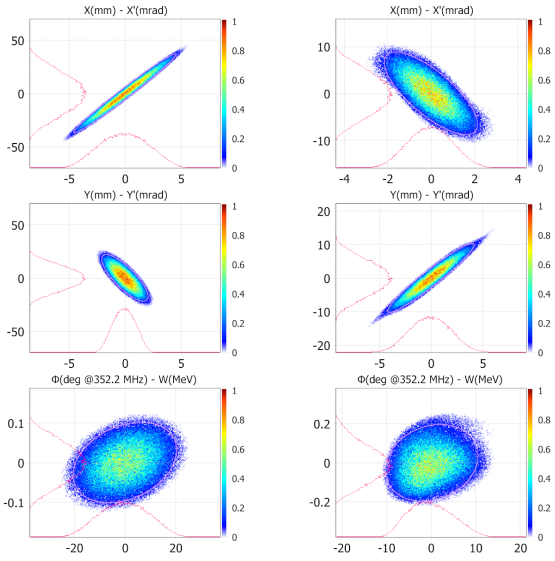
(a)



(b)

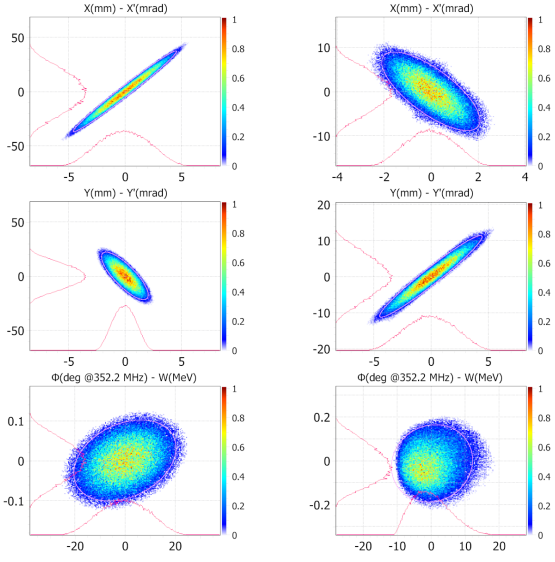
Figure 5.21: Beam envelopes along the QA-DTL from 1 MeV/u to 5 MeV/u for helium ions at (a) 5mA (beam for synchrotron) and (b) 30 mA (beam for radioisotope production) of nominal beam current. For each accelerated ion, the top plot represents transverse beam envelopes in the xz and yz planes, while the bottom plot shows the phase envelope.

The phase space plots in both transverse and longitudinal planes, at the entrance and exit of the QA-DTL, have been computed for 10^5 helium ions. These plots correspond to helium ions used for synchrotron injection at 5 mA (see Figure 5.22) and for radioisotope production at 30 mA (see Figure 5.23).



(a) **(b)**

Figure 5.22: Helium ion phase space (left column) at 1 MeV/u and (right column) at 5 MeV/u with the nominal beam current of 5 mA within QA-DTL.



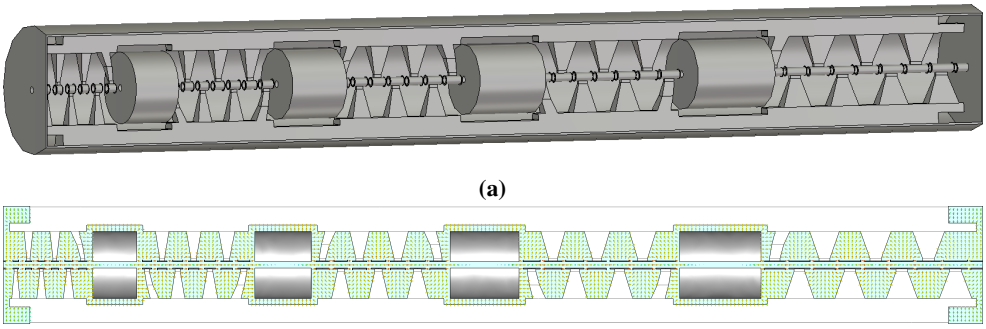
(a) **(b)**

Figure 5.23: Helium ion phase space (left column) at 1 MeV/u and (right column) at 5 MeV/u with the nominal beam current of 30 mA within QA-DTL.

5.2.2 H-mode Drift Tube Linac for helium injection into synchrotron

The IH-DTL was designed only to operate as a synchrotron injector due to the experience with the HITRI*plus* linac discussed in Subsection 5.1.5, and then compared with the QA-DTL. In other words, the IH-DTL is designed to accelerate helium ions at a nominal beam current of 5 mA. As previously mentioned, IH-DTL structures operate efficiently at frequencies below 300 MHz, leading to the choice of an operating frequency of 176 MHz - half that of the other linac structures developed in this thesis.

The electromagnetic (EM) simulations for the IH-DTL were conducted using CST Studio Suite, and its 3D model is shown in Figure 5.24a. These simulations provided insights into the electric field distribution, which is illustrated in Figure 5.24b. Additionally, the axial electric field along the IH-DTL is presented in Figure 5.25.



(a)

(b)

Figure 5.24: (a) The 3D model of IH-DTL and (b) electric field distribution in IH-DTL for helium ion acceleration from 1 MeV/u to 5 MeV/u, simulated with CST Studio Suite.

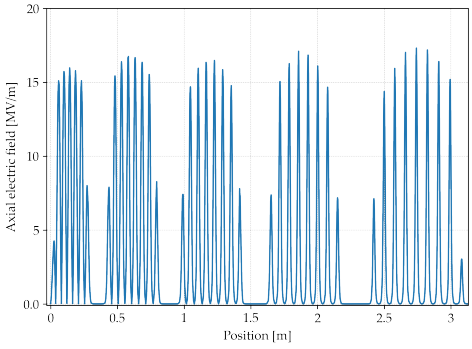


Figure 5.25: Axial electric field in IH-DTL designed for acceleration of helium ions from 1 MeV/u to 5 MeV/u, simulated with CST Studio Suite.

Using the post-processing tools within CST Studio Suite, the RF parameters were extracted and are documented in Table 5.20. Two synchronous phases are provided in Table 5.20, owing

to the two sections within the IH-DTL structure - an acceleration section and a beam rebunching section (three cells after each quadrupole) - integrated as part of the KONUS beam dynamics, as explained in Subsection 4.3.3. Besides the two synchronous phases, another distinguishing feature of the IH-DTL, compared to DTL structures, is the presence of undercuts. The dimensions of these undercuts ($L_{ucut}^{(1)}$ and $L_{ucut}^{(2)}$, as shown in Table 5.20) were optimized to achieve a uniform electric field distribution in each gap along the beam axis, as shown in Figure 5.25.

The total length of the IH-DTL is 3.12 m, with a cavity radius of 18.9 cm. The accelerating field is set to 3.5 MV/m, while the maximum surface field reaches 2.2 Kp, where the Kilpatrick level at 176 MHz is approximately 1 Kp $\approx$ 14.02 MV/m.

Table 5.20: RF and geometry parameters of the IH-DTL for helium ion acceleration from 1 MeV/u to 5 MeV/u

	IH-DTL	**Units**
Operating frequency	176	MHz
Input energy	4	MeV
Output energy	20	MeV
RF duty cycle	10	%
Peak beam current	5	mA
Accelerated field	3.5	MV/m
Maximal surface field	2.2	kp
Synchronous phase	0 / -30	deg
Length	3.12	m
Cavity radius	18.9	cm
Total RF power	342	kW
No. of cells	40	-
Effective shunt impedance	76.13	MΩ/m
Nominal tank voltage	8.08	MV
Power dissipation	302	kW
Beam power	40	kW
$L_{ucut}^{(1)}$	2 to 2.5	cm
$L_{ucut}^{(2)}$	8.5 to 10	cm

The IH-DTL has only 4 quadrupole triplets, resulting in 12 PMQs in total. For a bore radius of 10 mm the maximal allowed gradient strength is 100 T/m. A transverse phase advance of 52° has been chosen as a compromise between beam excursions and quadrupole gradient strength. The length and gradient strength of each PMQ within the IH-DTL are shown in Table 5.21.

Table 5.21: PMQ parameters of the IH-DTL for helium ion acceleration from 1 MeV/u to 5 MeV/u

No.	Grad. Str. [T/m]	Length [mm]	·	No.	Grad. Str. [T/m]	Length [mm]
1.	94.77	30	·	**3.**	51.86	50
	-89.53	60			-49.56	100
	94.77	30			51.86	50
2.	69.67	40	·	**4.**	41.04	60
	-66.38	80			-39.31	120
	69.67	40			41.04	60

Regarding the beam dynamics, all simulations were performed with 10^5 helium ions with a nominal beam current of 5 mA in TraceWin. The input transverse normalized rms emittance is set at 0.25 π.mm.mrad in both the horizontal and vertical planes. At the output, an increase in normalized rms emittance is observed, with values reaching 0.285 π.mm.mrad (corresponding to 14% normalized rms emittance growth) in the horizontal plane and 0.299 π.mm.mrad (corresponding to 19.6% normalized rms emittance growth) in the vertical plane.

On the other hand, in the longitudinal plane, the normalized rms input emittance is 0.197 π.deg.MeV, increasing to 0.238 π.deg.MeV at the output, which is 20.8% normalized rms emittance growth. The energy spread, calculated for 95% of the beam, is $\pm$0.98%. The beam parameters of the IH-DTL are summarized in Table 5.22.

Along with the parameters listed in Table 5.22, the beam envelopes were computed in TraceWin. The resulting beam envelopes for helium ions accelerated within the IH-DTL are shown in Figure 5.26.

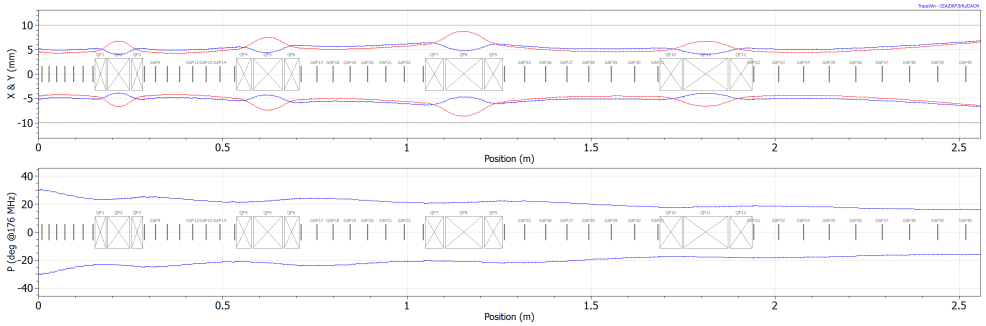


Figure 5.26: Beam envelopes along the IH-DTL from 1 MeV/u to 5 MeV/u for helium ions with 5 mA of nominal beam current. The top plot represents transverse beam envelopes in the xz and yz planes, while the bottom plot shows the phase envelope.

The beam phase space plots for helium ions at a nominal beam current of 5 mA, at the entrance and exit of the IH-DTL, were also computed with TraceWin and are presented in Figure 5.27.

Table 5.22: Beam parameters of the IH-DTL for helium ion acceleration from 1 MeV/u to 5 MeV/u

	IH-DTL	**Units**
Bore radius	10	mm
Max. grad. str.	100	T/m
Input tran. norm. emittance (rms)(xx')	0.250	π.mm.mrad
Input tran. norm. emittance (rms)(yy')	0.250	π.mm.mrad
Output tran. norm. emittance (rms)(xx')	0.285	π.mm.mrad
Output tran. norm. emittance (rms)(yy')	0.299	π.mm.mrad
Input long. norm. emittance (rms)	0.197	π.deg.MeV
Output long. norm. emittance (rms)	0.238	π.deg.MeV
Energy spread (for 2σ (95% beam))	$\pm$0.98	%
α_x (at output)	-1.212	-
β_x (at output)	0.556	mm/π.mrad
α_y (at output)	-1.288	-
β_y (at output)	0.678	mm/π.mrad
Transmission	100	%

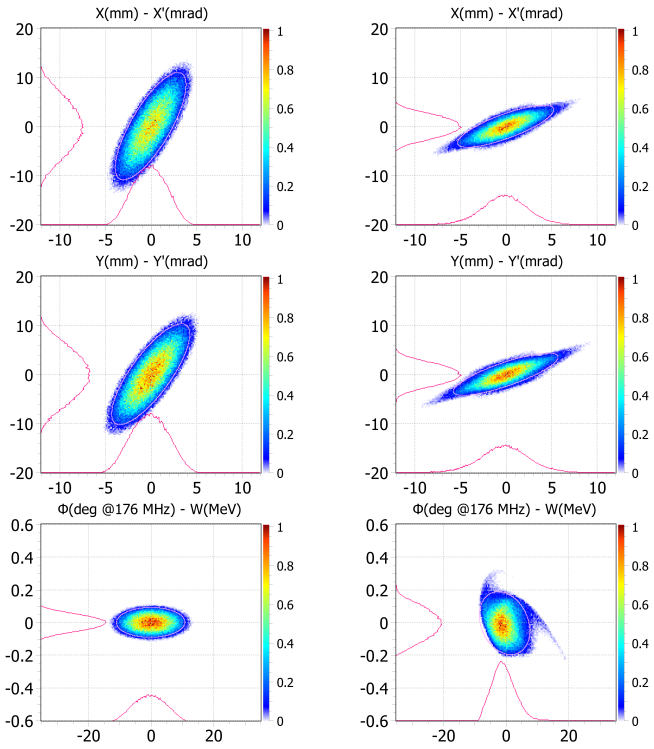


Figure 5.27: Helium ion phase space (left column) at 1 MeV/u and (right column) at 5 MeV/u with the nominal beam current of 5 mA within IH-DTL.

5.2.3 Alvarez Drift Tube Linac for radioisotope production

The QA-DTL is followed by two DTL structures, labeled DTL1 and DTL2, respectively. These structures have been designed with a unique feature: the first cell of each DTL is separated by a copper wall from the following cells. The reasoning behind this design choice is explained in Subsection 5.2.4.

The electric field distributions inside DTL1 and DTL2, when both of them are excited, have been computed using Poisson/SUPERFISH codes. The first cells of each cavity in this case operate as accelerating cells. The results of the simulation are shown in Figure 5.28.

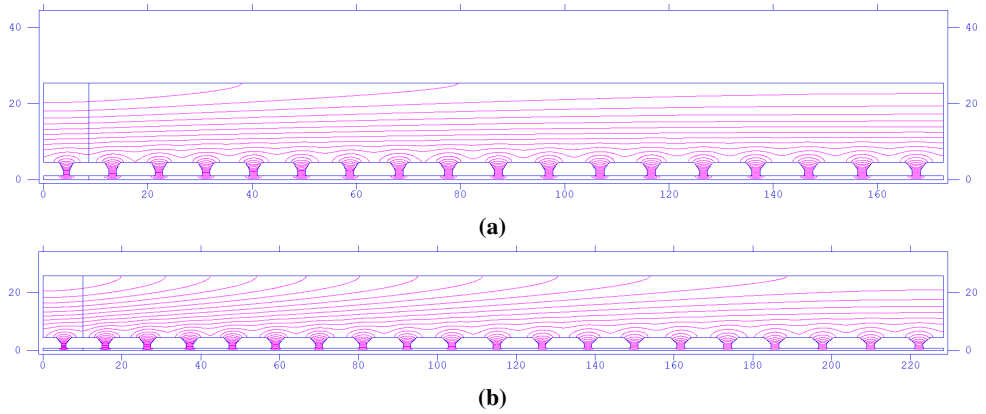


Figure 5.28: Electric field distribution in (a) DTL1, and (b) DTL2, for acceleration of 30 mA helium ions from (a) 5 MeV/u to 7.1 MeV/u, and (b) 7.1 MeV/u to 10 MeV/u, respectively, simulated with Poisson/SUPERFISH codes.

Table 5.23 summarizes the RF and geometry parameters for the acceleration of 30 mA helium ions within DTL1 and DTL2, from 5 MeV/u to 10 MeV/u. The operating frequency for both structures is 352.2 MHz, with an RF duty cycle of 10%. The accelerating field in both structures is set to 3.1 MV/m, while the synchronous phase for both DTL1 and DTL2 is constant at -24°.

DTL1 has a length of 1.74 meters and a cavity radius of 25.4 cm, while DTL2 has a length of 2.28 meters and a cavity radius of 25.8 cm. The effective shunt impedance per unit length is 56.18 MΩ/m for DTL1 and 59.14 MΩ/m for DTL2, with the power dissipation of 235 kW and 300 kW in DTL1 and DTL2, respectively.

The bore radius for both DTL1 and DTL2 is consistent, measuring 10 mm. Each PMQ within both DTL structures is constrained with a gradient strength of 100 T/m. A transverse phase advance of 46° for both DTL1 and DTL2, has been chosen as a compromise between beam excursions and quadrupole gradient strength. The length and gradient strength of each PMQ within both DTL1 and DTL2 are shown in Tables 5.24 and 5.25, respectively.

Table 5.23: RF and geometry parameters of the DTL1 and DTL2 for acceleration of 30 mA helium ions from 5 MeV/u to 10 MeV/u

	DTL1	DTL2	Units
Operating frequency	352.2		MHz
Input energy	20.0	28.4	MeV
Output energy	28.4	40.0	MeV
RF duty cycle	10		%
Peak beam current	30		mA
Accelerated field	3.1		MV/m
Maximal surface field	1.3		kp
Synchronous phase	-24		deg
Length	1.74	2.28	m
Cavity radius	25.4	25.8	cm
Total RF power	361	474	kW
No. of cells	18	20	-
Effective shunt impedance	56.18	59.14	MΩ/m
Nominal tank voltage	4.8	6.4	MV
Power dissipation	235	300	kW
Beam power	126	174	kW

Table 5.24: PMQ parameters of the DTL1 for acceleration of 30 mA helium ions from 5 MeV/u to 7.1 MeV/u

No.	Grad. Str. [T/m]	Length [mm]	·	No.	Grad. Str. [T/m]	Length [mm]
1.	90.97	50	·	**10.**	-93.95	50
2.	-90.98	50	·	**11.**	93.15	50
3.	93.32	50	·	**12.**	-93.16	50
4.	-93.33	50	·	**13.**	92.37	50
5.	95.75	50	·	**14.**	-92.38	50
6.	-95.76	50	·	**15.**	91.63	50
7.	94.82	50	·	**16.**	-91.63	50
8.	-94.83	50	·	**17.**	90.93	50
9.	93.95	50	·	**18.**	-90.94	50

Table 5.25: PMQ parameters of the DTL2 for acceleration of 30 mA helium ions from 7.1 MeV/u to 10 MeV/u

No.	Grad. Str. [T/m]	Length [mm]	·	No.	Grad. Str. [T/m]	Length [mm]
1.	89.81	50	·	**11.**	74.36	50
2.	-89.81	50	·	**12.**	-74.37	50
3.	85.95	50	·	**13.**	73.89	50
4.	-85.95	50	·	**14.**	-73.89	50
5.	82.17	50	·	**15.**	73.51	50
6.	-82.17	50	·	**16.**	-73.51	50
7.	79.51	50	·	**17.**	73.11	50
8.	-79.52	50	·	**18.**	-73.11	50
9.	76.91	50	·	**19.**	72.28	50
10.	-76.91	50	·	**20.**	-72.28	50

The input transverse normalized rms emittance in the horizontal plane is 0.259 π.mm.mrad for DTL1 and 0.266 π.mm.mrad for DTL2. Similarly, in the vertical plane, the input transverse normalized rms emittance is 0.265 π.mm.mrad for DTL1, while in DTL2, the normalized rms input emittance in the vertical plane is 0.272 π.mm.mrad.

At the output of DTL1, the transverse normalized rms emittance in the horizontal plane slightly increases, with values reaching 0.267 π.mm.mrad (corresponding to a 3.1% normalized rms emittance growth). In the vertical plane, the output normalized rms emittance of 0.271 π.mm.mrad (corresponding to a 2.3% normalized rms emittance growth) is registered in DTL1. In the case of DTL2, the normalized rms emittance at the output is the same as at the input in the horizontal plane, but in the vertical plane, the transverse normalized rms emittance is 0.275 π.mm.mrad (corresponding to a 1.1% normalized rms emittance growth).

For the longitudinal plane, the input normalized rms emittance is 0.421 π.deg.MeV in DTL1. In DTL2, the longitudinal normalized rms input emittance is 0.430 π.deg.MeV. At the output, the longitudinal rms emittance increases to 0.430 π.deg.MeV (corresponding to a 2.1% normalized rms emittance growth) in DTL1. In DTL2, the longitudinal rms emittance increases to 0.516 π.deg.MeV (corresponding to a 20% normalized rms emittance growth).

Lastly, the energy spread for 95% of the beam is $\pm$1.09% for helium ions at the output of DTL1, and $\pm$1.01% at the output of DTL2. These results are presented in Table 5.26.

The transverse and longitudinal beam envelopes of helium ions, from the entrance of DTL1 (5 MeV/u) to the exit of DTL1 (7.1 MeV/u), at a nominal beam current of 30 mA, are shown in Figure 5.29.

Table 5.26: Beam parameters of the DTL1 and DTL2 for acceleration of 30 mA helium ions from 5 MeV/u to 10 MeV/u

	DTL1	**DTL2**	**Units**
Bore radius	10		mm
Max. grad. str.	100		T/m
Input tran. norm. emittance (rms)(xx')	0.259	0.266	π.mm.mrad
Input tran. norm. emittance (rms)(yy')	0.265	0.272	π.mm.mrad
Output tran. norm. emittance (rms)(xx')	0.267	0.266	π.mm.mrad
Output tran. norm. emittance (rms)(yy')	0.271	0.275	π.mm.mrad
Input long. norm. emittance (rms)	0.421	0.430	π.deg.MeV
Output long. norm. emittance (rms)	0.430	0.516	π.deg.MeV
Energy spread (for 2σ (95% beam))	$\pm$1.09	$\pm$1.01	%
α_x (at output)	-1.677	-3.575	-
β_x (at output)	0.488	1.168	mm/π.mrad
α_y (at output)	4.561	1.517	-
β_y (at output)	1.186	0.404	mm/π.mrad
Transmission	100	100	%

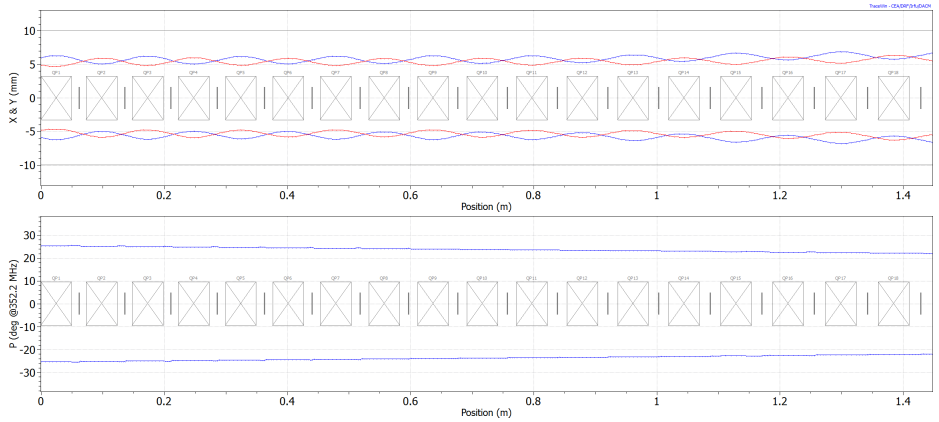


Figure 5.29: Beam envelopes along the DTL1 from 5 MeV/u to 7.1 MeV/u for helium ions at a beam current of 30 mA. The top plot represents transverse beam envelopes in the xz and yz planes, while the bottom plot shows the phase envelope.

Similarly, the beam envelopes for helium ions as they are accelerated through DTL2 have been calculated and are illustrated in Figure 5.30.

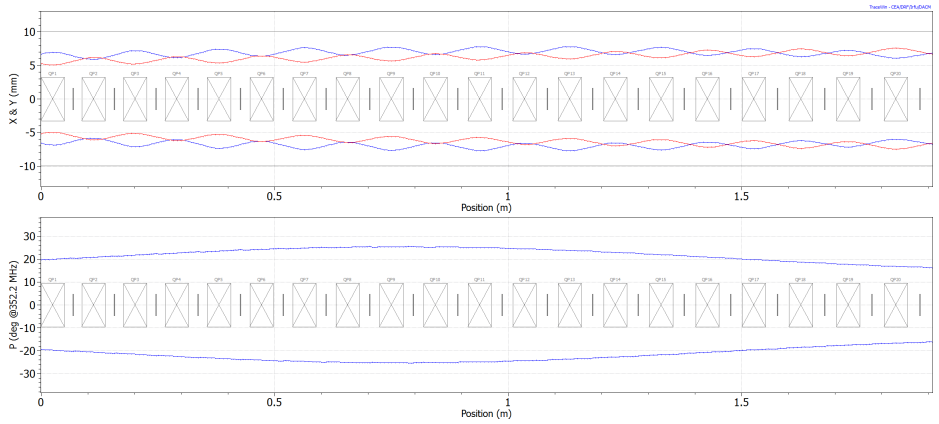
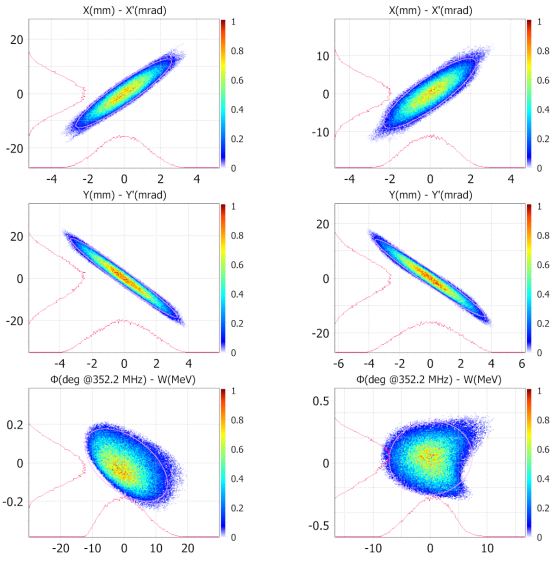


Figure 5.30: Beam envelopes along the DTL2 from 7.1 MeV/u to 10 MeV/u for helium ions at a beam current of 30 mA. The top plot represents transverse beam envelopes in the xz and yz planes, while the bottom plot shows the phase envelope.

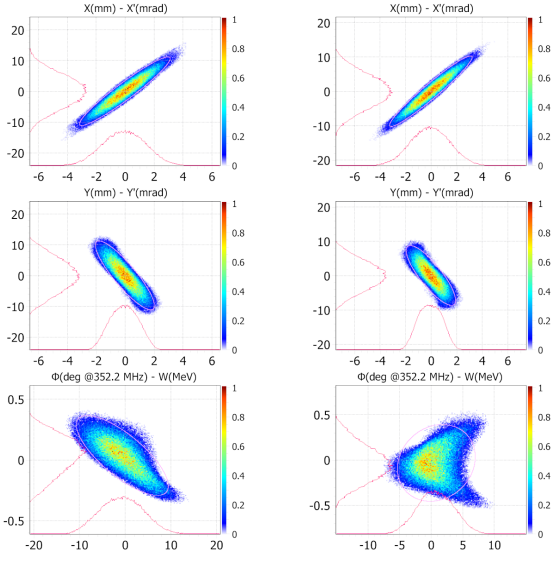
In addition to the beam envelopes, the beam transverse and longitudinal phase space within each structure were also computed. The phase space of the helium ions at a nominal beam current of 30 mA, at both the entrance and exit of DTL1, are presented in Figure 5.31



(a) **(b)**

Figure 5.31: Helium ion phase space (left column) at 5 MeV/u and (right column) at 7.1 MeV/u with the nominal beam current of 30 mA within DTL1.

On the contrary, the phase spaces for 30 mA helium ions in both transverse and longitudinal planes at the start and end of DTL2 are shown in Figure 5.32.



(a) **(b)**

Figure 5.32: Helium ion phase space (left column) at 7.1 MeV/u and (right column) at 10 MeV/u with the nominal beam current of 30 mA within DTL2.

5.2.4 Debunching cavity and energy ramping cavity before injection into helium synchrotron

For the NIMMS linac, which is designed to inject helium ions into a cancer therapy synchrotron, the inclusion of a Debunching Cavity (DEB) is essential. Alongside the DEB, an Energy Ramping Cavity (ERC) has been designed as an optional yet valuable addition to the linac configuration. As discussed in detail in Subsection 3.3.4, the ERC uses an advanced technique and offers a more efficient beam injection into the synchrotron. However, this comes at the cost of added complexity in the control system. Additionally, to mitigate overall manufacturing costs, both the DEB and ERC have been integrated as part of the DTL1 and DTL2 structures.

In practical terms, the first cell of DTL1 is optimized to serve as an accelerating cell or as the ERC for ramping the energy of particles. This dual-purpose structure significantly complicates the design process but results in a space-saving and cost-effective unit. Similarly, the first cell of the DTL2 can operate either as the DEB or as an accelerating cell. Both the ERC and DEB are isolated from the rest of the accelerating units by copper walls, allowing for independent operation. In other words, when the linac produces radioisotopes, both DEB and ERC function as accelerating cells operating at a synchronous phase along with the rest of the DTL structures, but when the linac injects a beam into the synchrotron, only DEB and ERC are excited at the zero crossing phase, while the rest of the DTL structures are off.

The electric field distributions for both cavities are displayed in Figure 5.33.

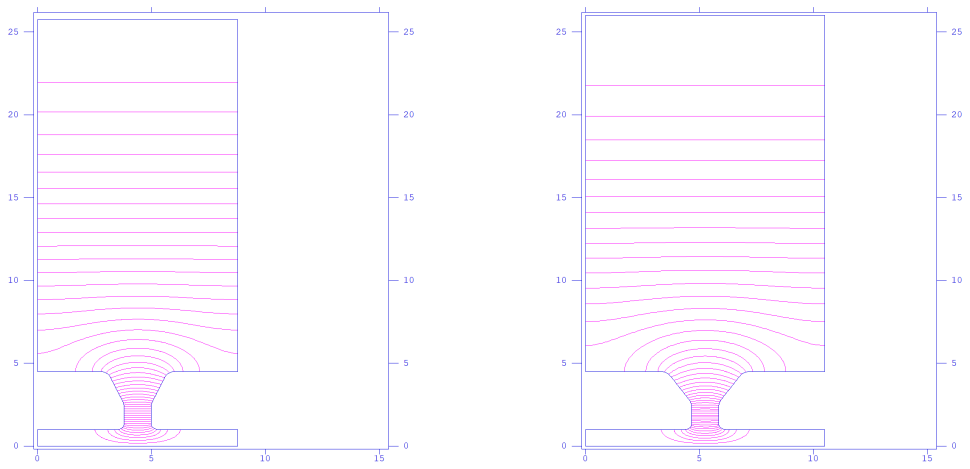


Figure 5.33: Electric field distribution in (a) ERC used for ramping the energy, and (b) DEB used for reducing energy spread of helium ions before injection into therapy synchrotron, simulated with Poisson/SUPERFISH codes.

In addition to the electric field distributions, the RF and geometry parameters of both structures are summarized in Table 5.27.

Table 5.27: RF and geometry parameters of ERC used for ramping the energy and DEB used for reducing energy spread of helium ions before injection into therapy synchrotron

	ERC	**DEB**	**Units**
No. of cells	1	1	-
Bore radius	10	10	mm
Cavity radius	254	258	mm
Length	88	105	mm
Accelerated field	3.1	1.4	MV/m
Maximal surface field	1.3	0.8	kp
Synchronous phase	-146.9 to -33.1	-90	deg
Effective shunt impedance	51.19	53.84	MΩ/m
Nominal tank voltage	240	130	kV
Power dissipation	35	8	kW

One important observation from Table 5.27 is the synchronous phase range provided for the ERC. This range, rather than a single value, is due to the nature of the ERC operation, where the synchronous phase continuously shifts between $-146.9°$ and $-33.1°$. This behavior is demonstrated in Figure 3.21. The minimum and maximum synchronous phase points within the ERC are chosen to correspond to a maximum energy gain or loss of 0.4 MeV, corresponding to an energy shift of 2% ($\Delta W/W \leq 2\%$) [109].

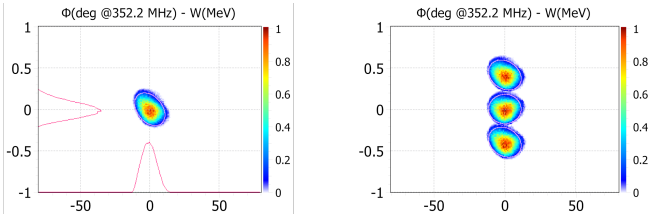
The beam dynamics were analyzed using TraceWin. The normalized rms longitudinal emittances and the energy spread (for 95% of the beam) were computed at both the entrance and exit of the ERC and DEB cavities. These results are documented in Table 5.28.

In the longitudinal phase space plots shown in Figure 5.34, the beam entering the ERC starts with an energy of 20 MeV. Upon exiting the ERC, the beam exhibits one of the energy values within the range of 19.6 MeV to 20.4 MeV. These energy deviations correspond to the expected energy shift, within the allowed ± 0.4 MeV range.

Following the ERC, the beam undergoes a drift until it reaches the entrance of the DEB, as the DTL1 structure is off during this mode of operation. During the drift through DTL1, the beam becomes elongated but narrower, as shown in Figure 5.35a. As the beam passes through the DEB, the electric field corresponding to the voltage of 130 kV reduces the energy spread by effectively rotating the beam bunch in longitudinal phase space, as illustrated in Figure 5.35b.

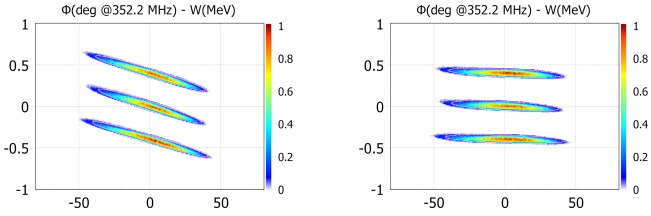
Table 5.28: Beam parameters of ERC used for ramping the energy and DEB used for reducing the energy spread of helium ions before injection into the therapy synchrotron

	Beam energy [MeV]	**ERC**	**DEB**	**Units**
Input long. norm.emi-ttance (rms)	19.6	0.403	0.405	π.deg.MeV
	20.0	0.403	0.404	π.deg.MeV
	20.4	0.403	0.401	π.deg.MeV
Output long. norm.emi-ttance (rms)	19.6	0.406	0.406	π.deg.MeV
	20.0	0.404	0.404	π.deg.MeV
	20.4	0.402	0.403	π.deg.MeV
Input energy spread(for 2σ (95% beam))	19.6	$\pm$0.83	$\pm$1.12	%
	20.0	$\pm$0.83	$\pm$1.08	%
	20.4	$\pm$0.83	$\pm$1.07	%
Output energy spread(for 2σ (95% beam))	19.6	$\pm$0.93	$\pm$0.29	%
	20.0	$\pm$0.92	$\pm$0.32	%
	20.4	$\pm$0.90	$\pm$0.30	%



(a) **(b)**

Figure 5.34: Helium ion phase space (left column) before and (right column) after ERC.



(a) **(b)**

Figure 5.35: Helium ion phase space (left column) before and (right column) after DEB.

5.2.5 Comparison and choice of the ideal linac configuration

The NIMMS linac consists of three linac sections. For the first linac section, the QA-DTL and IH-DTL were studied and compared to serve as a synchrotron injector, while for the second and third linac sections, two DTL structures were designed.

Regarding the length, the IH-DTL requires 32.9% less space (corresponding to 1.5 meters) compared to the QA-DTL. Additionally, the IH-DTL requires 47% less power than the QA-DTL. However, similar to the HITRI*plus* linac, the QA-DTL, designed as the first linac structure of the NIMMS linac, operates at higher frequencies compared to the IH-DTL. This enables the use of more available RF source solutions, such as klystrons, which become more efficient as power consumption and operational frequency increase. This can potentially reduce cost by a factor of two compared to SSA [113]. On the other hand, the power-efficient IH-DTL operates at a frequency of 176 MHz, limiting the choice of RF source to Solid-State Amplifiers (SSA).

Regarding beam dynamics, the situation is the opposite. In the case of the IH-DTL, normalized rms emittance growths of 19.6% in the transverse plane, and 20.8% in the longitudinal plane have been observed. In contrast, QA-DTL exhibits significantly lower normalized rms emittance growth: 3.2% in the transverse plane, and 2.5% in the longitudinal plane. It is important to note that QA-DTL can accelerate helium ions and deuterons up to 30 mA and operate in combination with the following two DTL sections, while IH-DTL has been designed to accelerate only 5 mA of helium ions for synchrotron injection. Also, it is not possible to use IH-DTL in combination with the Alvarez-type structures due to the different beam dynamics, as noted in Subsection 5.1.5. On the other hand, the energy spread at the exits of both QA-DTL and IH-DTL remains the same. The parameters of QA-DTL and IH-DTL for helium ion acceleration are shown in Table 5.29.

Table 5.29: Comparison between QA-DTL and IH-DTL for helium ion acceleration

	Power diss. [kW]	**Power source**	**Length [mm]**	**Norm. trans. / long. rms emit. growth [%]**
QA-DTL	570	klystron	4.65	3.2 / 2.5
IH-DTL	302	SSA	3.12	19.6 / 20.8

Since the RF costs of QA-DTL are comparable to those of IH-DTL, and the beam dynamics of QA-DTL are superior, the QA-DTL has been chosen as the preferred linac structure for the first section of the NIMMS linac. Despite the beam transmission of 100% in both structures, since the IH-DTL uses KONUS beam dynamics where the majority of the longitudinal period has the synchronous phase of 0 degrees, which is not considered stable motion in the longitudinal phase space [95], the IH-DTL is more prone to beam loss when errors are introduced. Especially at a 10% duty cycle, the beam losses are a concern due to activation and high radioactivity.

For the second and third NIMMS linac sections, two DTL structures have been chosen, as DTL has comparable power requirements to the other linac solutions at energies above 5 MeV/u, with superior beam performance. The power dissipation of DTL1 is 235 kW, while for DTL2 it is equal to 300 kW. Both DTL1 and DTL2 are designed so that the first cells of each structure can work as accelerating cells during radioisotope production, or as DEB or ERC when the linac is used as a synchrotron injector, as mentioned in Subsection 5.2.4. This design significantly reduces the overall required linac space, resulting in a 1.74 m long DTL1 including ERC, and a 2.28 m long DTL2 including DEB. The power dissipation and length of each linac unit, along

with estimated BTL length, are shown in Table 5.30.

Table 5.30: Overview of Alvarez-type linac configuration for helium ion acceleration

	Power diss. [kW]	**Length [m]**
QA-DTL	570	4.65
DTL1 + BTL (with ERC)	235	2.01
DTL2 + BTL (with DEB)	300	2.61
Alvarez-type (total)	**1105**	**9.27**

According to the aforementioned, the final NIMMS linac layout consists of QA-DTL as the first section, DTL1 as the second section, and DTL2 as the third section. The overall layout of the NIMMS linac configuration, consisting of both DEB and ERC cavities, is shown in Figure 5.36.

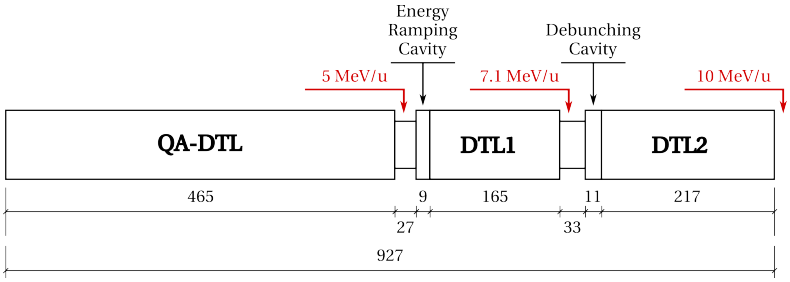


Figure 5.36: Layout of preferred NIMMS linac configuration. Dimensions are given in cm.

5.3 Isotope production helium linac design

A QA-DTL linac structure specifically devoted to producing one of the most promising alpha-therapy radioisotopes, the 211-Astatine, has been designed. This QA-DTL is capable of accelerating helium ions with a nominal beam current of 30 mA from 1 MeV/u up to 7.1 MeV/u. Unlike the other linac configurations discussed in this thesis, this design is not intended to be used as an injector for the cancer therapy synchrotron. The output energy of 7.1 MeV/u (corresponding to a total energy of 28.4 MeV) was chosen to optimize the production of ^{211}At while keeping the energy slightly below the threshold for producing the undesirable ^{210}At, which has a threshold energy of 28.6 MeV [114–116].

The QA-DTL is designed to operate at 352.2 MHz. The EM simulations have been carried out using the Poisson/SUPERFISH codes, computing the electric field distribution within the structure, as shown in Figure 5.37.

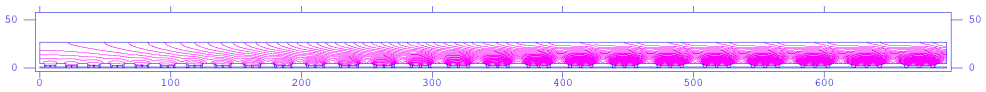


Figure 5.37: Electric field distribution in QA-DTL for helium ion acceleration from 1 MeV/u to 7.1 MeV/u, simulated with Poisson/SUPERFISH codes.

Table 5.31 presents the RF and geometry parameters of the QA-DTL used for helium ion acceleration from 1 MeV/u to 7.1 MeV/u. The accelerating field is 3.5 MV/m, with a maximum surface field limited to 1.8 Kp. Similar to other QA-DTL designs presented in this thesis, the synchronous phase for this QA-DTL design also starts at -35° and increases by 1° per super-period until reaching -24°.

The structure has a length of 6.9 meters and a cavity radius of 26.6 cm, with 25 super-periods. The effective shunt impedance per unit length is 62.18 MΩ/m, and the power dissipation is 770 kW.

Table 5.31: RF and geometry parameters of the QA-DTL for helium ion acceleration from 1 MeV/u to 7.1 MeV/u

	QA-DTL	**Units**
Operating frequency	352.2	MHz
Input energy	4	MeV
Output energy	28.4	MeV
RF duty cycle	10	%
Peak beam current	30	mA
Accelerated field	3.5	MV/m
Maximal surface field	1.8	kp
Synchronous phase	-35 to -24	deg
Length	6.9	m
Cavity radius	26.6	cm
Total RF power	1.14	MW
No. of super-periods	25	-
Effective shunt impedance	62.18	MΩ/m
Nominal tank voltage	18.1	MV
Power dissipation	770	kW
Beam power	366	kW

Similarly to previous designs, each PMQ within this QA-DTL structure is chosen to be made of samarium cobalt material and as such is constrained with a maximum gradient strength of 100 T/m for the given bore radius. A transverse phase advance of 68° has been chosen as a

compromise between beam excursions and quadrupole gradient strength. The length and gradient strength of each PMQ is shown in Table 5.32.

Table 5.32: PMQ parameters of the QA-DTL for helium ion acceleration from 1 MeV/u to 7.1 MeV/u

No.	Grad. Str. [T/m]	Length [mm]	·	No.	Grad. Str. [T/m]	Length [mm]
1.	70.72	60	·	**14.**	-61.46	60
2.	-70.62	60	·	**15.**	60.84	60
3.	67.29	60	·	**16.**	-60.83	60
4.	-67.18	60	·	**17.**	60.27	60
5.	65.02	60	·	**18.**	-60.26	60
6.	-64.98	60	·	**19.**	59.99	60
7.	63.99	60	·	**20.**	-59.97	60
8.	-63.96	60	·	**21.**	59.78	60
9.	63.07	60	·	**22.**	-59.77	60
10.	-63.04	60	·	**23.**	59.64	60
11.	62.23	60	·	**24.**	-59.63	60
12.	-62.21	60	·	**25.**	59.42	60
13.	61.49	60	·	-	-	-

Beam dynamics analysis was conducted using the TraceWin code. The simulations ensured 100% helium ion transmission at a nominal beam current of 30 mA. The beam parameters in both the transverse and longitudinal planes at the entrance and exit of the QA-DTL were successfully computed and are documented in Table 5.33.

Due to the high beam current, the bore radius is 10 mm. The input transverse normalized rms emittance in both the horizontal and vertical planes is 0.25 π.mm.mrad. At the output, the transverse normalized rms emittance slightly increases to 0.253 π.mm.mrad (corresponding to 1.2% normalized rms emittance growth) in the horizontal plane and 0.252 π.mm.mrad (corresponding to 0.8% normalized rms emittance growth) in the vertical plane.

For the longitudinal plane, the input normalized rms emittance is 0.394 π.deg.MeV, and at the output it increases to 0.406 π.deg.MeV (corresponding to 3% normalized rms emittance growth). The energy spread for 95% of the beam is $\pm$0.69%.

Figure 5.38 illustrates both the transverse and longitudinal beam envelopes for helium ions at the nominal beam current of 30 mA within the QA-DTL.

Table 5.33: Beam parameters of the QA-DTL for helium ion acceleration from 1 MeV/u to 7.1 MeV/u

	QA-DTL	Units
Bore radius	10	mm
Max. grad. str.	100	T/m
Input tran. norm. emittance (rms)(xx')	0.250	π.mm.mrad
Input tran. norm. emittance (rms)(yy')	0.250	π.mm.mrad
Output tran. norm. emittance (rms)(xx')	0.253	π.mm.mrad
Output tran. norm. emittance (rms)(yy')	0.252	π.mm.mrad
Input long. norm. emittance (rms)	0.394	π.deg.MeV
Output long. norm. emittance (rms)	0.406	π.deg.MeV
Energy spread (for 2σ (95% beam))	$\pm$0.69	%
α_x (at output)	0.811	-
β_x (at output)	0.311	mm/π.mrad
α_y (at output)	-3.457	-
β_y (at output)	1.439	mm/π.mrad
Transmission	100	%

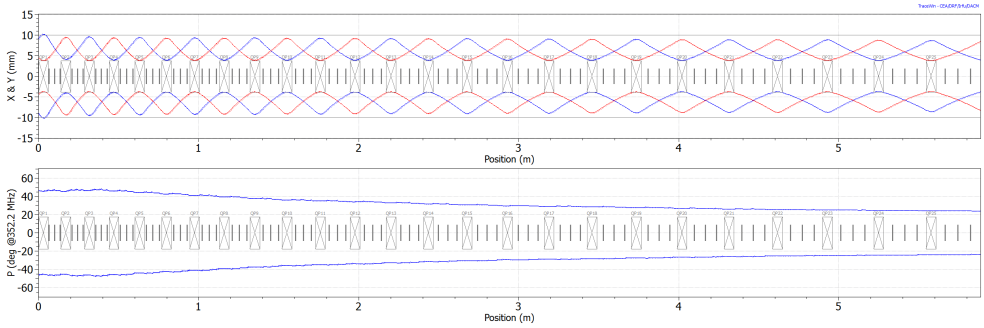
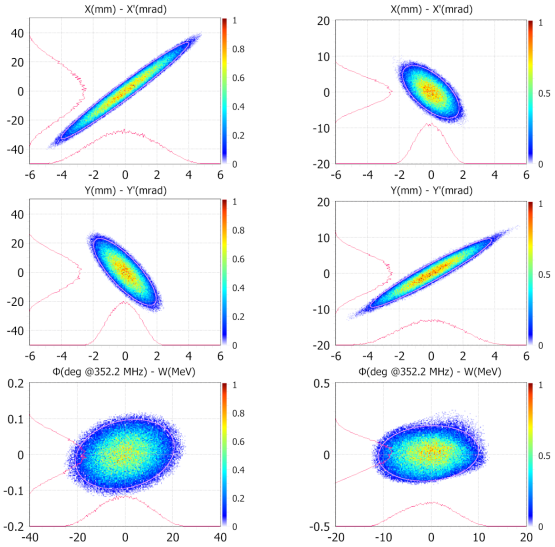


Figure 5.38: Beam envelopes along the QA-DTL from 1 MeV/u to 7.1 MeV/u with 30 mA of beam current used for radioisotope production. The top plot represents transverse beam envelopes in the xz and yz planes, while the bottom plot shows the phase envelope.

To further describe the beam dynamics, phase space plots for helium ions were created at both the entrance and exit of the QA-DTL, and are presented in Figure 5.39.



(a) **(b)**

Figure 5.39: Helium ion phase space (left column) at 1 MeV/u and (right column) at 7.1 MeV/u with the nominal beam current of 30 mA within QA-DTL.

5.4 Conclusions

Throughout this chapter, the preferred linac configurations for each of the three applications have been chosen to serve as the linac for the future carbon or helium particle therapy facilities. The HITRI*plus* linac configuration consists of QA-DTL as the first section, responsible for accelerating carbon and helium ions up to the energy of 5 MeV/u, and followed by two DTL cavities designed to accelerate helium ions up to 7.1 MeV/u and 10 MeV/u, respectively, as shown in Figure 5.40a. Similar to the HITRI*plus* linac, the NIMMS linac configuration consists of QA-DTL and two cavities of DTL designed to accelerate up to 30 mA of helium ions or deuterons, resulting in higher radioisotope production (Figure 5.40b). The combination of QA-DTL and two DTL structures has been chosen due to their superior beam dynamics, allowing stable motion in the longitudinal direction, and at the same time requiring comparable length and power to the other available solution, the IH-DTL. Based on its demonstrated performance, the QA-DTL has been designed to accelerate helium ions up to 7.1 MeV/u as a single cavity exclusively for radioisotope production (Figure 5.40c).

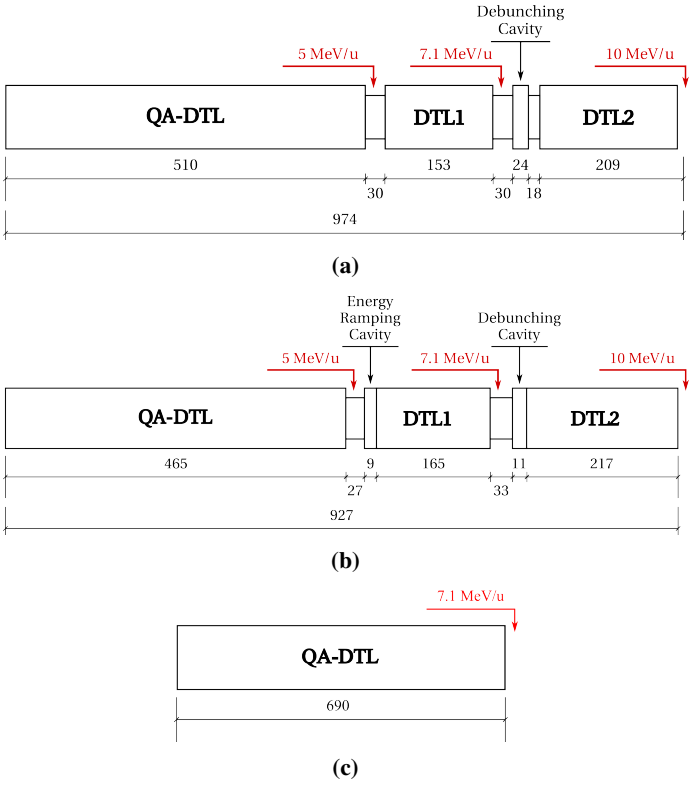


Figure 5.40: Layout of preferred (a) HITRI*plus*, (b) NIMMS, and (c) Astatine linac configuration. Dimensions are given in cm.

The DTL structures have superior beam dynamics over the IH-DTL, but they are not able to accelerate low-velocity particles as well as the IH-DTL structures are. Therefore, this thesis aimed to investigate a structure proposed several decades ago, which was never built due to technological limitations, but is capable of accelerating low-velocity particles similarly to the IH-DTL structure. The developed QA-DTL, presented in this thesis, enables the usage of the DTL structure in any future particle therapy facility that uses helium or carbon ions, providing a linac solution with improved beam performance over an IH-DTL design.

6. Conclusions

The goal of this thesis was to design linear accelerating structures for the injection of carbon and helium ions at an energy of 5 MeV/u into cancer therapy synchrotrons and the parallel production of radioisotopes with energy up to 10 MeV/u. This goal was successfully achieved by completing the following five tasks:

1. The first task was to **investigate existing ion linac structures** that could be used as a carbon and helium injector for a cancer therapy synchrotron. This was accomplished through an intensive literature analysis, resulting in the identification of twelve distinct linac structures. For low-velocity helium and carbon ion acceleration, two structures were selected for further investigation - namely, Interdigital H-mode Drift Tube Linac (IH-DTL) and Alvarez Drift Tube Linac (DTL). Based on the investigation, it was also proposed that further performance improvements for low-velocity ion injectors of a therapy synchrotron could be achieved by developing a Quasi-Alvarez Drift Tube Linac (QA-DTL), the modification of the DTL, and designing a Separated tanks Interdigital H-mode Drift Tube Linac (S-IH-DTL), the modification of the IH-DTL.

2. The second task was to define an optimization methodology for designing linac accelerating structures, by maximizing power efficiency and ensuring beam transmission without any loss of particles. To achieve this, **optimization algorithms** were developed to maximize the effective shunt impedance per unit length (ZT^2), which is proportional to the power efficiency. Furthermore, the gradient strengths of the permanent magnet quadrupoles, responsible for transverse beam focusing, were optimized to ensure loss-free beam transport within all linac structures.

3. The third task was to **design and optimize different linac structures** with the required input and output parameters, to be used as ion injectors for cancer therapy synchrotrons, or for the production of radioisotopes at different energies. To accomplish this, a new design of QA-DTL was developed. The developed QA-DTL allows ion acceleration at lower energies compared to its predecessor, the DTL. Alongside the QA-DTL, a new S-IH-DTL was designed, while for radioisotope production, a DTL was chosen.

4. The fourth task was to **compare the different linac structures** designed under task three and select the overall best solution for future carbon and helium cancer therapy facilities. The compared linac structures for the acceleration of low-velocity ions were the QA-DTL,

IH-DTL, and S-IH-DTL. Furthermore, for radioisotope production, at energies above 5 MeV/u, the DTL and IH-DTL were compared. All comparisons were based on beam performance, power efficiency, and overall length. Additionally, for low-velocity ion acceleration, a comparison of the total costs between the DTL and QA-DTL was made. A combination of QA-DTL and two DTL cavities was identified as the best linac solution for the future carbon and helium cancer therapy facilities and for the production of a wide range of radioisotopes.

5. Lastly, the fifth task was to **integrate the designed linac structures** into the proposed ion therapy facilities. This was accomplished by integrating the optimized linac solution (the combination of QA-DTL and two DTL cavities) into the general design for both the HITRI*plus* carbon linac and the NIMMS helium linac. Ultimately, due to its demonstrated performance, this configuration was selected as the proposed injector for the future Advanced Particle Therapy Center for the Baltic States [52].

The hypothesis was confirmed by demonstrating a cost-effective and flexible solution for ion acceleration using a linac. Additionally, the results of this thesis demonstrated that the QA-DTL provides superior beam performance compared to the IH-DTL, thanks to its better focusing lattice (the arrangement of transverse focusing quadrupoles that repeats along the linac structure) and the stable synchronous phase (the phase at which the synchronous particle is aligned with the accelerating field).

6.1 Thesis statements to be defended

1. For the acceleration of low-velocity carbon and helium ions, as an injector for a cancer therapy synchrotron, the developed linac structure (QA-DTL) has 61% lower total costs (cost of the accelerating structure and cost of the RF system) in comparison to the DTL.

2. The developed linac structure is capable of accelerating carbon ions from 0.7 MeV/u, whereas the DTL is capable of accelerating ions from 1 MeV/u at a lower beam current, thus simplifying the preceding accelerating section.

3. The beam within the developed linac structure has more stable longitudinal motion than within the IH-DTL structure currently used in ion therapy, resulting in improved output beam parameters with no beam loss. Specifically, for carbon ion acceleration, comparisons between the QA-DTL and IH-DTL showed significantly lower longitudinal normalized rms emittance growth in favor of the QA-DTL (2.02% vs. 25.7%), while for helium ion acceleration, the QA-DTL also exhibited significantly lower normalized rms emittance growth in the longitudinal plane (2.5% vs. 20.8%).

4. The combination of QA-DTL and two DTL cavities was identified as the best linac solution for integration into future carbon and helium ion therapy facilities and parallel

use in radioisotope production. The combination of the developed QA-DTL and two DTL cavities is shorter (9.74 m vs. 11.55 m), with practically the same power requirements (1077 kW vs. 1050 kW) compared to an IH-DTL based solution.

6.2 Future research challenges

The detailed research presented in this thesis has provided essential data and laid the groundwork for manufacturing a full-scale short prototype of the QA-DTL, which should be the focus of future research. This prototype should not be intended to accelerate particles, in order to keep costs low, but rather to enable RF measurements and provide an opportunity to explore topics not covered in this thesis, such as investigating post-couplers and field stabilizers, along with developing tuners. Both stabilizers and tuners are crucial for the proper operation of linac structures and must be addressed in future research.

Long DTL and QA-DTL cavities require tight mechanical tolerances to maintain a constant accelerating field along their length. A standard technique to mitigate this sensitivity, and to reduce the machining requirements, involves the use of post-couplers - short metallic posts protruding from the tank toward the drift tubes, alternating from side to side. This stabilization technique improves field flatness by coupling the main accelerating mode with a chain of post-coupler modes, and has to be considered for the QA-DTL.

It is important to mention that the ratio between the cavity radius and the drift tube radius in the developed linac structure is 5.9, which is very close to the value of 5.8 in LINAC4 at CERN [2]. Since the field stabilization of Linac4 was relatively straightforward [117], similar stabilization is expected for the QA-DTL structure. Nevertheless, this must be confirmed through testing on a full-scale prototype of the developed structure. In the event that prototype measurements indicate stabilization issues, the use of a $3/4\lambda$ post-coupler stabilization system, as described in [118], is foreseen.

Additionally, the injector for the linac structure requires further study. More specifically, the ion source and Radio Frequency Quadrupole (RFQ), responsible for pre-acceleration and beam-bunching before the linac structure, should be developed and integrated with the proposed linac configuration. Special attention should be given to the ion source, as a high-current helium beam is required for efficient radioisotope production with the developed QA-DTL linac structure.

BIBLIOGRAPHY

[1] A. Mamaras *et al.*, "Alvarez drift tube linac for medical applications in the framework of HITRIplus project," in *Proc. 14th International Particle Accelerator Conference (IPAC'23)*, JACoW Publishing, 2023, pp. 1717–1720. DOI: 10.18429/JACoW-IPAC2023-TUPA176.

[2] M. Vretenar *et al.*, *Linac4 Design Report* (CERN Yellow Reports: Monographs). Geneva: CERN, Sep. 2020, vol. 6/2020. DOI: 10.23731/CYRM-2020-006.

[3] M. T. Menzel and H. K. Stokes, *User's guide for the POISSON/SUPERFISH group of codes*, English, Report LA-UR-87-115, Los Alamos National Laboratory (LANL), Los Alamos, NM, USA, Jan. 1987, 207 pp.

[4] Dassault Systèmes Simulia Corp., *CST Studio Suite: 3d EM simulation and analysis software*, Computer software, Dassault Systèmes, Vélizy-Villacoublay, France, 2025.

[5] D. Uriot and N. Pichoff, *TraceWin: Beam dynamics simulation code for linear accelerators*, Computer software, Commissariat à l'énergie atomique et aux énergies alternatives (CEA), Saclay, France, 2025.

[6] S. Hanna, *RF Linear Accelerators for Medical and Industrial Applications*, 1st. Norwood, MA, USA: Artech House, 2012, p. 210, ISBN: 9781608070909.

[7] Y. M. Zhang, Y. J. Pei, L. S. Sheng, and Y. F. Song, "Research of L-band disk-loaded waveguides travelling wave accelerating structures for a high power Linac," in *Journal of Physics: Conference Series*, vol. 874, IOP Publishing, 2017, p. 012 018. DOI: 10.1088/1742-6596/874/1/012018.

[8] A. Figotin, "Analytic theory of coupled-cavity traveling wave tubes," *Journal of Mathematical Physics*, vol. 64, no. 4, p. 042 705, 2023. DOI: 10.1063/5.0102701.

[9] L. W. Alvarez, "Linear accelerator," U.S. Patent US2770755A, Mar. 20, 1951.

[10] S. Wang *et al.*, "RF measurement and tuning for an Alvarez-type drift tube linear accelerator without post couplers," *Nuclear Instruments and Methods in Physics Research Section A: Accelerators, Spectrometers, Detectors and Associated Equipment*, vol. 1053, p. 168 372, 2023. DOI: 10.1016/j.nima.2023.168372.

[11] X. Du, A. Seibel, S. Mickat, and L. Groening, "Alvarez DTL cavity design for the UNILAC upgrade," in *Proc. 6th International Particle Accelerator Conference (IPAC'15)*, JACoW Publishing, 2015, pp. 3776–3778. DOI: 10.18429/JACoW-IPAC2015-WEPMA017.

[12] D. Liska and D. Warner, “Design proposal for a Quasi-Alvarez structure for the new lead ion Linac,” CERN, Geneva, Switzerland, Tech. Rep. CERN PS/91-05 (HI), 1991.

[13] P. Lapostolle, D. J. Warner, M. Vretenar, E. Tanke, and S. Valero, “Computer design and dynamics of the Quasi-Alvarez Linac,” CERN, Geneva, Switzerland, Tech. Rep. CERN PS/90-68 (DI), 1990.

[14] D. J. Warner and J. C. Nanan, “Single cavity design for the Quasi-Alvarez Linac between 0.24 MeV/u and 4.2 MeV/u,” CERN, Geneva, Switzerland, Tech. Rep. CERN PS/91-08 (HI), 1991.

[15] M. R. Khalvati, V. Bencini, and S. Ramberger, “Quasi-Alvarez drift-tube Linac structures for heavy ion therapy accelerator facilities,” *Physical Review Accelerators and Beams*, vol. 26, no. 2, p. 022 001, 2023. DOI: 10.1103/PhysRevAccelBeams.26.022001.

[16] J. M. Garland, J.-B. Lallement, and A. Lombardi, “LINAC5 – a Quasi-Alvarez Linac for BioLEIR,” in *Journal of Physics: Conference Series*, vol. 874, IOP Publishing, 2017, p. 012 057. DOI: 10.1088/1742-6596/874/1/012057.

[17] T. Ito *et al.*, “RF characteristics of the SDTL for the J-PARC,” in *Proc. 23rd International Linear Accelerator Conference (LINAC’06)*, JACoW Publishing, 2006, pp. 749–751.

[18] T. Kato, “Proposal of a separated-type proton drift tube Linac for a medium-energy structure,” National Lab. for High Energy Physics (KEK), Tsukuba, Japan, Tech. Rep. KEK Report 92-10, 1992.

[19] C. Kazusa and M. Yoneda, “Side-coupled standing-wave linear accelerator,” U.S. Patent US4746839A, May 24, 1988.

[20] L. Picardi, C. Ronsivalle, and B. Spataro, “The first module of the 3 GHz side coupled drift tube Linac (SCDTL): Numerical studies of RF properties and cold tests results,” in *Proc. 7th European Particle Accelerator Conference (EPAC’00)*, JACoW Publishing, 2000, pp. 1999–2001.

[21] L. Picardi, C. Ronsivalle, and B. Spataro, “Numerical studies and measurements on the side-coupled drift tube Linac (SCDTL) accelerating structure,” *Nuclear Instruments and Methods in Physics Research Section B: Beam Interactions with Materials and Atoms*, vol. 170, no. 1–2, pp. 219–229, 2000. DOI: 10.1016/S0168-583X(00)00160-9.

[22] E. Benedico-Mora and M. Vretenar, “Design of a side-coupled linear accelerator structure for Linac4,” CERN, Geneva, Switzerland, Tech. Rep. CERN-AB-2005-044-RF, 2005.

[23] J. H. Billen, “Coupled-cavity drift-tube Linac,” U.S. Patent US5578909A, Nov. 26, 1996.

[24] M. Vretenar, Y. Cuvet, J. Genest, C. Vollinger, and F. Gerigk, “Development of a 352 MHz cell-coupled drift tube Linac prototype,” in *Proc. 22nd International Linear Accelerator Conference (LINAC’04)*, JACoW Publishing, 2004, pp. 57–59.

[25] Y. Cuvet *et al.*, "Development of a cell-coupled drift tube Linac (CCDTL) for Linac4," in *Proc. 24th International Linear Accelerator Conference (LINAC'08)*, JACoW Publishing, 2008, pp. 67–69.

[26] F. Gerigk and M. Vretenar, "Design of the 120 MeV drift tube Linac for the SPL," CERN, Geneva, Switzerland, Tech. Rep. CERN-PS-RF-Note-2000-019, 2000.

[27] F. Gerigk and R. Wegner, "Design of the Pi-mode structure (PIMS) for Linac4," in *Proc. 23rd Particle Accelerator Conference (PAC'09)*, Vancouver, BC, Canada: JACoW Publishing, 2009, pp. 4881–4883.

[28] R. Wegner *et al.*, "Linac4 PIMS construction and first operation," in *Proc. 8th International Particle Accelerator Conference (IPAC'17)*, JACoW Publishing, 2017, pp. 4307–4310. DOI: 10.18429/JACoW-IPAC2017-THPIK094.

[29] K. W. Shepard, S. Takeuchi, and G. P. Zinkann, "Development of superconducting niobium accelerating structures for heavy ions," *IEEE Transactions on Magnetics*, vol. 21, no. 2, pp. 146–148, 1985. DOI: 10.1109/TMAG.1985.1063639.

[30] H. Ao *et al.*, "First annular-ring coupled structure cavity for the Japan proton accelerator research complex Linac," *Physical Review Special Topics — Accelerators and Beams*, vol. 15, no. 5, p. 051 005, 2012. DOI: 10.1103/PhysRevSTAB.15.051005.

[31] B. Schlitt and U. Ratzinger, "Drift tube accelerator for accelerating ion packets," German Patent DE10333454B4, Jul. 13, 2006.

[32] B. Schlitt and U. Ratzinger, "Drift tube accelerator for ion bunch acceleration," European Patent EP1505855A2, Jan. 11, 2017.

[33] R. Tang *et al.*, "IH-DTL design with modified KONUS beam dynamics for a synchrotron-based proton therapy system," *Nuclear Instruments and Methods in Physics Research Section A: Accelerators, Spectrometers, Detectors and Associated Equipment*, vol. 920, pp. 50–57, 2019. DOI: 10.1016/j.nima.2018.10.125.

[34] M. Maier *et al.*, "Commissioning of the Linac for the Heidelberg heavy ion cancer therapy centre (HIT)," in *Proc. 22nd Particle Accelerator Conference (PAC'07)*, IEEE, 2007, pp. 2734–2736. DOI: 10.1109/PAC.2007.4440558.

[35] P. A. Posocco *et al.*, "Status of Linac beam commissioning for the Italian hadron therapy center CNAO," in *Proc. 11th International Conference on Heavy Ion Accelerator Technology (HIAT'09)*, Venice, Italy, 2009, pp. 188–192.

[36] M. Benedikt, J. Gutleber, U. Dorda, A. Fabich, M. Palm, and W. Pirkl, "Overview of the MedAustron design and technology choices," CERN, Geneva, Switzerland, Tech. Rep. CERN-ATS-2010-116, 2010.

[37] D. A. Swenson, "Alternating phase focused Linacs," U.S. Patent US4211954A, Jul. 8, 1980.

[38] S. Lauber *et al.*, "An alternating phase focusing injector for heavy ion acceleration," *Nuclear Instruments and Methods in Physics Research Section A: Accelerators, Spectrometers, Detectors and Associated Equipment*, vol. 1040, pp. 1–11, 2022. DOI: 10.1016/j.nima.2022.167099.

[39] R. E. Laxdal, P. G. Bricault, T. Reis, and D. V. Gorelov, "A separated function drift-tube Linac for the ISAC project at TRIUMF," in *Proc. 17th Particle Accelerator Conference (PAC'97)*, vol. 1, IEEE, 1997, pp. 1194–1196. DOI: 10.1109/PAC.1997.749973.

[40] R. Brodhage, U. Ratzinger, H. Podlech, C. Fix, G. Clemente, and L. Groening, "First coupled CH power cavity for the FAIR proton injector," in *Proc. 2nd International Particle Accelerator Conference (IPAC'11)*, San Sebastián, Spain: JACoW Publishing, 2011, pp. 2565–2567.

[41] U. Amaldi, M. Dosanjh, J. Balosso, J. Overgaard, and B. Sørensen, "A facility for tumour therapy and biomedical research in south-eastern Europe," *CERN Yellow Reports: Monographs*, no. CERN-2019-002, 2019. DOI: 10.23731/CYRM-2019-002.

[42] G. Kraft, "History of the heavy ion therapy at GSI," *GSI Helmholtzzentrum für Schwerionenforschung GmbH, Planckstraße*, vol. 2, no. 64, p. 17, 2013.

[43] U. Scheeler *et al.*, "Recommissioning of the Marburg ion-beam therapy centre (MIT) accelerator facility," in *Proc. 7th International Particle Accelerator Conference (IPAC'16)*, JACoW Publishing, 2016, pp. 1908–1910. DOI: 10.18429/JACoW-IPAC2016-TUPOY004.

[44] B. Schlitt *et al.*, "Commissioning and operation of the injector Linacs for HIT and CNAO," in *Proc. 24th International Linear Accelerator Conference (LINAC'08)*, JACoW Publishing, 2008, pp. 720–724.

[45] T. P. Wangler, *RF Linear Accelerators*, 2nd. Weinheim, Germany: Wiley-VCH, 2008, ISBN: 978-3-527-40680-7. DOI: 10.1002/9783527623426.

[46] M. Okamura *et al.*, "A new medium energy beam transport line for the proton injector of AGS-RHIC," in *Proc. 25th International Linear Accelerator Conference (LINAC'10)*, Tsukuba, Japan: JACoW Publishing, 2010, pp. 458–460.

[47] R. Garoby *et al.*, "The European spallation source design," *Physica Scripta*, vol. 93, no. 1, p. 014 001, 2017. DOI: 10.1088/1402-4896/aa9bff.

[48] HITRIplus Consortium, *Heavy ion therapy research integration plus (HITRIplus), grant agreement ID 101008548*, European Commission, CORDIS project page, 2023. [Online]. Available: https://cordis.europa.eu/project/id/101008548.

[49] M. Rabiei, M. Asadi, and H. Yousefnia, "Astatine-211 radiopharmaceuticals: Status, trends, and the future," *Current Radiopharmaceuticals*, vol. 17, no. 1, pp. 7–13, 2024. DOI: 10.2174/0118744710262325231025075638.

[50] L. Litov, "SEEIIST — a new research facility for tumor treatment and biomedical investigations with proton and ion beams," *Health and Technology*, vol. 14, no. 5, pp. 957–963, 2024. DOI: 10.1007/s12553-024-00864-5.

[51] CERN – Conseil Européen pour la Recherche Nucléaire, *Next ion medical machine study (NIMMS)*, Project website, CERN, 2025. [Online]. Available: https://nimms.web.cern.ch.

[52] K. Paļskis *et al.*, "Particle therapy — future for the Baltic states? synthesis of the expert workshop report," *Health and Technology*, vol. 14, no. 5, pp. 965–972, 2024. DOI: 10.1007/s12553-024-00875-2.

[53] International Atomic Energy Agency, *Cyclotron Produced Radionuclides: Physical Characteristics and Production Methods* (Technical Reports Series 468). Vienna, Austria: International Atomic Energy Agency, 2009, ISBN: 978-92-0-106908-5.

[54] J. C. Clark and D. J. Silvester, "A cyclotron method for the production of fluorine-18," *The International Journal of Applied Radiation and Isotopes*, vol. 17, no. 3, pp. 151–154, 1966. DOI: 10.1016/0020-708X(66)90034-4.

[55] V. Casella, T. Ido, A. P. Wolf, J. S. Fowler, R. R. MacGregor, and T. J. Ruth, "Anhydrous F-18 labeled elemental fluorine for radiopharmaceutical preparation," *Journal of Nuclear Medicine*, vol. 21, no. 8, pp. 750–757, 1980.

[56] A. Hermanne, F. Tárkányi, S. Takács, S. F. Kovalev, and A. Ignatyuk, "Activation cross sections of the ^{64}Ni(d,2n) reaction for the production of the medical radionuclide ^{64}Cu," *Nuclear Instruments and Methods in Physics Research Section B: Beam Interactions with Materials and Atoms*, vol. 258, no. 2, pp. 308–312, 2007. DOI: 10.1016/j.nimb.2007.02.071.

[57] Y. Skakun and S. M. Qaim, "Excitation function of the ^{64}Ni(α,p)^{67}Cu reaction for production of ^{67}Cu," *Applied Radiation and Isotopes*, vol. 60, no. 1, pp. 33–39, 2004. DOI: 10.1016/j.apradiso.2003.09.003.

[58] I. Kambali and F. A. Wibowo, "Comparison of Gallium-68 production yields from (p,2n), (α,2n) and (p,n) nuclear reactions applicable for cancer diagnosis," in *Journal of Physics: Conference Series*, vol. 1198, IOP Publishing, 2019, pp. 1–10. DOI: 10.1088/1742-6596/1198/2/022003.

[59] A. M. La Gamma and S. J. Nassiff, "Excitation functions for deuteron-induced reactions on ^{89}Y," *Radiochimica Acta*, vol. 19, no. 4, pp. 161–162, 1973. DOI: 10.1524/ract.1973.19.4.161.

[60] S. Manenti *et al.*, "Excitation function and yield for the ^{103}Rh(d,2n)^{103}Pd nuclear reaction: Optimization of the production of Palladium-103," *Nuclear Medicine and Biology*, vol. 49, pp. 30–37, 2017. DOI: 10.1016/j.nucmedbio.2017.02.005.

[61] A. Nikjou and M. Sadeghi, "Overview and evaluation of different nuclear level density models for the ^{123}I radionuclide production," *Applied Radiation and Isotopes*, vol. 136, pp. 45–58, 2018. DOI: 10.1016/j.apradiso.2018.02.003.

[62] S. Takács *et al.*, "Excitation function of ^{122}Te(d,n)^{123}I nuclear reaction: Production of ^{123}I at a low energy cyclotron," *Applied Radiation and Isotopes*, vol. 50, no. 3, pp. 535–540, 1999. DOI: 10.1016/S0969-8043(98)00059-1.

[63] I. Kambali, "Production of Lu-177 radionuclide using deuteron beams: Comparison between (d,n) and (d,p) nuclear reactions," in *Journal of Physics: Conference Series*, vol. 1120, IOP Publishing, 2018, pp. 1–7. DOI: 10.1088/1742-6596/1120/1/012011.

[64] S. Lahiri and M. Maiti, "Recent developments in nuclear data measurements and chemical separation methods in accelerator production of astatine and technetium radionuclides," *Radiochimica Acta*, vol. 100, no. 8–9, pp. 535–541, 2012. DOI: 10.1524/ract.2011.1888.

[65] M. R. Zalutsky and M. Pruszynski, "Astatine-211: Production and availability," *Current Radiopharmaceuticals*, vol. 4, no. 3, pp. 177–185, 2011. DOI: 10.2174/1874471011104030177.

[66] G. Moffitt, *Medical radioisotope production platform*, Presentation, Nusano, 2023. [Online]. Available: https://nusano.com/wp-content/uploads/2023/05/Nusano_At211_COSTMeeting_webpub.pdf.

[67] N. B. Smith and A. Webb, *Introduction to Medical Imaging: Physics, Engineering and Clinical Applications*. Cambridge, UK: Cambridge University Press, 2010, ISBN: 978-0-521-19065-7.

[68] M. A. Flower, *Webb's Physics of Medical Imaging*, 2nd. Boca Raton, FL, USA: CRC Press, 2012, ISBN: 978-0-7503-0573-0.

[69] F. F. Knapp and A. Dash, *Radiopharmaceuticals for Therapy*. New Delhi, India: Springer, 2016, ISBN: 978-81-322-2606-2. DOI: 10.1007/978-81-322-2607-9.

[70] D. M. Pozar, *Microwave Engineering*, 4th. Hoboken, NJ, USA: Wiley, 2012, ISBN: 978-0-470-63155-3.

[71] C. A. Balanis, *Balanis' Advanced Engineering Electromagnetics*, 3rd. Hoboken, NJ, USA: John Wiley & Sons, 2024, ISBN: 978-1-394-18095-2.

[72] R. E. Collin, *Foundations for Microwave Engineering*, 2nd. Hoboken, NJ, USA: John Wiley & Sons, 2007, ISBN: 978-0-7803-6031-0.

[73] A. M. Labrador Garcia, "Beam dynamics equations and programs; Linac 2 applications including the high current case," CERN, Geneva, Switzerland, Tech. Rep. CERN PS/93-03 (HI), 1993.

[74] W. D. Kilpatrick, "Criterion for vacuum sparking designed to include both RF and DC," *Review of Scientific Instruments*, vol. 28, no. 10, pp. 824–826, 1957. DOI: 10.1063/1.1715731.

[75] T. J. Boyd Jr., "Kilpatrick's criterion," Los Alamos National Laboratory, Los Alamos, NM, USA, Tech. Rep. Los Alamos Group AT-1 Report AT-1:82-28, 1982.

[76] M. Vretenar, "Linear accelerators," in *CAS — CERN Accelerator School: High Power Hadron Machines*, Geneva, Switzerland: CERN, 2013, pp. 225–249. DOI: 10.5170/CERN-2013-001.225.

[77] M. Vretenar, "Low-beta structures," in *CAS — CERN Accelerator School: RF for Accelerators*, Geneva, Switzerland: CERN, 2011, pp. 319–340. DOI: 10.5170/CERN-2011-007.319.

[78] E. Wilson, *An Introduction to Particle Accelerators*. Oxford, UK: Oxford University Press, 2001, ISBN: 978-0-19-850829-8.

[79] H. Wiedemann, *Particle Accelerator Physics*, 4th. Cham, Switzerland: Springer Nature, 2015, ISBN: 978-3-319-18316-9. DOI: 10.1007/978-3-319-18317-6.

[80] S.-Y. Lee, *Accelerator Physics*, 4th. Singapore: World Scientific Publishing Company, 2018, ISBN: 978-981-3274-78-5.

[81] M. Conte and W. W. MacKay, *Introduction to the Physics of Particle Accelerators*, 2nd. Singapore: World Scientific Publishing Company, 2008, ISBN: 978-981-277-961-8.

[82] N. Pichoff, "Introduction to RF linear accelerators," in *CAS — CERN Accelerator School: Intermediate Accelerator Physics*, Geneva, Switzerland: CERN, 2006, pp. 105–128. DOI: 10.5170/CERN-2006-002.105.

[83] M. Weiss, "Introduction to RF linear accelerators," in *CAS — CERN Accelerator School: 5th General Accelerator Physics Course*, Geneva, Switzerland: CERN, 1994, pp. 913–953. DOI: 10.5170/CERN-1994-001.913.

[84] E. D. Courant, M. S. Livingston, and H. S. Snyder, "The strong-focusing synchrotron — a new high energy accelerator," *Physical Review*, vol. 88, no. 5, pp. 1190–1196, 1952. DOI: 10.1103/PhysRev.88.1190.

[85] J. P. Blewett, "Radial focusing in the linear accelerator," *Physical Review*, vol. 88, no. 5, pp. 1197–1199, 1952. DOI: 10.1103/PhysRev.88.1197.

[86] L. C. Teng, "Alternating gradient electrostatic focusing for linear accelerators," *Review of Scientific Instruments*, vol. 25, no. 3, pp. 264–268, 1954. DOI: 10.1063/1.1771038.

[87] L. Smith and R. L. Gluckstern, "Focusing in linear ion accelerators," *Review of Scientific Instruments*, vol. 26, no. 2, pp. 220–228, 1955. DOI: 10.1063/1.1771257.

[88] B. J. Holzer, "Lattice design in high-energy particle accelerators," in *CAS — CERN Accelerator School: Advanced Accelerator Physics*, Geneva, Switzerland: CERN, 2014, pp. 61–100. DOI: 10.5170/CERN-2014-009.61.

[89] K. Floettmann, "Some basic features of the beam emittance," *Physical Review Special Topics — Accelerators and Beams*, vol. 6, no. 3, p. 034 202, 2003. DOI: 10.1103/PhysRevSTAB.6.034202.

[90] D. Möhl, "Sources of emittance growth," in *CAS — CERN Accelerator School: Small Accelerators*, Geneva, Switzerland: CERN, 2006, pp. 45–69. DOI: 10.5170/CERN-2006-012.45.

[91] E. Cosgun, M. S. Hur, S. Moon, D. Kim, and M. Chung, "Time-resolved space-charge compensation studies for pulsed and matched proton beam in a low-energy transport line," *Physical Review Accelerators and Beams*, vol. 28, no. 9, p. 090 102, 2025. DOI: 10.1103/l8v5-ch9z.

[92] E. Sargsyan *et al.*, "Linac4 source and low energy experience and challenges," in *Proc. 68th ICFA Adv. Beam Dyn. Workshop on High-Intensity High-Brightness Hadron Beams (HB'23)*, JACoW Publishing, 2024, pp. 231–235. DOI: 10.18429/JACoW-HB2023-WEA4I2.

[93] I. M. Kapchinskij and V. V. Vladimirskij, "Limitations of proton beam current in a strong focusing linear accelerator associated with the beam space charge," in *Proc. International Conference on High Energy Accelerators and Instrumentation*, Geneva, Switzerland: CERN Scientific Information Service, 1959, pp. 274–288.

[94] D. J. Warner, "Heavy ion acceleration using drift-tube structures with optimised focusing," CERN, Geneva, Switzerland, Tech. Rep. CERN PS/88-63 (HI), 1988.

[95] R. Tiede, U. Ratzinger, H. Podlech, C. Zhang, and G. Clemente, "KONUS beam dynamics designs using H-mode cavities," in *Proc. 42nd ICFA Advanced Beam Dynamics Workshop on High-Intensity, High-Brightness Hadron Beams (HB'08)*, JACoW Publishing, 2008, pp. 223–230.

[96] D. E. Young, "Buildings and costs," in *Proceedings of the 1961 Conference on Linear Accelerators*, 1961. [Online]. Available: https://accelconf.web.cern.ch/l61/papers/talks-13.pdf.

[97] Los Alamos National Laboratory, *Los alamos national laboratory (LANL)*, Laboratory website, 2025. [Online]. Available: https://www.lanl.gov.

[98] J. H. Billen, *SFCODES2: Auxiliary codes for the POISSON/SUPERFISH group of programs*, English, Version 7.17, Los Alamos National Laboratory (LANL), Los Alamos, NM, USA, Jan. 2006, 64 pp.

[99] J. H. Billen, *SFCODES: Codes for the POISSON/SUPERFISH group of programs*, English, Version 7.17, Los Alamos National Laboratory (LANL), Los Alamos, NM, USA, Jan. 2006, 98 pp.

[100] J. H. Billen, *SFPHYS4: Physics notes for the POISSON/SUPERFISH group of codes*, English, Version 7.17, Los Alamos National Laboratory (LANL), Los Alamos, NM, USA, Jan. 2006, 24 pp.

[101] Dassault Systèmes Simulia Corp., *CST Studio Suite 2021 — high frequency simulation: User manual*, English, Dassault Systèmes, Vélizy-Villacoublay, France, Aug. 2020.

[102] D. Uriot and N. Pichoff, *PlotWin: Companion visualization tool for TraceWin*, Computer software, CEA Saclay, 2025. [Online]. Available: https://www.dacm-logiciels.fr/plotwin.

[103] A. W. Chao, K. H. Mess, M. Tigner, and F. Zimmermann, Eds., *Handbook of Accelerator Physics and Engineering*, 2nd. World Scientific, 2013, ISBN: 978-981-4415-84-2. DOI: 10.1142/8543.

[104] U. Ratzinger, "H-type Linac structures," in *CAS — CERN Accelerator School: Radio Frequency Engineering*, Geneva, Switzerland: CERN, 2005, pp. 351–378. DOI: 10.5170/CERN-2005-003.351.

[105] H. W. Pommerenke, "Compact radio-frequency quadrupoles for industrial and medical applications," Doctoral thesis, Universität Rostock, Rostock, Germany, 2020. DOI: 10.18453/rosdok_id00002956.

[106] J. H. Hähnel, "Development of an IH-type Linac for the acceleration of high current heavy ion beams," Doctoral thesis, Goethe Universität Frankfurt am Main, Frankfurt am Main, Germany, 2017, pp. 1–149.

[107] S. Ikeda, T. Kanesue, and M. Okamura, "Design of IH-DTL to accelerate intense lithium-ion beam for compact neutron source," Brookhaven National Laboratory (BNL), Upton, NY, USA, Tech. Rep. BNL-223791-2022-COPA, 2022.

[108] R. Tiede, H. Hähnel, and U. Ratzinger, "Beam dynamics design parameters for KONUS lattices," in *Proc. 8th International Particle Accelerator Conference (IPAC'17)*, JACoW Publishing, 2017, pp. 683–685. DOI: 10.18429/JACoW-IPAC2017-MOPIK068.

[109] M. Vretenar, "Design of the energy ramping RF system at LINAC 3," CERN, Geneva, Switzerland, Tech. Rep. CERN-AB-Note-2004-068, 2004.

[110] U. Ratzinger, B. Koubek, H. Höltermann, H. Podlech, and M. Vretenar, "Linac design within HITRIplus for particle therapy," *JACoW LINAC*, vol. 2022, pp. 134–137, 2022. DOI: 10.18429/JACoW-LINAC2022-MOPOGE01.

[111] M. M. Alauddin, "Positron emission tomography (PET) imaging with ^{18}F-based radiotracers," *American Journal of Nuclear Medicine and Molecular Imaging*, vol. 2, no. 1, pp. 55–76, 2011.

[112] J. C. Whitaker, *The RF Transmission Systems Handbook*. Boca Raton, FL, USA: CRC Press, 2002, ISBN: 978-0-8493-0973-1.

[113] C. Adolphsen, *RF system conceptual design for the LCLS-II CW SCRF Linac*, Presentation, CW SCRF Workshop, CERN, 2014. [Online]. Available: https://indico.cern.ch/event/276274/contributions/625713/.

[114] T. Bigourdan, A. Cadiou, A. Guertin, and F. Haddad, "Discussions on liquid bismuth target use as an alternative for astatine-211 production," in *EPJ Web of Conferences*, vol. 285, EDP Sciences, 2023, p. 09 002. DOI: 10.1051/epjconf/202328509002.

[115] A. Hermanne, F. Tárkányi, S. Takács, Z. Szücs, Y. N. Shubin, and A. I. Dityuk, "Experimental study of the cross-sections of α-particle induced reactions on ^{209}Bi," *Applied Radiation and Isotopes*, vol. 63, no. 1, pp. 1–9, 2005. DOI: 10.1016/j.apradiso.2005.01.015.

[116] M. Maiti, S. Lahiri, D. Kumar, and D. Choudhury, "Separation of no-carrier-added astatine radionuclides from α-particle irradiated lead bismuth eutectic target: A classical method," *Applied Radiation and Isotopes*, vol. 127, pp. 227–230, 2017. DOI: 10.1016/j.apradiso.2017.06.020.

[117] M. R. Khalvati and S. Ramberger, "Tuning and field stabilization of the CERN Linac4 drift tube Linac," CERN, Geneva, Switzerland, Tech. Rep. CERN-ACC-2014-0167, 2014.

[118] M. Vretenar and D. J. Warner, "Field stabilization in the Quasi-Alvarez structure," in *Proc. 15th Linear Accelerator Conference (LINAC'90)*, Albuquerque, NM, USA: JACoW Publishing, 1990, pp. 96–98.

LIST OF PUBLICATIONS

Articles in peer-reviewed journals

1. **L. Nikitovic**, M. Vretenar and T. Torims, "An Alvarez-type linac configuration for future carbon and helium ion therapy facilities with parallel radioisotope production", *Instruments* 2026; 10(1):16, https://doi.org/10.3390/instruments10010016

2. M. Vretenar, A. Lombardi and **L. Nikitovic**, "A helium ion linear accelerator optimised for astatine production", *Instruments* 2026; 10(2):25, https://doi.org/10.3390/instruments10020025

Publications in conference proceedings

1. **L. Nikitovic**, T. Torims and M. Vretenar, "Comparison of 352 MHz linac structures for injection into an ion therapy accelerator", Journal of Physics: Conference Series, Jan. 2024, pp. 1-8, https://doi.org/10.1088/1742-6596/2687/5/052011

2. **L. Nikitovic**, T. Torims and M. Vretenar, "Design of a helium ion linear accelerator for injection in a particle therapy synchrotron and parallel production of radioisotopes", in Proc. LINAC2024, Chicago, IL, USA, Aug. 2024, pp. 147-150, https://doi.org/10.18429/JACoW-LINAC2024-MOPB045

3. M. Vretenar, A. Lombardi and **L. Nikitovic**, "Design of a helium ion linear accelerator for astatine production", in Proc. IPAC25, Taipei, Taiwan, Jun. 2025, pp. 1044-1047, https://doi.org/10.18429/JACoW-IPAC2025-TUPB046

Presentations and seminars

1. "Comparison of Linac Structures for Injection into an Ion Therapy Accelerator and parallel production of radioisotopes", Joint NIMMS-SEEIIST Meeting #96, 14th Jul. 2023, https://indico.cern.ch/event/1306275/

2. "Linac design for HeLICS injector and for production of 211At", Internal NIMMS Meeting #51, 27th Sep. 2024, https://indico.cern.ch/event/1460836/

3. "Novel LINAC Design for Hadrontherapy and Radioisotope Production", MAPF meeting, 06.12.2023, https://indico.cern.ch/event/1217587/

Conference participation

1. 2nd CERN Baltic Conference (CBC 2022), oral presentation on ”Design of DTL for Acceleration of Ions with charge-to-mass Ratio of 1/2 with a Potential Production of Radioisotopes”, 10-12 Oct. 2022, Vilnius, Lithuania, https://indico.cern.ch/event/1147717/

2. 3rd CERN Baltic Conference (CBC 2023), poster presentation on ”Comparison of different LINAC structures for injection into an ion therapy accelerator and parallel production of radioisotopes”, 9-11 Oct. 2023, Riga, Latvia, https://indico.cern.ch/event/1288731/

3. 4th CERN Baltic Conference (CBC 2024), oral presentation on ”Novel linear accelerator design for injection of helium ions into a particle therapy synchrotron and parallel radioisotope production”, 15-17 Oct. 2024, Tallinn, Estonia, https://indico.cern.ch/event/1416853/

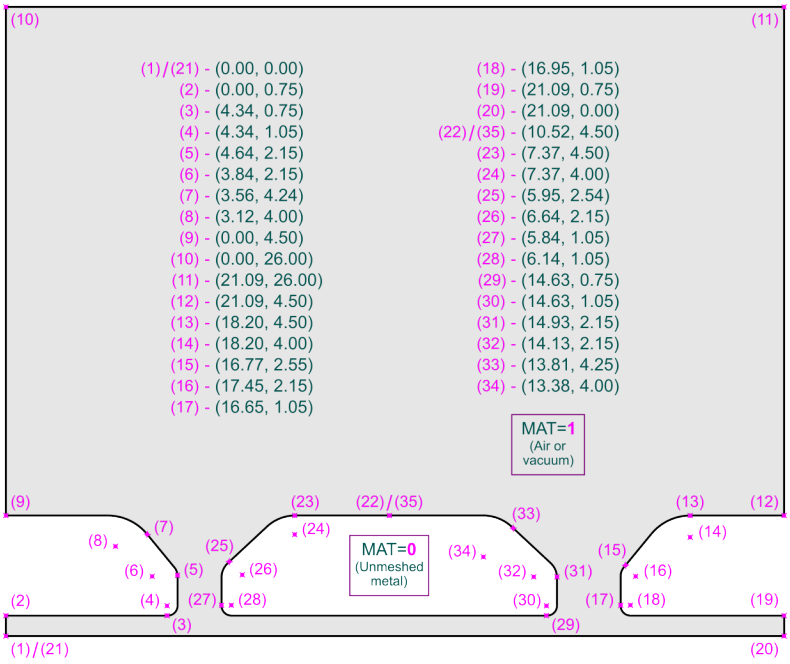
4. 14th International Particle Accelerator Conference (IPAC’23), poster presentation on ”Comparison of 352 MHz LINAC structures for injection into an ion therapy accelerator”, 7-12 May 2023, Venice, Italy, https://www.ipac23.org/

5. 3rd I.FAST Annual Meeting, discussions on novel linac designs, 16-19 Apr. 2024, Paris, France, https://indico.cern.ch/event/1357302/

Appendix A

Appendix A-1

(Two-cell cavity with defined points)



Appendix A-2

(Segment of the code from the *Automesh* control file)

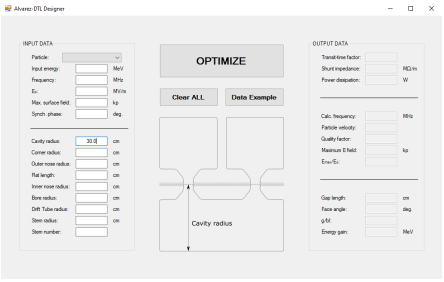
; *The boundary points for the region* 1
&$REG\ MAT = 1$&
&$PO\ X = 0.0, Y = 0.0$ & ! *Point* 01
&$PO\ X = 0.0, Y = 0.75$ & ! *Point* 02
&$PO\ X = 4.34, Y = 0.75$ & ! *Point* 03
&$PO\ NT = 2, X0 = 4.34, Y0 = 1.05, X = 0.3, Y = 0.0$ & ! *Point* 04
&$PO\ X = 4.64, Y = 2.15$ & ! *Point* 05
&$PO\ NT = 2, X0 = 3.84, Y0 = 2.15, X = 0.69, Y = 0.39$ & ! *Point* 06
&$PO\ X = 3.56, Y = 4.24$ & ! *Point* 07
&$PO\ NT = 2, X0 = 3.12, Y0 = 4, X = 0.0, Y = 0.5$ & ! *Point* 08
&$PO\ X = 0.0, Y = 4.5$ & ! *Point* 09
&$PO\ X = 0.0, Y = 26$ & ! *Point* 10
&$PO\ X = 21.09, Y = 26$ & ! *Point* 11
&$PO\ X = 21.09, Y = 4.5$ & ! *Point* 12
&$PO\ X = 18.20, Y = 4.5$ & ! *Point* 13
&$PO\ NT = 2, X0 = 18.20, Y0 = 4, X = -0.43, Y = 0.25$ & ! *Point* 14
&$PO\ X = 16.77, Y = 2.55$ & ! *Point* 15
&$PO\ NT = 2, X0 = 17.45, Y0 = 2.15, X = -0.8, Y = 0.0$ & ! *Point* 16
&$PO\ X = 16.65, Y = 1.05$ & ! *Point* 17
&$PO\ NT = 2, X0 = 16.95, Y0 = 1.05, X = 0.0, Y = -0.3$ & ! *Point* 18
&$PO\ X = 21.09, Y = 0.75$ & ! *Point* 19
&$PO\ X = 21.09, Y = 0.0$ & ! *Point* 20
&$PO\ X = 0.0, Y = 0.0$ & ! *Point* 21

; *The points for the drift tube in the center*
&$REG\ MAT = 0$&
&$PO\ X = 10.52, Y = 4.5$ & ! *Point* 22
&$PO\ X = 7.37, Y = 4.5$ & ! *Point* 23
&$PO\ NT = 2, X0 = 7.37, Y0 = 4, X = -0.43, Y = 0.24$ & ! *Point* 24
&$PO\ X = 5.95, Y = 2.54$ & ! *Point* 25
&$PO\ NT = 2, X0 = 6.64, Y0 = 2.15, X = -0.8, Y = 0.0$ & ! *Point* 26
&$PO\ X = 5.84, Y = 1.05$ & ! *Point* 27
&$PO\ NT = 2, X0 = 6.14, Y0 = 1.05, X = 0.0, Y = -0.3$ & ! *Point* 28
&$PO\ X = 14.63, Y = 0.75$ & ! *Point* 29
&$PO\ NT = 2, X0 = 14.63, Y0 = 1.05, X = 0.3, Y = 0.0$ & ! *Point* 30
&$PO\ X = 14.93, Y = 2.15$ & ! *Point* 31
&$PO\ NT = 2, X0 = 14.13, Y0 = 2.15, X = 0.68, Y = 0.41$ & ! *Point* 32
&$PO\ X = 13.81, Y = 4.25$ & ! *Point* 33
&$PO\ NT = 2, X0 = 13.38, Y0 = 4, X = 0.0, Y = 0.5$ & ! *Point* 34
&$PO\ X = 10.52, Y = 4.5$ & ! *Point* 35

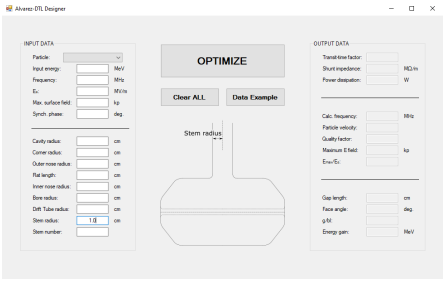
Appendix B

Appendix B-1

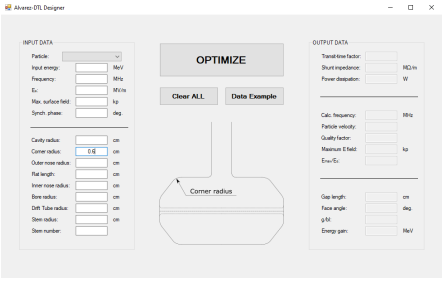
(Descriptive images within A-GUI corresponding to the input data: (a) cavity radius, (b) stem radius, (c) corner radius, and (d) DT radius)



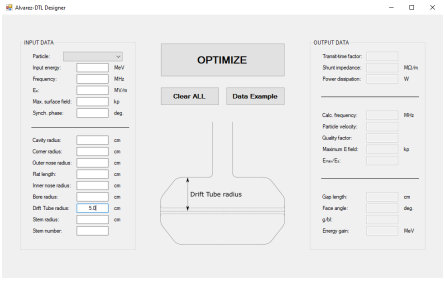
(a)



(b)



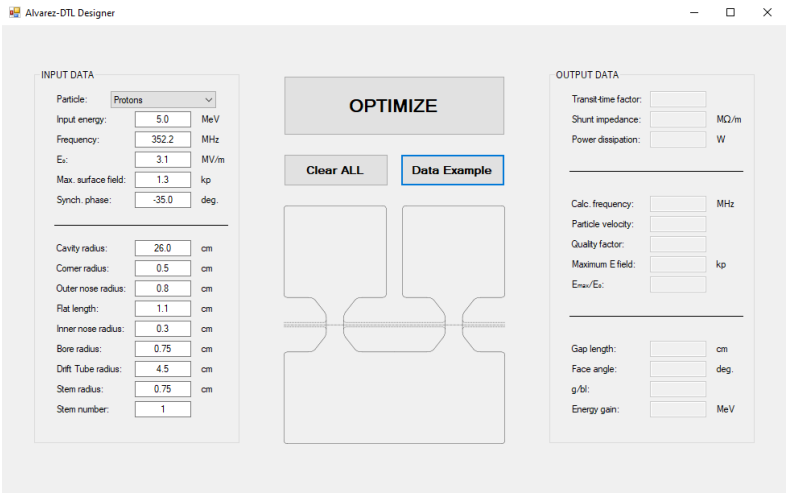
(c)



(d)

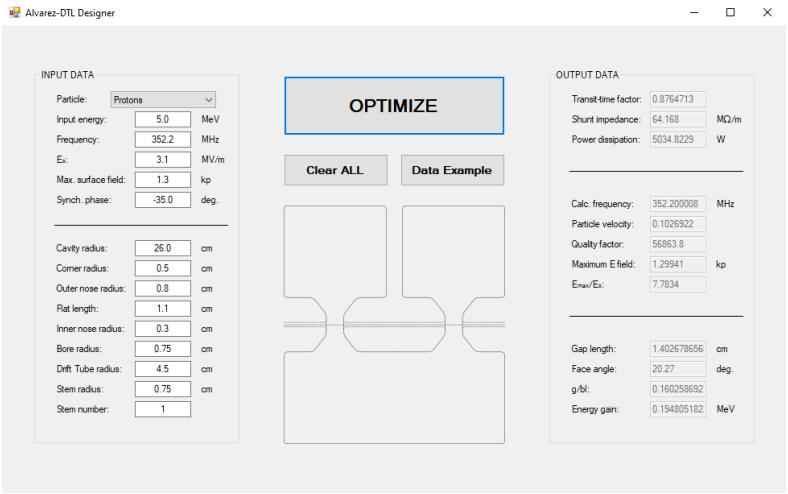
Appendix B-2

(Input data provided by *Data Example* button in A-GUI)



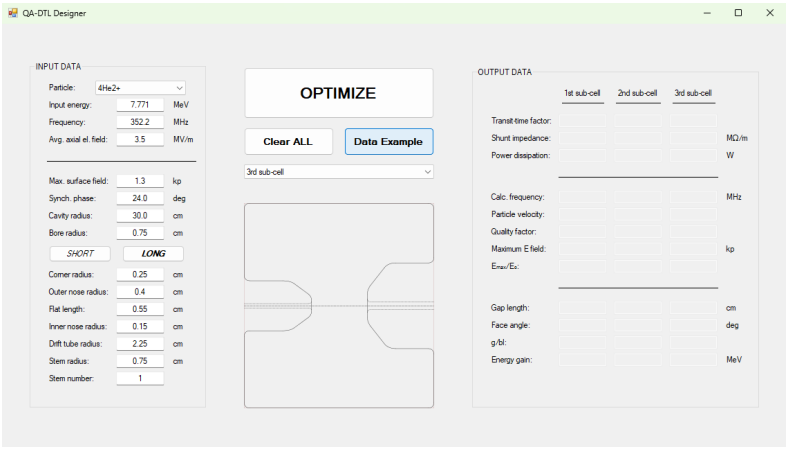
Appendix B-3

(Interface of A-GUI after completing the optimization of DTL cell)



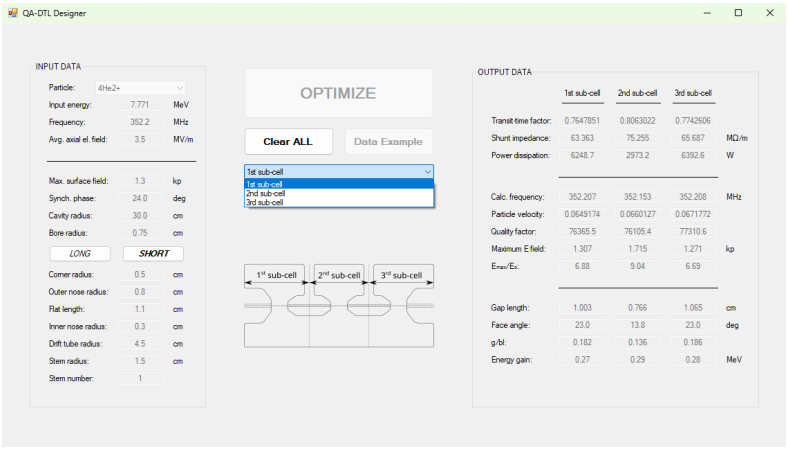
Appendix B-4

(Input data provided by *Data Example* button in QA-GUI)



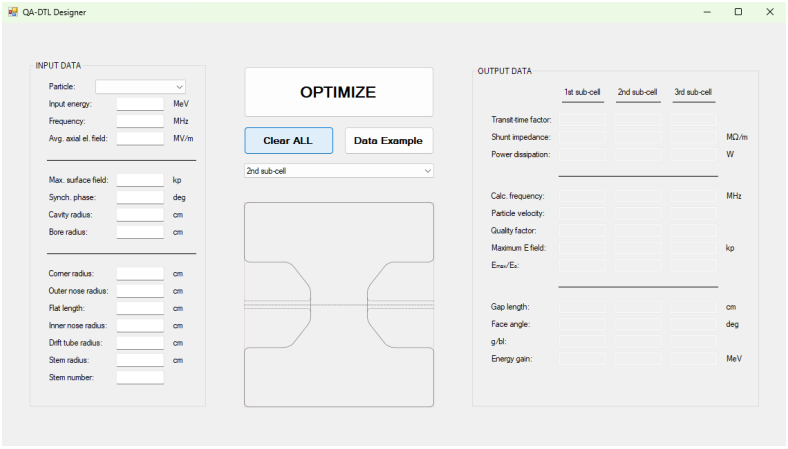
Appendix B-5

(Interface of QA-GUI after completion of the optimization process of QA-DTL super-period)



Appendix B-6

(Interface of QA-GUI after activation of *Clear ALL* button)





Lazar Nikitović was born in 1994 in Cetinje, Montenegro. He obtained his Bachelor's degree (2016), Specialist degree (2017), and Master's degree (2020) in Electrical Engineering from the University of Montenegro. From the beginning of 2022 until the end of 2024, he was enrolled in the Doctoral Student Programme at CERN, where he worked on the development of linear accelerators for medical applications. From 2025 to 2026, he was a researcher at the Institute of Particle Physics and Accelerator Technologies, Faculty of Natural Sciences and Technology, Riga Technical University (RTU). His research interests are radio frequency (RF) engineering and accelerator technologies.